Elasticity of Proteins and Polymers from Molecular Dynamics Simulations

Dissertation

zur Erlangung des akademischen Grades eines Doktors der Naturwissenschaften (Dr. rer. nat.)

am Fachbereich Physik der Freien Universität Berlin

vorgelegt von
Richard Schwarzl

Berlin, 2020

Erster Gutachter:	Prof. Dr. Roland R. Netz Freie Universität Berlin
Zweiter Gutachter:	Prof. Dr. Joachim Dzubiella Albert-Ludwigs-Universität Freiburg
Tag der Disputation:	16. Juli 2021

Contents

Chapter 1

Introduction

Macromolecules, which are large molecules with a usual diameter between 1 nm and 1 µm, are ubiquitous in nature. When we think in terms of large biomolecules, they consist of smaller molecules like carbohydrates, lipids, proteins, or nucleic acids. The physiological functions of these biomolecules are many-faceted and include the energy delivery to cells based on the breakdown of sugars,[1] the formation of cell-membrane bilayers,[2] the interplay between enzyme function and protein dynamics as regulatory processes in organisms,[3,4] as well as genome expression in DNA.[5] In 1946, James Batcheller Sumner, John Howard Northrop and Wendell Meredith Stanley received the Nobel Prize in chemistry for "the discovery that enzymes can be crystallized" and for "their preparation of enzymes and virus proteins in a pure form",[6] and in 1958 the Nobel Prize in chemistry was awarded to the British chemist Frederick Sanger for his studies on the structure of insulin.[7] Consequently, efforts to investigate the structure and interaction of biomolecules in connection to their physiological functions persist now for more than seventy years.[8–10]

The complexity of biomolecules can be estimated, when we realize that today, the exact pathways for interactions and their connection to structural changes of proteins on a molecular level is still an enormously active field of research and that many aspects of it are not well understood.[11–14]

Several new or significantly improved experimental methods drive the research of molecular processes together with theoretical modeling and computational simulations. For the study of proteins, these methods include nuclear magnetic resonance (NMR),[15–18] small-angle X-ray scattering (SAXS),[19–21] single molecule force spectroscopy (SMFS),[22–26] vibrational spectroscopy,[27–30] Förster resonance energy transfer (FRET) microscopy,[31–33] the development of theoretical models to interpret energy landscapes and to estimate transition and escape times,[34–39] as well as extensive computational efforts to model systems by means of Brownian dynamics (BD) simulations, all atom molecular dynamics (MD) simulations and ab initio or quantum mechanics calculations.[40–51]

Another class of macromolecules relevant to this thesis are synthetic polymers which

have long been a major field of material science.[52–60] They also play a huge role in medical applications such as tissue engineering[61–63] or the design of nanocarriers for drug delivery.[64–66]

Throughout this thesis, experimental results from physics, chemistry, biology, and pharmaceutical science are combined with mostly all atom molecular dynamics simulations as well as theoretical descriptions to elucidate quantitative relationships or to reveal scaling predictions.[67–71]

In chapter 2, we present MD simulations in explicit water to investigate the force-extension relations of the five homopeptides polyglycine, polyalanine, polyasparagine, poly(glutamic acid), and polylysine. Simulations in the low-force regime allow for the determination of the Kuhn length, whereas analysis of the high-force regime provides the equilibrium polymer contour length as well as the linear and non-linear stretching moduli, which agree well with quantum- chemical density-functional theory calculations. We find these parameters to vary considerably between the different homopeptides. Based on the analysis of the dihedral angle distribution, we confirm the applicability of the inhomogeneous partially freely rotating chain (iPFRC) model that accounts for side-chain interactions and restricted dihedral rotation. We augment the model to implement the force-dependent change of the polymer contour length due to the stretching-force induced increase of bond angles and bond lengths. We find the simulated stretching response to be described well by an augmented iPFRC model. Consequently, we provide analytic expressions which act as reliable model predictions for the force-extension relations of the simulated homopeptides. We present a quantitative comparison between published experimental single-molecule force-extension curves for different polypeptides with simulation and model predictions. The thermodynamic stretching properties of polypeptides are investigated by decomposition of the stretching free energy into energetic and entropic contributions.

Chapter 3 is motivated by the investigation of structural signal transmission mechanisms based on the two-component signaling motif of light-regulated histidine kinases by Möglich, et al.[72] To this end, we simulate the coiled coil linker structure Jα which is based on the light-oxygen-voltage (LOV) histidine kinase YF1.[72,73] This coiled coil linker structure consists of two parallel alpha-helical polypeptides. The system is stable in MD simulations in explicit water but can undergo different relative motions which include shift, splay, and twist. We analyse the relative fluctuations of the end-termini for the two helices concerning the relative motions shift, splay, and twist. By employment of linear response theory, we can calculate the response functions from these fluctuations which are consequently translated in Fourier space. This approach can be compared to the description of an alternating current circuit. The knowledge of the linear response functions allows for the definition of a "real" periodic driving force on one end of one helix and a "virtual" periodic force on another end, such that the relative fluctuations become zero (c.f. eqs 3.5 to 3.7). This definition yields the relative motion

specific frequency-dependent transmission functions as quotients of two response functions in Fourier space. These functions provide a measure for the efficiency of a relative motion to transmit a signal from one end of the double-helical structure to another end. The extracted response functions are fitted to extract correlation times and strengths inherent to the relative motions. The total simulation time of more than 10 μs and the fits of the response functions allow for the description of the transmission function for frequencies between 100 kHz and 1 THz. The analysis provides a blueprint on how to quantify the efficiency of signal transmission through different structural motions inside a signaling protein complex.

In chapter 4, we investigate the effect of change in temperature on the force-extension relation and the thermodynamic stretching properties for polyethylene glycol (PEG) and poly(N-isopropylacrylamide) (PNiPAM) from MD simulations in explicit water. In collaboration with the research group of Thorsten Hugel from Albert-Ludwigs-Universität in Freiburg, these results are compared with experimental single molecule force spectroscopy measurements. The comparison of the two water-soluble polymers reveals an opposing temperature dependence of the stretching response for PEG and PNiPAM. Based on MD simulations in explicit water of both PEG and PNiPAM at a wide range of temperatures, we attribute these effects to interactions of the polymers with water molecules (hydration) which impacts the mechanics of these polymers through stabilization. Upon investigation of the stretching thermodynamic properties by decomposition of the stretching free energy into energetic and entropic contributions, we find that these contributions compete. For PEG, we can link the temperature-dependent change in energetic and entropic contributions to the non-linear behavior of the mean fraction of monomers in trans state upon an increase of the stretching force. Below 200 pN the probability for water bridges to stabilize gauche states in PEG turns out to be increased for lower temperatures. For both PEG and PNiPAM, hydration effects are of such relevance that traditional polymer models such as the freely jointed chain or worm-like chain are rendered nonphysical in their attempt to describe the force-extension relation.

Finally, in Chapter 5 we present Brownian dynamics simulations of grafted and non-grafted bead-spring chains under linear shear flow conditions including hydrodynamic interactions. This bead-spring chain acts as a coarse-grained model for the von Willebrand factor,[74,75] a large glycoprotein whose activation is crucially involved in primary hemostasis.[76–78] The shear-flow-increase-driven transition from a globular to an elongated state has been suggested as a mechanism to activate von Willebrand factor. The elongation leads to the exposure of cleavage sites for interaction with ADAMTS13, enables the von Willebrand factor to bind to the vessel wall and ultimately yields the aggregation of blood platelets at the site of an injured vessel.[68,79–83] This study provides a comparison between the previously well-studied situation of von Willebrand factor under linear shear flow conditions in the non-grafted scenario[74,75] to the not yet studied grafted situation where von Willebrand is bound to the vessel wall. Tensile

force profiles and the shear-rate-dependent globular-coil transition for grafted and non-grafted chains are investigated to shed light on the different unfolding mechanisms. The critical shear rate, at which the globular-coil transition takes place, is investigated. The scaling of the critical shear rate with the monomer number is inverse for the grafted and non-grafted scenarios. This implicates that for the grafted scenario, larger chains have a decreased critical shear rate, while for the non-grafted scenario higher shear rates are needed to unfold larger chains. Protrusions govern the unfolding transition of non-grafted polymers, while for grafted polymers, the maximal tension appears at the grafted end. For the grafted polymer, we discuss the interplay between drag and lift forces that lead to a specific angle at which the polymer reaches into the solvent.

The common intention of the aforementioned projects is to provide a more robust understanding of the underlying mechanics and thermodynamic properties for the force-dependent and temperature-dependent response of proteins and polymers in water.

Chapter 2

Force Response of Polypeptide Chains from Water-Explicit MD Simulations

Bibliographic information: This chapter and appendix A have previously been published. Reprinted with permission from Ref. [i], https://doi.org/10.1021/acs.macromol.0c00138.

Author contribution statement: Richard Schwarzl carried out all simulations and the analysis of the data except for the DFT calculations, which have been carried out by Florian N. Brünig. Roland R. Netz supervised the project. Richard Schwarzl created all figures und wrote the first version of the manuscript except the methods part for the DFT calculations, which has been written by Florian N. Brünig. Fabio Laudisio contributed to the figure A.1 in appendix A by investigation of the effect of the salt concentration during his bachelor thesis under the supervision of Richard Schwarzl. For the investigation of the effect of the salt concentration, Richard Schwarzl provided the input files for the simulations and additionally carried out the same simulations himself. All authors except Fabio Laudisio discussed the results and contributed to the final version of the manuscript, which is published under: R. Schwarzl, S. Liese, F. N. Brünig, F. Laudisio, and R. R. Netz, Force Response of Polypeptide Chains from Water-Explicit MD Simulations, Macromolecules 53, 4618 (2020).

2.1 Introduction

Proteins consist of amino acids that are linked by peptide bonds. Numerous biological processes depend on the mechanical response of proteins [84–89] and the understanding of such processes requires as a first step the accurate description of the stretching response of single peptide chains. The elastic response of single protein molecules has been thoroughly investigated experimentally by atomic force microscopy (AFM). [90–96] The experimentally measured force-stretching relations of unfolded peptide chains are

typically compared with the freely jointed chain (FJC) [97–99] model or the worm-like chain (WLC) [100,101] model. The WLC model has been shown to describe relatively stiff biological polymers such as double-stranded DNA [102] very well, and the persistence length that results from a fit to the force-extension relationship is related to the DNA bending stiffness and thus has physical meaning. For flexible polymers, which at the atomic scale consist of chemical bonds with a preferred bond length and preferred bond angle, neither the FJC nor the WLC model is microscopically correct. In fact, for the stretching of titin immunoglobulin domains, a multitude of different theoretical polymer models have been used that account for various molecular aspects such as fixed or extensible bond lengths, fixed bond angles, dihedral potential effects as well as specific interactions between polymer backbone and solvent. [92,103–105]

While experimental force-extension data of polypeptides is routinely fitted with the freely-jointed chain (FJC) model, which is equivalent to the Langevin model for the alignment of a dipole in an external field, the bond length that results from such a fit has no physical meaning and in particular does not agree with the actual chemical peptide bond length. As a step towards a more accurate description of experimental force-extension data of polypeptides, the stretching response of a freely rotating chain (FRC) model, which includes a fixed bond angle, was favorably compared with experimental data. [106,107] The disadvantage of the FRC model is that the force-extension relation is not available in closed form but must be calculated numerically by transfer matrix techniques. The resulting stretching behavior is quite complex and exhibits three distinct scaling regimes, a low-force linear regime, an intermediate regime that is similar to the response of a WLC chain, and finally a high force regime that can be mapped onto the FJC model. [106] But a peptide chain is also not accurately described by the FRC model, since the peptide backbone bond lengths and angles are not all the same and, more importantly, strong dihedral potentials exist that are very different for different bonds along the peptide backbone. In fact, one of the bonds, the so-called peptide bond, is almost unable to rotate. Motivated by this, the more general inhomogeneous partially freely rotating chain (iPFRC) model [108] was introduced, which, in addition to the inhomogeneous bond lengths and bond angles along the peptide backbone, accounts for the stiff peptide bond and fixes its dihedral angle to 180°. All these models are ideal and neglect interactions between amino acids as well as hydration effects, which for PEG have been demonstrated to dramatically influence the stretching behavior. [48] Particularly important for peptides are the interactions between side chains of neighboring amino acids, which are difficult to treat in theoretical polymer models.

In this paper, we investigate the force-extension relation of five different homopeptides consisting of 13 amino acids by means of molecular dynamics (MD) simulations in explicit water. In analogy to AFM experiments, we apply a constant force to the outermost C_α atoms and determine the average end-to-end distance between those C_α atoms, as schematically shown in Figure 2.1a and as done earlier for PEG and PNIPAM. [48,71] We choose polyglycine (GLY), which consists of only the peptide backbone and hence represents the structurally simplest peptide, and in addition polyalanine

(ALA), polyasparagine (ASN), polyglutamic acid (GLU) and polylysine (LYS). These peptides span a wide range from hydrophobic to hydrophilic and charged polymers.

In order to separate effects due to interactions between neighboring amino acids from effects due to interactions between non-neighboring amino acids, we compare stretching simulations of tripeptides with stretching simulations of peptides consisting of 13 amino acids, both in water. From this comparison we conclude that interactions between side chains of neighboring amino acids are strong and modify significantly the unstretched peptide contour length and the backbone extensibility. By comparison of tripeptide simulations in water at room temperature and in vacuum at zero temperature, we demonstrate that hydration effects do not modify the peptide contour length and the peptide contour extensibility, which we explain by a detailed hydrogen bonding analysis. The comparison with density-functional quantum-chemistry calculations of stretched tripeptides shows that the MD peptide force fields are well parameterized in terms of the backbone contour length and its extensibility. We then extract the peptide Kuhn length from the low-force stretching response of 13-mers. An analysis of dihedral angle distributions in terms of Ramachandran plots demonstrates that indeed the peptide bond is not rotating, which confirms the basic assumption of the iPFRC model. By comparison of the iPFRC model with the MD simulations at large stretching force, we determine the single undetermined parameter in the iPFRC model and show that it provides an excellent description of MD stretching curves over the entire force range if the contour length and contour extensibility are correctly taken into account. Finally, we compare the force-extension relations from MD simulations and the iPFRC model with experimental AFM results obtained previously [107] for two different heteropolymers, titin and spider silk (GVGVP), and for polylysine. The agreement is overall good but shows some discrepancy in the 200 pN force range, which might be due to peptide bond isomerization effects. We also determine the energetic and entropic contributions to the stretching response and find that water bridges, where one water forms two hydrogens bonds with the polypeptide, play only a marginal role in thermodynamically stabilizing homopeptide conformations against stretching. We conclude that the iPFRC model is an accurate model for the description of peptide stretching, provided that effects due to restricted backbone dihedral rotation and side-chain interactions are accounted for by suitably choosing the single fit parameter of the iPFRC model.

2.2 Results

In Figure 2.1a we show an MD simulation snapshot of an alanine chain with 13 residues, which we abbreviate by ALA_{13}, solvated in water at a stretching force of $f = 1300\,\mathrm{pN}$. Constant stretching forces f, parallel to the z-axis, act in opposite directions on the first and last C_α atoms. For each force, we calculate the time-averaged end-to-end distance z_{ete} in z-direction between these two C_α atoms. In Figure 2.1b we present force-extension results for all five polypeptides investigated in this study. All simulations are performed without added salt, in the supplementary information, salt effects

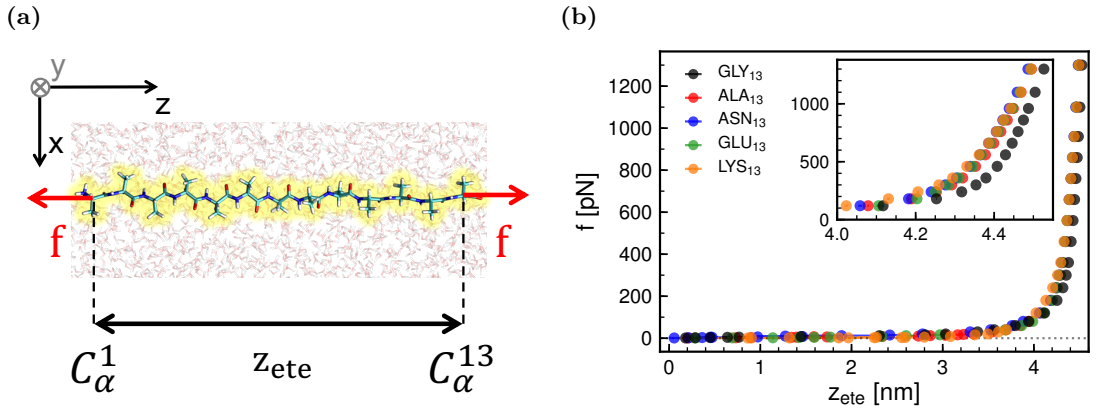

Figure 2.1: (a) Snapshot of an MD simulation of ALA_{13} at a stretching force of $f = 1300\,\mathrm{pN}$. (b) Simulation results for the force-extension relation of five different polypeptides. The inset highlights the high-stretching regime.

are shown to be negligible in the force range considered by us. Deviations between different peptides are revealed in the inset, where we show the large stretching regime. Of the five polypeptides, polyglycine shows the largest end-to-end distance z_{ete} for a given force, as we will explain based on an analysis of the contour lengths of the different peptides later on.

To quantify the stretching response of different peptides, we first need to determine the contour length in the absence of an external force, which need not be the same for the different peptides. For this we probe the stretching response of a tripeptide, which is the smallest subunit of a polypeptide for which the separation vector between the outer C_α atoms in the stretched state is parallel to the end-to-end vector of the polypeptide. [107] This is so because one amino acid residue consists of an odd number of backbone atoms, namely three. Figures 2.2a and 2.2b show as solid lines the potential energy landscapes of all tripeptides in vacuum at zero temperature as a function of the separation between the outer C_α atoms, denoted by $2a$, which are obtained from ground state optimization of the MD force field (see Figure 2.2c for a snapshot and illustration of the geometry), where a denotes the contour length per amino acid residue.

The results demonstrate the existence of different competing ground states that exhibit sharp transitions as different ground state energies cross. The dotted lines in Figures 2.2a and 2.2b correspond to the free energy landscapes obtained from MD umbrella simulations of tripeptides in water at room temperature T=300 K. For large stretching the differences between the corresponding solid and broken lines are very small, which means that hydration as well as conformational fluctuation effects are not important in the stretched state. For small values of $2a$, i.e. in the unstretched and compressed state, the differences between the vacuum $T = 0\,\mathrm{K}$ results and the hydrated finite-T results are significant and the sharp transitions between different groundstates

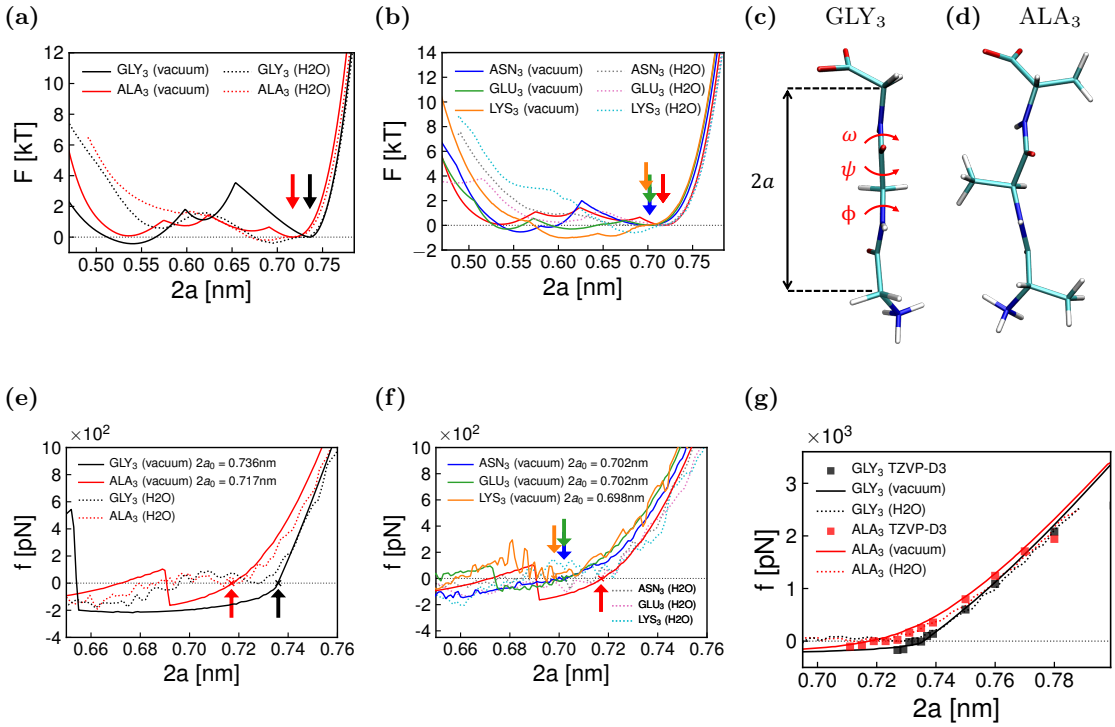

Figure 2.2: (a+b) Comparison of energy landscapes in vacuum at $T = 0\,\mathrm{K}$ (solid lines) and free energy landscapes in water at $T = 300\,\mathrm{K}$ (dotted lines) from MD simulations as function of the separation between the terminal C_α atoms, $2a$, for (a) GLY_3, ALA_3 and (b) ASN_3, GLU_3, LYS_3 (ALA_3 in red is shown for reference). Ground state conformations for a strongly stretched state ($2a = 0.77\,\mathrm{nm}$) of (c) GLY_3 and (d) ALA_3 obtained from the MD force field in vacuum at $T = 0\,\mathrm{K}$. The structures reveal that the backbone of ALA_3 is non planar, which is due to repulsive side-chain backbone interactions. GLY_3 on the other hand adopts a planar state at the same separation. (e+f) Stretching forces of the different tripeptides, obtained by numerical derivative of the energy and free energy landscapes in (a) and (b). The largest separation $2a_0$ where the stretching force in vacuum vanishes is used to define the equilibrium monomer lengths a_0, which are denoted by vertical colored arrows. Note that the range of separations shown is decreased compared to (a) and (b) in order to focus on the equilibrium configuration with separation $2a_0$. (g): Comparison of stretching forces from quantum chemistry DFT in vacuum at $T = 0\,\mathrm{K}$ (data points), MD force-fields in vacuum at $T = 0\,\mathrm{K}$ (solid lines), MD force-fields in water at $T = 300\,\mathrm{K}$ (dotted lines) for the stretching force of alanine and glycine tripeptides.

that are visible in the $T = 0\,\mathrm{K}$ results are expectedly washed out at room temperature. In Figures 2.2e and 2.2f we show the stretching forces of tripeptides, which are obtained from the numerical derivative of the tripeptide energy and free energy landscapes. We define the equilibrium monomer contour length a_0 by the largest monomer length at which the force vanishes and base our results, which are denoted by vertical colored arrows, on the forces obtained within the vacuum calculations (solid lines). The re-

sulting equilibrium monomer lengths are 0.74 nm for glycine, 0.72 nm for alanine and 0.70 nm for asparagine, glutamic acid and lysine. The fact that the glycine equilibrium monomer length is significantly larger than for the other investigated peptides is explained by the fact polyglycine forms a perfectly planar structure in the ground state, while the other polypeptides exhibit non-planar ground states due to repulsive interactions between side chains and the backbone. This is illustrated in Figure 2.2c and d, where we show MD snapshots in vacuum and at $T = 0\,\mathrm{K}$ of GLY_3 and ALA_3 at the same fixed separation $2a = 0.77\,\mathrm{nm}$. This fixed separation corresponds to a significant stretching force in the range of 2 nN. We see that the backbone of alanine is non planar even at such a strong stretching force.

In Figure 2.2g we compare DFT results in vacuum at $T = 0\,\mathrm{K}$ with MD force-field results in vacuum at $T = 0\,\mathrm{K}$ and in water at $T = 300\,\mathrm{K}$ for the stretching force for glycine and alanine tripeptides. DFT and MD results agree very well in the relevant force regime between 0 pN and 1500 pN, which reflects that amber backbone force-field parameters have been optimized using gas-phase QM calculations.[109] The DFT results confirm the increased resistance to stretching of alanine compared to glycine. An analysis of the MD interaction energies in vacuum for ALA_3 and GLY_3 (cf. supporting information) shows that the smaller contour length of alanine is caused by repulsive Lennard-Jones interactions between the side-chain and the backbone. This means that backbone rotational degrees of freedom are restricted by the presence of side-chains in alanine, the same mechanism acts for the other polypeptides as well.

In order to further understand the structural differences between polyglycine and the other polypeptides, we investigate backbone dihedral angles of polypeptides in water. The nomenclature for the different backbone dihedral angles is defined in Figure 2.2c, ϕ denotes the $C-C_\alpha-N-C$ dihedral angle and ψ denotes the $N-C-C_\alpha-N$ dihedral angle. We calculate the dihedral angles ϕ and ψ for zero stretching force and for a large stretching force of 1300 pN by averaging over all 12 equivalent dihedral angles in the polypeptide. The resulting Ramachandran plots for zero force for GLY_{13} and for ALA_{13} are shown in Figure 2.3a and Figure 2.3b. We see that for glycine the distribution of the dihedral ϕ is symmetric and rather broadly distributed, whereas for alanine the distribution is asymmetric and restricted to a smaller region of the conformational space, which demonstrates the restricted backbone rotation due to side-chain steric hindrance. The symmetry breaking persists to large stretching forces of 1300 pN in Figure 2.3c and Figure 2.3d. These results show that even at large stretching forces alanine is not planar, while glycine is perfectly planar at such high forces. That this effect is not specific to alanine but holds also for all other investigated polypeptides, except glycine, can be seen in the plots Figures 2.3e to 2.3g. The intercept of the broken lines in Figure 2.3 indicates the planar state, where $\phi = 180°$ and $\psi = 180°$.

We next analyze the stretching response of all tripeptides quantitatively. In Figure 2.4 we again show our results for the stretching force of tripeptides in vacuum and at $T = 0\,\mathrm{K}$ obtained from DFT and MD force fields as a function of the end-to-end distance $2a$. We fit the stretching force from the MD zero-temperature calculations by

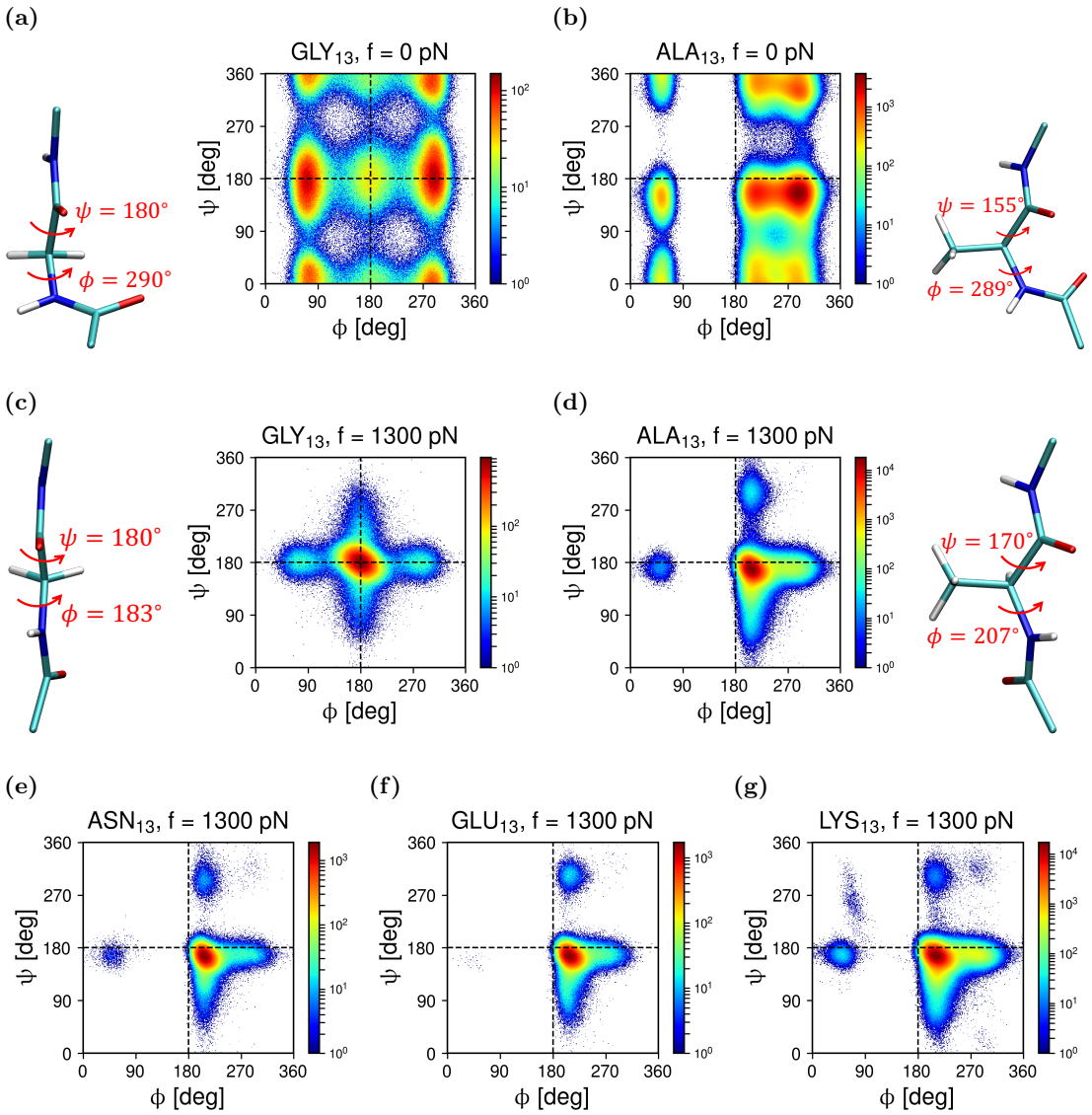

Figure 2.3: (a - d): Ramachandran plots for GLY_{13} and ALA_{13} at 0 pN and 1300 pN from MD simulations in water. All ϕ and ψ angles of the polypeptides are averaged. Side-chain interactions in polyalanine shift the most probable (red) region away from the symmetric planar state $\phi = 180°$, $\psi = 180°$ (intercept of the broken lines). The results for polyglycine on the other hand indicate a planar conformation. The results are in close agreement with previously published Ramachandran plots of GLY_3 and ALA_3.[109–112] MD simulations snapshots in water show the most probable conformations of a part of the polypeptides. (e - g): Ramachandran plots of ASN_{13}, GLU_{13} and LYS_{13} at a stretching force of 1300 pN show that all peptides except glycine adopt non planar most probable states.

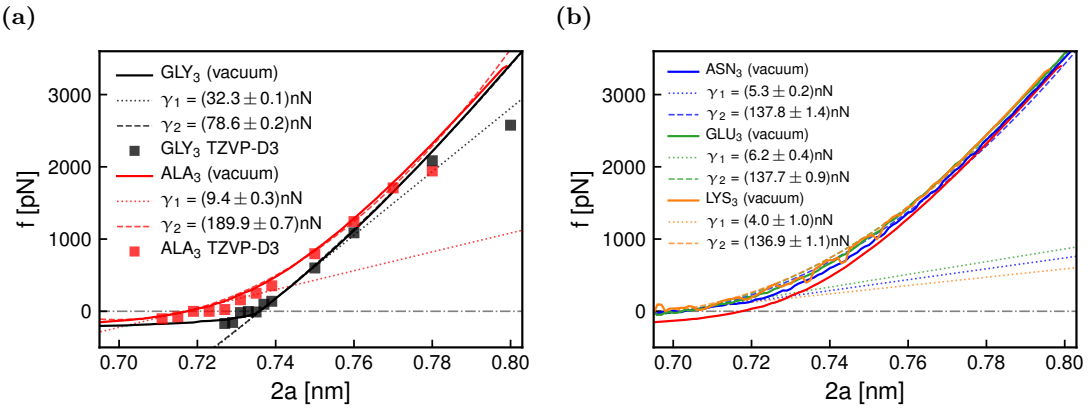

Figure 2.4: (a) Stretching force for GLY_3 and ALA_3 tripeptides in vacuum and at $T = 0\,\mathrm{K}$ as a function of the extension $2a$. Solid lines denote results from MD force fields and squares denote results from DFT. The first order (dotted lines) and second-order (broken lines) elastic responses defined in eq 2.5, which are fitted to the MD results, illustrate the relative importance of the stretching moduli γ_1 and γ_2. (b) Results for ASN_3, GLU_3 and LYS_3. Results for ALA_3 in red are included for reference.

a second-order polynomial function, similar to a previous analysis,[107] given by

$$f = \gamma_1 \left(\frac{a}{a_0} - 1 \right) + \gamma_2 \left(\frac{a}{a_0} - 1 \right)^2 , \tag{2.1}$$

where we use the equilibrium monomer lengths a_0 as determined in Figures 2.2e and 2.2f. The linear stretching modulus coefficient γ_1 is determined by a local fit for monomer lengths a above the equilibrium monomer length a_0 in the range $0 \leq (a/a_0 - 1) < 0.015$. For the non-linear coefficient γ_2 the full range of data is used for fitting. The fits to the MD results are presented in Figure 2.4 as dotted lines (including only the first order) and as dashed lines (including first and second-order). It is seen that non-linear stretching effects are rather small for glycine while non-linear effects are important for alanine. This can be explained by the fact that alanine is rather soft for small stretching due to its non-planar ground state and hardens for larger stretching, similar to results observed previously for the stretching of RNA molecules.[107] We conclude that the non-linear model eq 2.1 fits the $T = 0\,\mathrm{K}$ stretching response of tripeptides very well over the entire force range.

The parameters extracted so far describe the zero-temperature stretching response of polypeptides and thus neglect the effects of conformational fluctuations. Finite-temperature fluctuation effects in fact become important for stretching forces smaller than roughly 1 nN.[107] For low forces the stretching response of polymers is characterized by a linear relation between the end-to-end extension z_{ete} (normalized by the equilibrium unstretched contour length L_0) and the applied stretching force f according

to

$$\frac{z_{ete}}{L_0} = \frac{f a_{Kuhn}}{3 k_B T}, \tag{2.2}$$

which defines the Kuhn length a_{Kuhn}.[53,113,114] This relation holds if the low-stretching condition $f a_{Kuhn} < k_B T$ is satisfied and if monomer-monomer interactions are neglected.[115,116] Since the polypeptides used in our simulations are rather short, the transition from the linear stretching response $z_{ete} \sim f$ to the non-linear Pincus stretching response $z_{ete} \sim f^{2/3}$, which is expected to occur in the presence of repulsive monomer-monomer interactions at very low stretching forces, cannot be observed.[117–119] In the supporting information we demonstrate that the addition of salt into our simulations does not change the stretching response, we conclude that electrostatic repulsive interactions between charged side chains are not relevant in the force regime we are investigating. Figure 2.5a shows the MD force-extension data in the small force regime. We extract a_{Kuhn} from the MD simulation results by linear fits in the force range $0 \leq f < f_{max}$, indicated by solid straight lines. The upper bound f_{max} is determined by the aforementioned condition $f_{max} a_{Kuhn} = k_B T$ and is indicated by dotted horizontal lines in Figure 2.5a. The contour length L_0 at zero force in eq 2.2 is given by $12 \times a_0$, where the equilibrium monomer lengths a_0 are taken from Figures 2.2e and 2.2f. The resulting Kuhn lengths are shown in Figure 2.5c for all different peptides. Except for asparagine, a larger side-chain size leads to a larger Kuhn length. The inset of Figure 2.5c shows the squared radius of gyration R_G at zero force as a function of the Kuhn length. The relation between the squared radius of gyration R_G^2 and the Kuhn length a_{Kuhn} is described by the heuristic relation

$$R_G^2/N = \alpha a_{Kuhn} a_0 + \beta, \tag{2.3}$$

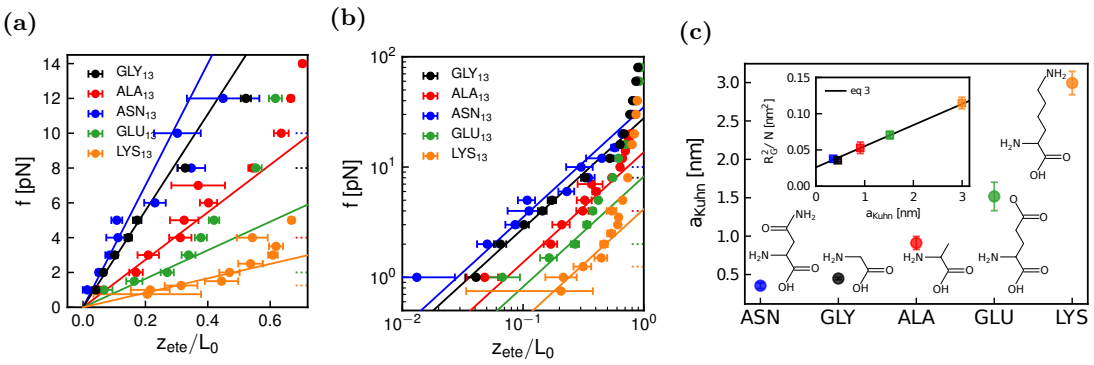

Figure 2.5: (a): Low-force MD simulation results. Solid lines depict linear fits according to eq 2.2 and yield estimates for the Kuhn length a_{Kuhn} for the different polypeptides. (b): Same results as in (a) on a double-logarithmic scale. (c): Results for the Kuhn length are shown in ascending order, corresponding chemical peptide structures are included next to each data point. The inset shows the correlation between the squared radius of gyration divided by $N = 12$ at zero stretching force and the Kuhn length according to eq 2.3.

where $\alpha = 0.04$ and $\beta = 0.025\,\mathrm{nm}^2$ are the best-fit values. The presence of a finite offset β is unexpected but obviously needed to describe the data.
We have so far determined the most important polymer parameters of the different polypeptides investigated in this study, namely the equilibrium unstretched monomer length a_0, from which the contour length $L_0 = Na_0$ in the absence of a stretching force can be calculated, the Kuhn length a_{Kuhn}, and the non-linear elastic coefficients that characterize the stretching response of the contour length. Notably, all these parameters are rather different for different polypeptides. The Kuhn length describes the low-force stretching response, while the elastic parameters describe the high-force stretching response of polymers. We now set out to describe the polypeptide stretching response at intermediate forces. Based on the stretching response of a partially restricted freely-rotating chain model,[106] a simple heuristic formula for the force-extension relation of polypeptides, which omits the intermediate worm-like-chain stretching regime, was given as [108]

$$f_{\mathrm{iPFRC}} = \frac{k_{\mathrm{B}}T\,\mathrm{z_{ete}}}{\mathrm{L}(f)}\left(\frac{3}{a_{\mathrm{Kuhn}}} + \frac{1}{c\;a_0}\frac{\mathrm{z_{ete}}/\mathrm{L}(f)}{1-\mathrm{z_{ete}}/\mathrm{L}(f)}\right). \tag{2.4}$$

Note that this expression is constructed such as to reproduce both the low-force and the high-force limits of the stretching response of a rotating chain model. We here generalize the iPFRC model by allowing the contour length $L(f)$ to be force-dependent, which is motivated by the results shown in Figures 2.4a and 2.4b. As a main feature, the inhomogeneous partially freely rotating chain (iPFRC) model accounts for the fact that the dihedral angle ω, which describes the peptide bond, defined by $\mathrm{C_\alpha}$–N–C–$\mathrm{C_\alpha}$, is fixed at 180°, see Figure 2.2c for a graphical definition. In the original iPFRC model, the other two dihedral angles, ϕ and ψ (as defined in Figure 2.2c), are free to rotate, which clearly is an approximation. To test whether the dihedral angle ω is restricted in our simulations, we consider Ramachandran plots of all different combinations of dihedral angles. Two-dimensional probability histograms of dihedral angles from simulations at zero stretching force are shown in Figure 2.6. The results support the assumption that the dihedral angle characterizing the peptide bond ω is restricted to 180°. Furthermore, we see that the other two dihedral angles, ϕ and ψ, are restricted in their rotation to different degrees, depending on the peptide type. This suggests that the parameter c in eq 2.4, which was determined from transfer-matrix calculations where two of the three dihedral angles in the peptide backbone were completely free to rotate, must be adjusted.
The relation between the force-dependent contour length $\mathrm{L}(f)$ and the unstretched contour length $\mathrm{L_0}$ follows from eq 2.1 as

$$\mathrm{L}(f) = \mathrm{L_0}\left(1 + \frac{\sqrt{\gamma_1^2 + 4\gamma_2 f} - \gamma_1}{2\gamma_2}\right) \quad \text{, for } \frac{\sqrt{\gamma_1^2 + 4\gamma_2 f} - \gamma_1}{2\gamma_2} \geq 0. \tag{2.5}$$

The large force stretching response from eq 2.4 follows as

$$\left(1 - \frac{\mathrm{z_{ete}}}{\mathrm{L}(f)}\right)^{-1} = \frac{ca_0}{k_{\mathrm{B}}T} \times f. \tag{2.6}$$

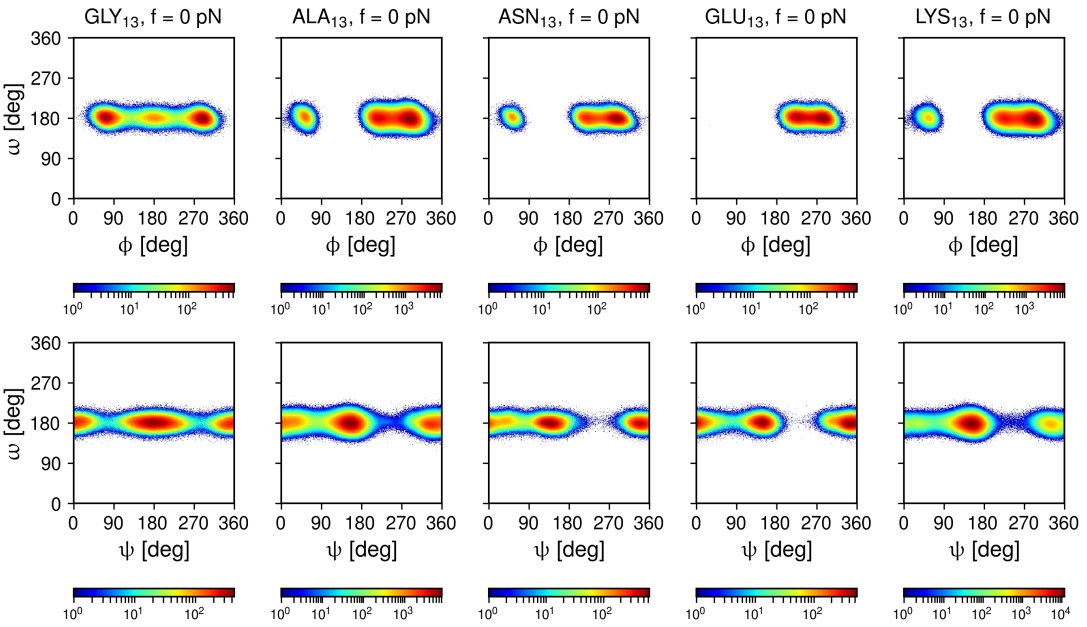

Figure 2.6: Ramachandran plots of the dihedral angles for zero stretching force demonstrate that the dihedral angle ω that characterizes rotations around the peptide bond is restricted and fixed to 180°. The other two dihedral angles, ϕ and ψ, exhibit rather broad distributions the shapes of which depend sensitively on the peptide type.

To determine the parameter c we plot $1/(1 - \mathrm{z_{ete}}/\mathrm{L}(f))$ as a function of the applied stretching force f in Figure 2.7. We use a least-square fit algorithm based on eq 2.6 for forces between 10 pN and 400 pN, since for forces above 400 pN solvation effects, finite-temperature effects and higher-order elastic effects presumably modify the dependence of the contour length $L(f)$ on force compared to the elastic response we extracted from our MD simulations of tripeptides at zero temperature. The resulting values for c are given in Figure 2.7.

Now that we have determined all parameters of the iPFRC model from simulations, which are compiled in Table 2.1, we can describe the simulated force-stretching data over the entire force range without any adjustable parameters and thereby test the applicability of the heuristic force-extension relation eq 2.4. In Figure 2.8 we present the MD simulation data by plotting the logarithm of the force versus the linear end-to-end distance divided by the force-dependent contour length $L(f)$. In Figure 2.8 a we compare data for all different polypeptides and in the other subfigures we compare data for individual polypeptides with eq 2.4. For comparison, we here also show results for previously determined values of c, as predicted from the inhomogeneous partially freely rotating chain model, $c_{\mathrm{iPFRC}} = 0.807$, and the inhomogeneous freely rotating chain model, $c_{\mathrm{iFRC}} = 0.515$.[108] Our results show that with the c values extracted by fits to the MD simulation data, which are generally higher than the previously estimated values c_{iPFRC} and c_{iFRC}, less force is needed in the intermediate regime to stretch the

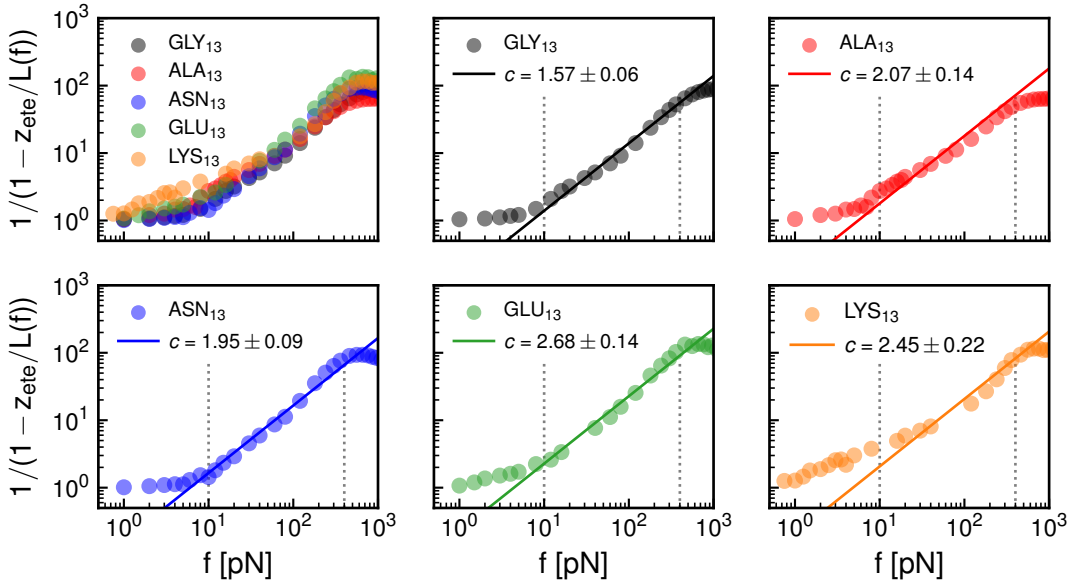

Figure 2.7: The parameter c, which determines the large-force stretching response, is determined by a least-square fit of the simulation results according to eq 2.6 (solid lines). For the contour length $L(f)$ the force-dependent expression eq 2.5 is used. The vertical dashed lines indicate the force range that is used for the fit.

peptides. This reflects the fact that previous models have neglected side-chain interactions, which of course are included in the MD simulations.
In Figure 2.9b and c we compare iPFRC modeling results (solid lines) with previously published experimental AFM results for the stretching of different single polypeptides[107] and with our MD simulation results, where we show the logarithm of the force versus the end-to-end distance z_{ete} rescaled by the unstretched contour length L_0. The experimental contour length L_0 we take from the original paper:[107] There, a fit of the experimental data in the large force regime according to $z_{ete} = L(f) \times (1 - k_B T/(2bf))$ with $b = 0.154\,\text{nm}$ was done, where $L(f)$ is given by eq 2.5 with the parameters

	a_{Kuhn}[nm]	a_0[nm]	γ_1[nN]	γ_2[nN]	c
Glycine	0.45 ± 0.02	0.368	32.3 ± 0.1	78.6 ± 0.2	1.57 ± 0.06
Alanine	0.91 ± 0.09	0.359	9.4 ± 0.3	189.9 ± 0.7	2.07 ± 0.14
Asparagine	0.35 ± 0.04	0.351	5.3 ± 0.2	137.8 ± 1.4	1.95 ± 0.09
Glutamic acid	1.49 ± 0.18	0.351	6.2 ± 0.4	137.7 ± 0.9	2.68 ± 0.14
Lysine	2.92 ± 0.15	0.349	4.0 ± 1.0	136.9 ± 1.1	2.45 ± 0.22

Table 2.1: Parameters obtained from simulations including the equilibrium monomer length a_0, the Kuhn length a_{Kuhn}, the linear and non-linear stretching moduli γ_1 and γ_2 and the parameter c of the iPFRC model.

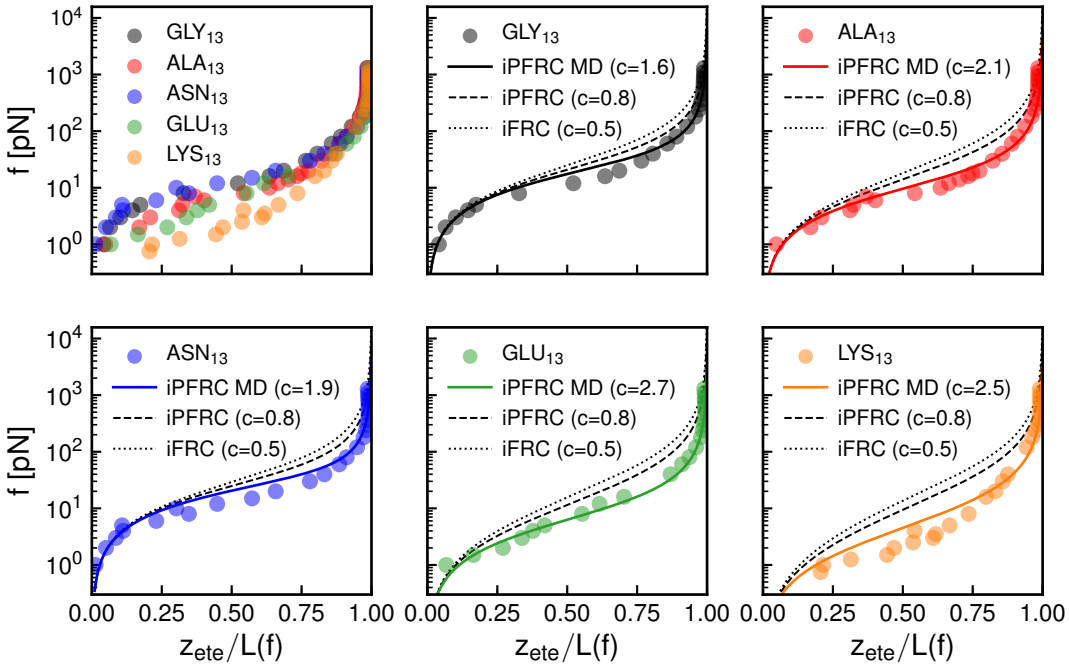

Figure 2.8: Comparison of the simulated force-stretching data to the stretching model eq 2.4 (lines). The force-dependent contour length is given by eq 2.5, for the solid lines the c parameter values are used as deduced from the MD simulations in Figure 2.7. We also show predictions using the previously determined parameter values for the iFRC and iPFRC models [108] (dotted and dashed lines).

$a_0 = 0.365\,\text{nm}$, $\gamma_1 = 27.4\,\text{nN}$ and $\gamma_2 = 109.8\,\text{nN}$. These parameters were determined previously from DFT calculations of polyglycine.[107] For the rescaling of our MD simulation results we use the parameters for a_0, γ_1, γ_2 and c as derived from MD simulations in the present paper, which for polyglycine are very similar to the parameters obtained earlier.[107] The comparison does not employ additional fit parameters. The agreement between experimental and iPFRC results in Figure 2.9b is fair over the experimentally probed force range, which primarily validates the MD force-field that was used to obtain the iPFRC parameters. Note that only one of the three experimental data sets, polylysine, corresponds to a homo-polypeptide; polyGVGVP is a repeating pentameric sequence and titin consists of a titin domain repeat, so the comparison with our homopolymeric results can strictly be done only for polylysine. In fact, the three different experimental sequences agree with each other for forces above 30 pN, where data for all three sets is available. Unfortunately, for smaller forces, where our results would predict differences between different sequences to show up, data for only polyGVGVP is available, which is seen to agree quite well with our results for polyglycine and polyasparagine. Interestingly, deviations between the experimental and modeling results appear in the force regime around 200-400 pN. The origin of this discrepancy is

unclear, we speculate that it might be related to kinetically frozen dihedral angle flips. Additional experiments that specifically probe aging and memory effects and that use different stretching rates would be highly desirable in order to understand these deviations.

In Figure 2.9d and Figure 2.9e we compare experimental and simulation data with iPFRC results on a linear force scale. Here we also show in addition the force-dependent contour length as given by eq 2.5. The contour stretching response as determined from our simulation results is shown as broken lines, the contour stretching response for glycine using the parameters determined previously by Hugel et al.[107] is shown as a dashed-dotted line, these two estimates are seen to differ only slightly. This shows that the way we compare experimental data with modeling results is consistent.

In Figure 2.9a we depict MD simulation snapshots of ALA_{13} for a few different applied forces. Only for the smallest force $f = 1$ pN are monomer-monomer contacts seen, the snapshots thus indicate that for the force range we are interested in, which is substantially larger, interactions between amino acid residues can be neglected.

Finally, we investigate the entropic and energetic contributions to the stretching free energy. The stretching free energy is calculated by integrating the force-extension relation according to $\Delta F(\mathrm{z_{ete}}) = \int_0^{\mathrm{z_{ete}}} f(\mathrm{z'_{ete}})\,\mathrm{dz'_{ete}}$. The change in internal energy ΔU is directly calculated from the simulation trajectories. The change in entropy then follows as $-T\Delta S = \Delta F - \Delta U$. All contributions are divided by the number of monomeric units and thus refer to monomeric quantities. In Figure 2.10a we show the free energy and its decomposition into internal energy and entropy. We see that the stretching response is mostly entropic in nature and that for alanine and glutamic acid a noticeable attractive energetic contribution is present. All energy curves increase steeply for large force, which in the supporting information is demonstrated to be due to backbone bond stretching and backbone angle deformation. In Figure 2.10b we show the mean number of hydrogen bonds per residue between peptides and water, $\mathrm{n_{HB}/N}$, as well as the ratio between the mean number of water-bridges and the mean number of hydrogen-bonds between peptides and water, $2\mathrm{n_{WB}/n_{HB}}$. A water bridge is defined as a water molecule that forms two hydrogen bonds with the polypeptide.[48] An example of a water bridge is shown in the inset of Figure 2.10b. We see that the number of hydrogen bonds between peptide and water does not change with the stretching force, from which we conclude by inversion that interactions with water do only have a marginal impact on the stretching response of polypeptides. This is in line with our previous observation that the stretching response of tripeptides is very similar in vacuum and in water.

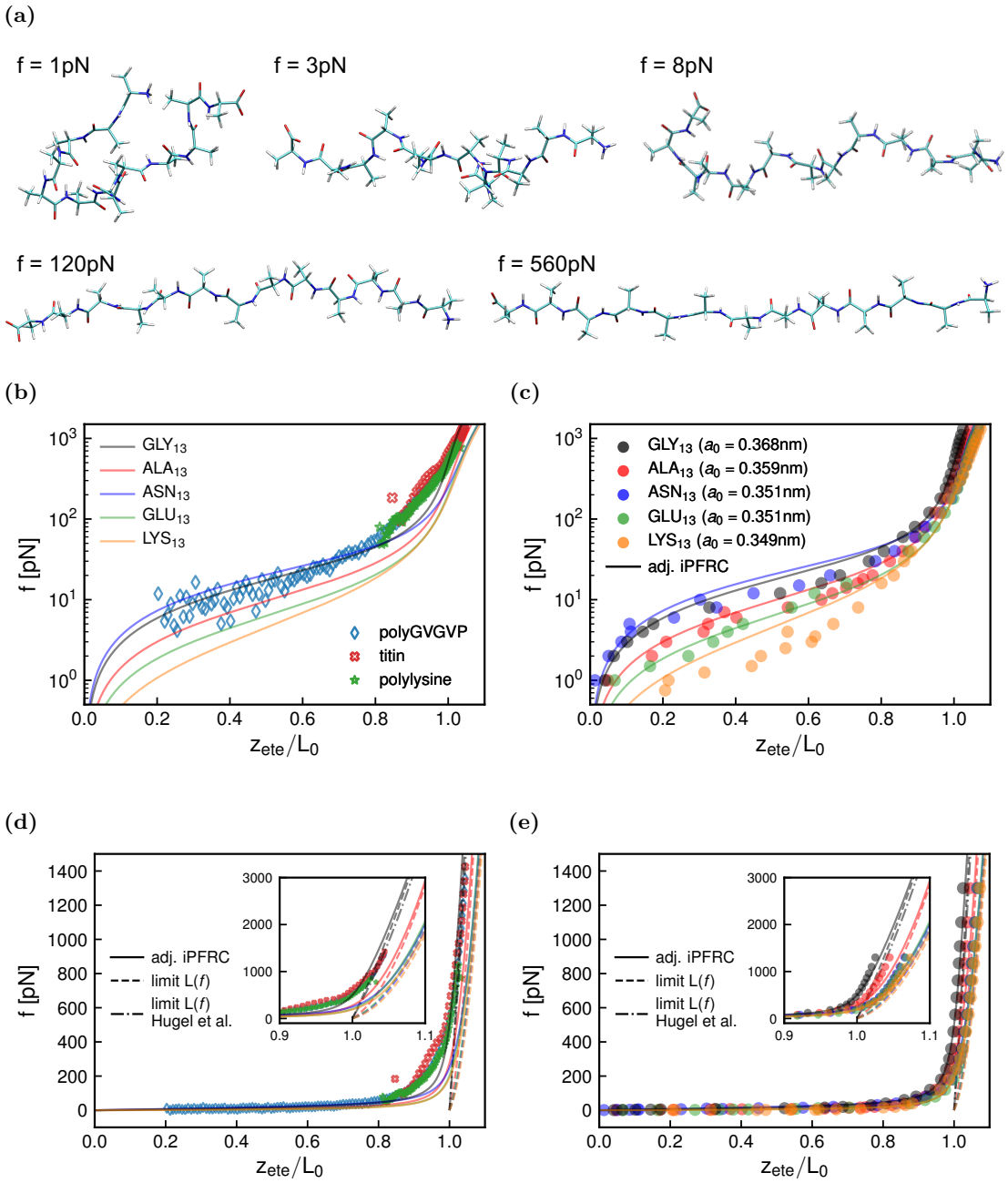

Figure 2.9: (a) Snapshots of ALA_{13} from MD simulations for several different applied forces. Comparison of the iPFRC model predictions (solid lines) with (b) experimental single polypeptide data from AFM stretching experiments [107] (open data points) and with (c) simulation data (filled data points) for the logarithm of the stretching force versus the end-to-end distance rescaled by the unstretched contour length L_0. (d) and (e): Same data as in (b) and (c) but on a linear force scale. Here in addition the force-dependent contour lengths are shown as determined in this study (dashed lines) and as determined by Hugel et al. for polyglycine [107] (dashed-dotted line).

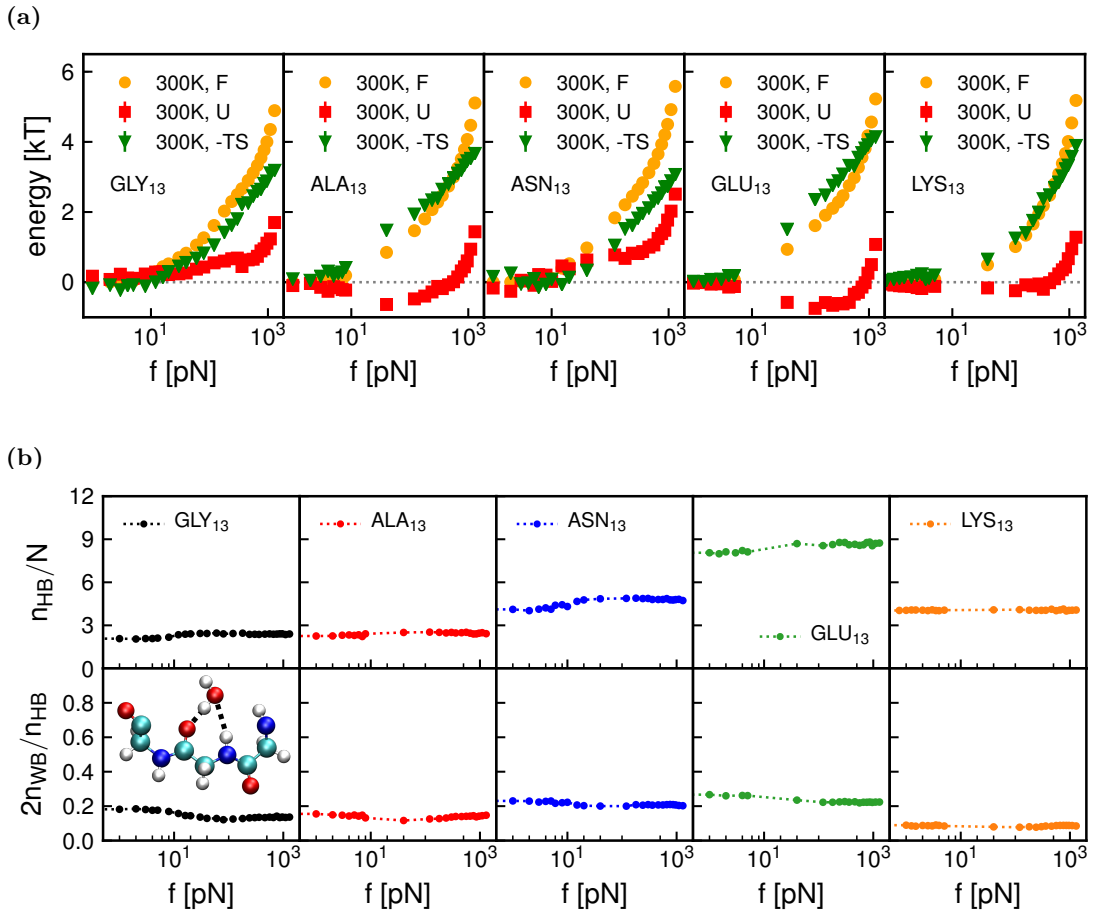

Figure 2.10: (a) The polypeptide stretching free energy is decomposed into internal energy and entropic contributions. The stretching free energy is calculated by the integral of the force-extension relation. (b) The mean number of hydrogen bonds per monomeric unit between the polypeptides and water, n_{HB}/N, is shown to change only weakly as a function of the stretching force. The force-dependent ratio between the mean number of water-bridges and the mean number of hydrogen bonds between the polypeptide and water, $2n_{WB}/n_{HB}$, depends strongly on peptide type but only weakly on stretching force.

2.3 Conclusions

We present extensive MD simulation results for the force-extension relation of five different homopeptides in explicit water and compare with the iPFRC model force-extension relation, with quantum-chemistry calculations as well as with previously published experimental AFM data. The parameters for the equilibrium monomer length a_0 and the linear and nonlinear contour length stretching moduli γ_0 and γ_1 are determined from tripeptide simulations in vacuum and in water. The Kuhn length a_{Kuhn} is ex-

tracted from the linear relation of stretching force and relative extension for 13-mers in the low-force regime. All these parameters depend strongly on the peptide type. The applicability of the inhomogeneous partially freely rotating chain (iPFRC) model is analyzed by detailed analysis of Ramachandran plots and it is shown that side-chain interactions in peptides modify the iPFRC parameter c that plays a prominent role in the high-force regime. It is shown that the iPFRC model describes the simulated force-extension very well over the entire force range without additional freely adjustable parameters. Agreement with published experimental data is good over the force range where experimental data is available, but shows significant deviations in the mid-force regime around 200-400 pN, which suggests further experimental studies in the future. We thus demonstrate that if all relevant parameters such as the equilibrium monomer length, the Kuhn length, the iPFRC parameter c and the stretching moduli are determined, the global force-stretching relation of peptides can be quantitatively predicted. This will help to interpret polypeptide force-extension relations measured experimentally in different applications and scenarios. The stretching of the contour length is important in the high-force regime. The effect of amino-acid interactions is expected to show up in the low-force regime and can be included by incorporating existing scaling models.[115,116] A decomposition of the stretching free energy into energetic and entropic contributions shows that peptide stretching is mostly entropic, which is different from previous results found for PEG.[48,71] This result is rationalized by an analysis of the number of hydrogen bonds between water and peptide and of the number of water-bridges, which depend very little on the applied force.

2.4 Methods

All MD simulations are performed using the Gromacs simulation package version 5.1.5, some simulations were additionally done with the version 2016.1.[120] The time step is set to 2 fs, the temperature is set to 300 K and the pressure is set to 1 bar with a water compressibility of $4.5 \times 10^{-5}\,\mathrm{bar}^{-1}$. For temperature coupling we use the v-rescale[121] and for pressure coupling the Parrinello-Rahman[122] algorithm with relaxation times of 0.1 ps and 0.5 ps, respectively. All simulations are performed using periodic boundary conditions. The cut-off for non-bonded interactions is set to 1.0 nm. The particle mesh Ewald method[123] is used to calculate the long-range electrostatic interactions. Except for the tripeptide calculations, all homopeptides investigated consist of 13 amino acids. The first and last C_α atoms along the backbone are the anchor points for constant forces that are applied in opposite directions in the z-direction. The polypeptides are simulated in a box with dimensions of 4.5 nm in x- and y- and 12.5 nm in z-direction. Production runs for low forces have a simulation time of up to 830 ns, for high forces the simulations times are at least 200 ns. The mean end-to-end distance z_{ete} in stretching-direction is defined by the time average over the distance in z-direction between the first and the last C_α atom of the backbone of the polypeptide as $z_{ete} = \langle z_{C_\alpha^1 - C_\alpha^{13}} \rangle$. We simulate polyalanine, polyasparagine, polyglutamic acid, polyglycine and polylysine.

The caps of the polypeptides are chosen in the zwitterionic form. All polypeptides are simulated using the amber99sb force field.[124] The bond lengths are not constraint. In the initial configuration of the simulations the dihedral angles are all 180°, which for GLY_{13} corresponds to a length of $z_{C_\alpha^1 - C_\alpha^{13}} = 4.38\,\text{nm}$. Initial configurations are created with Avogadro.[125] The exported pdb file is converted to Gromacs input files using pdb2gmx. For the polypeptides with charged side chains, such as polylysine and polyglutamic acid, all side chains are charged. The system is neutralized by inserting the same number of counter ions Na^+ or Cl^-. Simulations with added salt are shown in the supplementary information. For water, the recommended force field tip3p is used.[126] To equilibrate the system before production runs, an energy minimization followed by a 1 ns NPT simulation is performed. For a given polypeptide, the same equilibrated configuration is used for initializing all production runs at different forces. We analyzed the auto-correlation function of the end-to-end separation to confirm that the relaxation time is much smaller than the simulation time. From the ratio of simulation times and relaxation times the number of uncorrelated configurations is estimated, which is then used for the calculation of the standard error of expectation values. For the hydrogen bond analysis, a donor-acceptor distance cutoff of 3.5 Å and an angle cutoff of 150° is used, which agrees with cutoffs used in the definition of strong hydrogen bonds.[127–129] The number of hydrogen bonds between water and the polypeptide is analyzed every 0.2 ns using the tools `MDAnalysis.analysis.hbonds.hbond_analysis`.[130,131] A water molecule that forms two hydrogen bonds with the polypeptide is denoted as a water bridge.

For the umbrella simulations, tripeptides are put in a $2.5\times2.5\times2.5\,\text{nm}^3$ box with 503 water molecules. After energy minimization, the box is equilibrated for 1 ns in an NPT simulation. Afterwards, a harmonic potential with a force constant of $200\,000\,\text{kJ}/(\text{mol nm}^2)$ is applied between the first and the last C_α atoms. The minimum of the harmonic potential is varied between 0.50 nm and 0.80 nm in steps of 0.01 nm. The number of windows is therefore given by 30. The simulations are analyzed using the WHAM algorithm.[132]

For the estimate of the force response of a monomer in vacuum, we perform energy minimizations in double precision, where a single stretched tripeptide is put in a $2.5 \times 2.5 \times 2.5\,\text{nm}^3$ box without any water molecules. The distance $2a$ between the first and the last C_α atoms is constrained during each energy minimization. For each value of $2a$ we perform two indepedent minimizations using the steepest descent method and using the conjugate gradient method and choose the result that gives the lower energy, which helps to avoid the pitfall of being stuck in a local energy minimum. We then change the value of $2a$ in steps of 0.01 nm and use the result from the previous minimization as starting point. By starting from various different initial configurations, we ensure to obtain the lowest energy structures for all values of $2a$. For steepest descent, the maximum step size is set to 0.01 nm and the maximum tolerance is set to $1\,\text{kJ}/(\text{mol nm})$. The same tolerance value is used for the conjugate gradient method. The dielectric constant for the energy minimization is set to the bulk value of tip3p water, which we found to be 106 at 300 K. This value matches reasonable well the

reported value of 97 ± 7 by Höchtl et al.,[133] which was simulated with AMBER 4.1[134] in a box with 2.5 nm side length.
In order to support the results from classical simulations and exclude the possibility that differences between glycine and other peptides are force-field specific effects, density functional theory (DFT) calculations are performed. The tripeptide structures are simplified compared to the MD simulations by substituting the capping groups for neutral methyl groups ($CH_3-NH-CO-CR-NH-CO-CH_3$). We limit the computations to two systems, glycine and alanine. Energy minimizations of the structures in vacuum at fixed separations between the C atoms of the caps are performed for several values around $2a = 0.73$ nm, starting from optimized geometries of the corresponding classical simulations. For the DFT calculations, we use the CP2K 4.1 environment with a correlation-consistent polarized triple-zeta basis set augmented with diffuse functions, the BLYP exchange-correlation functional and D3 dispersion corrections.[135–137]

Chapter 3

Quantification of the Frequency-Dependent Signal Transduction for the Coiled Coil Linker Jα

Bibliographic information: The content of this chapter is in preparation to be submitted to a peer-reviewed journal (Ref. [ii]).

Author contribution statement: Richard Schwarzl carried out all simulations and the analysis of the data. Roland R. Netz supervised the project. Richard Schwarzl created all figures and wrote the manuscript, which has not been handed in for publication yet.

3.1 Introduction

Physiological responses to stimuli constitute a major inherent regulatory concept in biology. Prime examples are cell regulation[138–140] and differentiation.[141–143] At the molecular level, such regulatory processes involve signal receptors (sensors) which can perceive environmental changes (e.g., light, pH, hormones) and corresponding effectors which are responsible for sparking a response.[144–146] Sensors and effectors can usually be assigned to distinct domains of proteins.[145] Improvements of experimental techniques, e.g., in the field of fluorescence resonance energy transfer (FRET),[147,148] triggered a shift of the focus to the investigation of designated signaling pathways on a molecular level.[72,149–155] The combination of spectroscopy techniques and all atom molecular dynamics simulation description has led to recent insights into time-resolved processes of allosteric regulation.[156–159]
In this study we investigate different structural signal transmission mechanisms based on the two-component signaling motif of light-regulated histidine kinases by Möglich, et al.[72] The design is based on the light-oxygen-voltage (LOV) histidine kinase YF1.[72,73] Coiled coil systems are a frequently suggested signal transduction motif.[160–166]

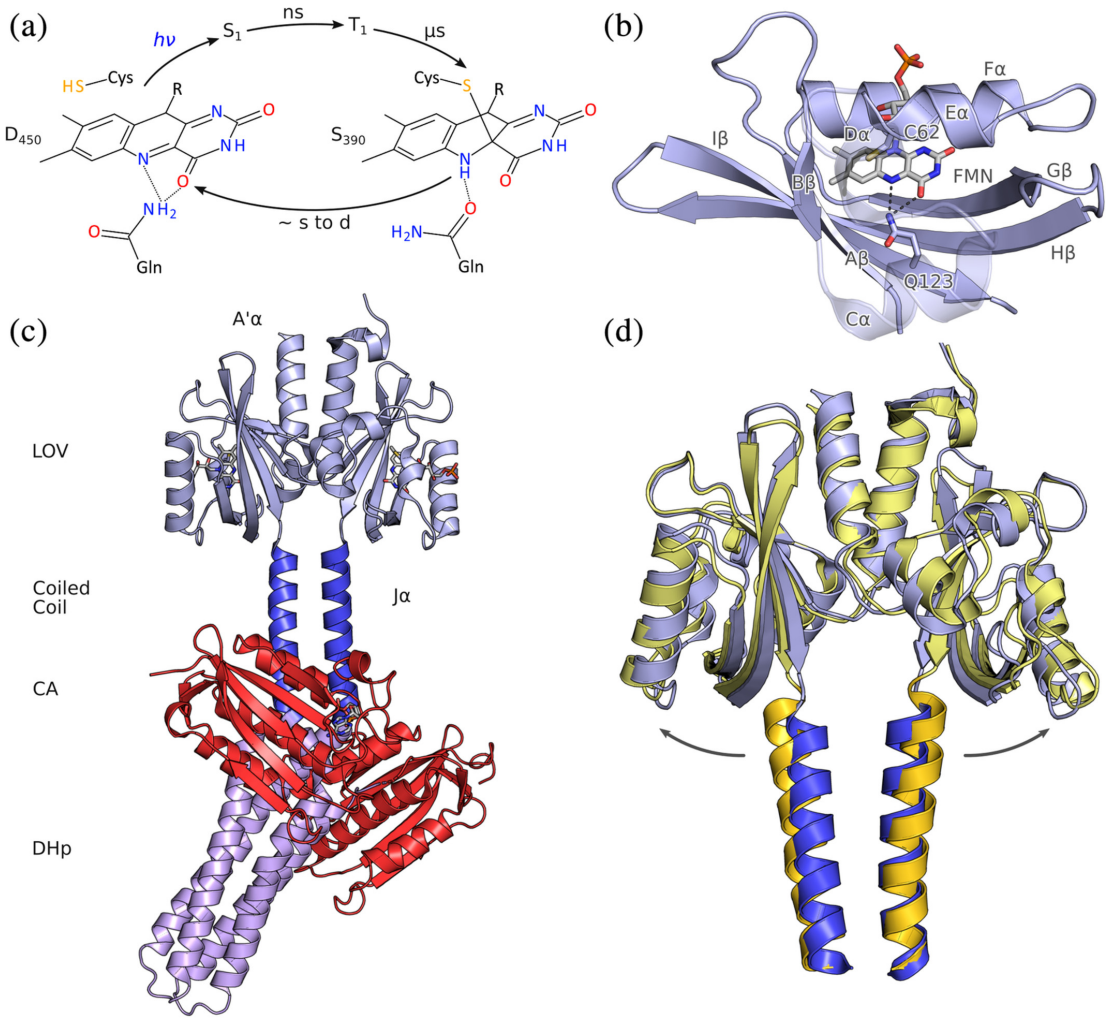

Figure 3.1: **Photochemistry, structure, and signaling of light-oxygen-voltage (LOV)-histidine kinases.** (a) The dark-adapted state D_{450} with its flavin-nucleotide chromophore in the oxidized quinone state absorbs blue light and then passes through short-lived electronically excited singlet and triplet states. A covalent bonds forms between a conserved cysteine residue and atom C4a of the flavin, thus giving rise to the metastable signaling state S_{390} , which thermally decays to D_{450} over seconds to many hours, depending on residues adjacent to the chromophore. (b) As a subfamily of the Per-ARNT-Sim domains, LOV sensor domains exhibit a compact fold with a five-stranded antiparallel β sheet and several α helices that together coordinate the flavin chromophore. (c) The full-length structure of the dark-adapted LOV histidine kinase YF1 (PDB 4GCZ). (d) Based on electron paramagnetic resonance spectroscopy and X-ray solution scattering, the light-induced conformational changes within the dimeric LOV sensor have been identified as a splaying apart of the sister monomers. The N termini of the Jα helices that form the coiled coil linker are thus moved apart by around 3 Å in the light (yellow) relative to the dark (blue).
Note: Figure and caption are taken from Möglich 2019 [73] as a reference of the investigated coiled coil section Jα. Reprinted from A. Möglich, Signal transduction in photoreceptor histidine kinases, Protein Science 28, 1923-1946 (2019), `https://doi.org/10.1002/pro.3705`. Copyright 2019 by Andreas Möglich, Protein Science published by Wiley Periodicals, Inc. on behalf of The Protein Society. Reprinted with permission. License: CC BY.

To investigate the fundamental mechanism of structural signaling through a coiled coil linker, we perform molecular dynamics (MD) simulations of the coiled coil linker, which has previously been experimentally investigated by Möglich, et al.[72] This linker consists of two α-helices (c.f. Figure 3.1). It is referred to as Jα and connects two parts of a fusion protein that is built up by the histidine kinase complex from Bradyrhizobium japonicum and the LOV sensor domain from Bacillus subtilis YtvA.[72] In our simulations, the linker is studied without the environment of the adjacent sensor and effector domains. Each α-helix has the sequence ITEHQQTQARLQELQSELVHVSR The N-terminus of the helices at the side of ILE is NH_2 and the C-terminus at ARG is an N-Methylamide C-terminus (CT_3) which is given by $CO-NH-CH_3$. The charge of the NH_2 terminus is artificially put to zero such that both termini are neutral in charge. Charged residues of the sequence are the two GLU ($-e$) and the ARG ($+e$) resulting in a total charge of $-e$ per α-helix. Hence, the solute contains two sodium counter ions to ensure zero total charge of the system. The two α-helices are initially arranged parallel in the simulation box but are not additionally constrained throughout the simulation. We provide further information on how we prepare and conduct the simulations in the Methods section. A screenshot from simulations of the linker is shown in Figure 3.2a without the solute.

From MD simulations results, we investigate three possible relative motions of the two coils as modes of signal transmission, namely shift, splay, and twist (cf. Figures 3.2c and 3.2d). All three modes will be defined in the beginning of the Results section of this study. The self- and cross-correlations of the two shift, the two splay, and the twist components are calculated and the numerical derivatives of the results, which correspond to the time-resolved response functions of a designated modes, are transferred into Fourier space. Ratios of the self- and the cross-response in Fourier space yield the transmission function, which states the effectiveness of signal transduction from the N terminal side to the opposing C terminal side of the linker through a designated relative motion depending on the frequency of the driving force. Experimental investigations have given rise to the proposed signal transduction pathway of a splay motion (c.f. Figure 3.1).[73] Based on the frequency dependent force-transmit functions deduced from our simulation, we find that the splay mode provides a rather low value of force-transmission and that the force-transmission of the twist and shift mode are larger by a factor between five and ten depending on the frequency range. Therefore, the numerical results from MD simulations alone suggest the twist and shift mode to be a more likely pathway for signal transduction. However, we point out that we neglected the adjacent sensor and effector domains in our simulations.

We describe the numerical results with multi-exponential functions as a heuristic ansatz based on the deconvolution theory by Hinczewski, et al.[167] to extract correlation strengths and correlation times relevant for the modes shift, splay, and twist. These parameters yield analytic expressions for the frequency dependent response functions and consequently also the transmission functions, which can help to interpret noisy regions of the numerical result.

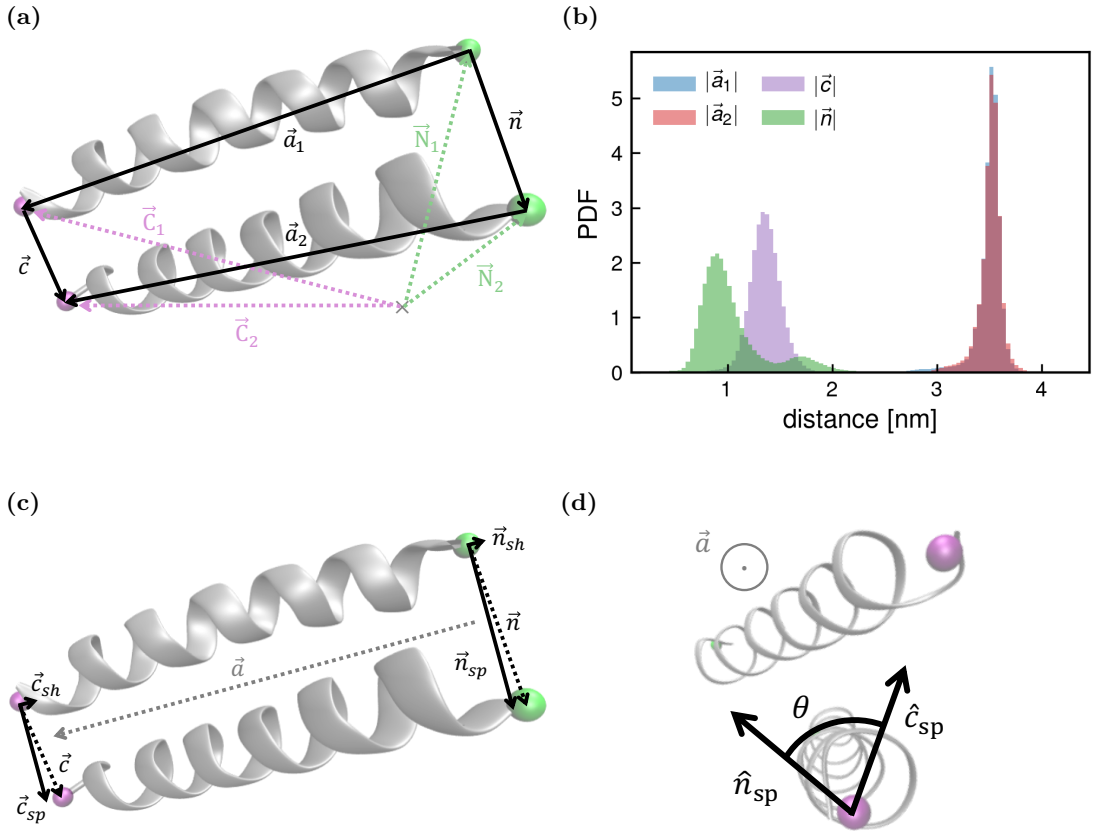

Figure 3.2: (a) A screenshot of the simulated coiled coil system together with the position vectors of the end-termini as well as difference vectors describing the distances between end-termini. (b) Histograms of the distances defined in (a) are shown as evidence for the stability of the system over the course of the simulation length of 10 μs. Note that the distributions of $|\vec{a}_1|$ and $|\vec{a}_2|$ overlap. (c) The schematics of the definitions of shift and splay as the parallel and perpendicular components of $\vec{c}$ and $\vec{n}$ with respect to the symmetrized axis $\vec{a} = (\vec{a}_1 + \vec{a}_2)/2$ and (d) the twist, which is defined based on the scalar product of the two unit vectors $\hat{c}_{\mathrm{sp}}$ and $\hat{n}_{\mathrm{sp}}$.

3.2 Results

For the description of the dynamics of the two α-helices of the linker Jα, we define the position vectors $\vec{\mathrm{C}}_i$ of the C-terminal CH_3 and $\vec{\mathrm{N}}_i$ of the N-terminal NH_2, where $i = 1, 2$ refers to the first or second α-helix. The vectors are used to construct the distance vectors $\vec{c} = \vec{\mathrm{C}}_2 - \vec{\mathrm{C}}_1$, $\vec{n} = \vec{\mathrm{N}}_2 - \vec{\mathrm{N}}_1$ and $\vec{a}_i \equiv \vec{\mathrm{C}}_i - \vec{\mathrm{N}}_i$ as shown in Figure 3.2a. To check the stability of the simulated system, we extract the probability density function (PDF) of each of the distance vector lengths c, n and a_i. The results are shown in Figure 3.2b and confirm a stable attraction between the two chains. The two peaks in the distribution of n relate to the interactions of a single sodium ion with the ARG residue at the N-termini. Starting from the end-to-end axes $\vec{a}_i$ of the helices, we define

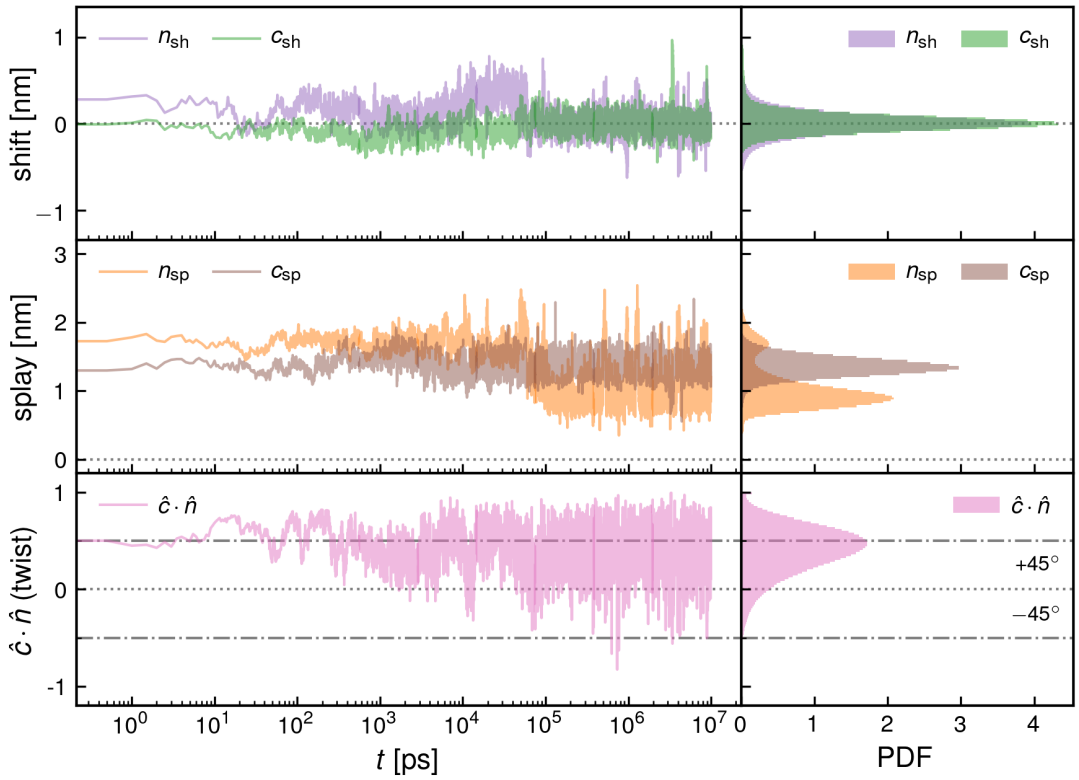

Figure 3.3: Time series and corresponding probability density functions for the scalar shifts, splays and the cosine of the twist angle.

the mean-axis $\vec{a} = (\vec{a}_1 + \vec{a}_2)/2$. With respect to that reference-axis $\vec{a}$, we separate $\vec{c}$ into a shift

$$\vec{c}_{\mathrm{sh}} = (\vec{c} \cdot \hat{a}) \cdot \hat{a} \tag{3.1}$$

and a splay

$$\vec{c}_{\mathrm{sp}} = \vec{c} - \vec{c}_{\mathrm{sh}} \tag{3.2}$$

contribution as shown in Figure 3.2c. $\hat{a}$ denotes the unit vector of $\vec{a}$. The same is done for $\vec{n}$ and consequently referred to as $\vec{n}_{\mathrm{sh}}$ and $\vec{n}_{\mathrm{sp}}$. Finally, the twist θ of the two coils is defined based on the scalar product of the two unit vectors $\hat{c}_{\mathrm{sp}}$ and $\hat{n}_{\mathrm{sp}}$ by means of

$$\cos\theta = \hat{c}_{\mathrm{sp}} \cdot \hat{n}_{\mathrm{sp}} \ , \tag{3.3}$$

which for $0° \leq \theta \leq 60°$ can be written as $\theta \approx \sqrt{2 \cdot (1 - \cos\theta)} = \sqrt{2 \cdot (1 - \hat{c}_{\mathrm{sp}} \cdot \hat{n}_{\mathrm{sp}})}$. Schematics of the definition of the twist measure are shown in Figure 3.2d. Before the analysis, we reduce the shift to the scalar $c_{\mathrm{sh}} \equiv |\vec{c}_{\mathrm{sh}}|$ and the splay to $c_{\mathrm{sp}} \equiv |\vec{c}_{\mathrm{sp}}|$. Interchanging c with n yields the shift $n_{\mathrm{sh}} \equiv |\vec{n}_{\mathrm{sh}}|$ and splay $n_{\mathrm{sp}} \equiv |\vec{n}_{\mathrm{sp}}|$ at the N-terminus. The twist is a scalar quantity by definition. In Figure 3.3, we show the time-series as well as histograms of these quantities over the total simulation period

of 10 μs. We see shifts around zero and splays between 0.5 nm and 2 nm. The twist predominantly resides in the range of 45°.

After having defined shifts, splays and twist, we introduce the self- and cross-correlation functions. We adopt the references to sensor (s) and effector (e) which correspond to the N-terminal and the C-terminal ends of the linker. $C_{\text{self}}^{\text{sh, s}} = \langle c_{\text{sh}}(0)\, c_{\text{sh}}(t)\rangle$ and $C_{\text{self}}^{\text{sh, e}} = \langle n_{\text{sh}}(0)\, n_{\text{sh}}(t)\rangle$ define the self-correlation functions of the shifts c_{sh} and n_{sh}. The cross-correlation function is symmetric and can therefore be written as $C_{\text{cross}}^{\text{sh, s}\to\text{e}} = \langle n_{\text{sh}}(0)\, c_{\text{sh}}(t)\rangle$ or $C_{\text{cross}}^{\text{sh, e}\to\text{s}} = \langle c_{\text{sh}}(0)\, n_{\text{sh}}(t)\rangle$. Hence, we define the average of the symmetric cross-correlation functions as $C_{\text{cross}}^{\text{sh}} = \left(C_{\text{cross}}^{\text{sh, s}\to\text{e}} + C_{\text{cross}}^{\text{sh, e}\to\text{s}}\right)/2$. The correlation functions for the splays are defined by interchanging the shift quantities by the related splay quantities, e.g. $C_{\text{self}}^{\text{sp, s}} = \langle c_{\text{sp}}(0)\, c_{\text{sp}}(t)\rangle$. For the twist, we define the self- and cross-correlation functions by the scalar product of the splay unit vectors. The self-correlation functions can be written as $C_{\text{self}}^{\text{tw, s}} \equiv \langle \hat{n}_{\text{sp}}(0)\cdot\hat{n}_{\text{sp}}(t)\rangle$, $C_{\text{self}}^{\text{tw, e}} \equiv \langle \hat{c}_{\text{sp}}(0)\cdot\hat{c}_{\text{sp}}(t)\rangle$ and the cross-correlation function is written as either $C_{\text{cross}}^{\text{tw, s}\to\text{e}} \equiv \langle \hat{n}_{\text{sp}}(0)\cdot\hat{c}_{\text{sp}}(t)\rangle$ or $C_{\text{cross}}^{\text{tw, e}\to\text{s}} \equiv \langle \hat{c}_{\text{sp}}(0)\cdot\hat{n}_{\text{sp}}(t)\rangle$, which leads to an average cross-correlation function $C_{\text{cross}}^{\text{tw}} \equiv \left(C_{\text{cross}}^{\text{tw, s}\to\text{e}} + C_{\text{cross}}^{\text{tw, e}\to\text{s}}\right)/2$. Based on linear response theory and the fluctuation-dissipation-theorem, these correlation functions can be used to calculate the corresponding response functions via the time-derivative of respective correlation function as[167,168]

$$J(t) = -\frac{1}{k_{\text{B}}T}\,\frac{\text{d}}{\text{d}t}C(t) \quad . \tag{3.4}$$

These response functions J are later used to describe the shift, splay, and twist displacements in Fourier space in dependence of periodic forces applied to the sensor and effector site (c.f. eqs 3.5 and 3.6). Each response function inherits in its notation sub- and superscripts of C, e.g., $J_{\text{self}}^{\text{sh, s}}(t) = -\frac{1}{k_{\text{B}}T}\frac{\text{d}}{\text{d}t}C_{\text{self}}^{\text{sh, s}}(t) = -\frac{1}{k_{\text{B}}T}\frac{\text{d}}{\text{d}t}\langle c_{\text{sh}}(0)\, c_{\text{sh}}(t)\rangle$. The results for the correlations functions and their respective time-derivatives are shown in Figure 3.4. To avoid any complications for the upcoming Fourier-transformation of the derivative of the correlation function, we define a threshold from which on we pad the time-derivative correlation function by zero up to 10 μs. This threshold is defined individually for each type of relative motion (e.g., shift or splay) and indicates where all correlation derivatives have fallen below zero for the first time, thus corresponding to the point where the noise is dominating. We see that all time-derivatives of the correlation functions smoothly go to zero. The longest correlation is observed for the twist.

For the following discussion, it will be useful to take the Fourier-transform of the previously defined response functions. Whenever we refer to a Fourier-transform of a response function, we will denote this by using a tilde, e.g., $\tilde{J}_{\text{self}}^{\text{sh, s}}$. The response functions corresponding to the time-derivatives shown in Figure 3.4 are easily calculated using an FFT algorithm. The results are split into a real, e.g., Re $\tilde{J}_{\text{self}}^{\text{sh, s}}$, and an imaginary part, e.g., Im $\tilde{J}_{\text{self}}^{\text{sh, s}}$. In Figure 3.5, we show both for each of the correlation-function derivatives shown in Figure 3.4.

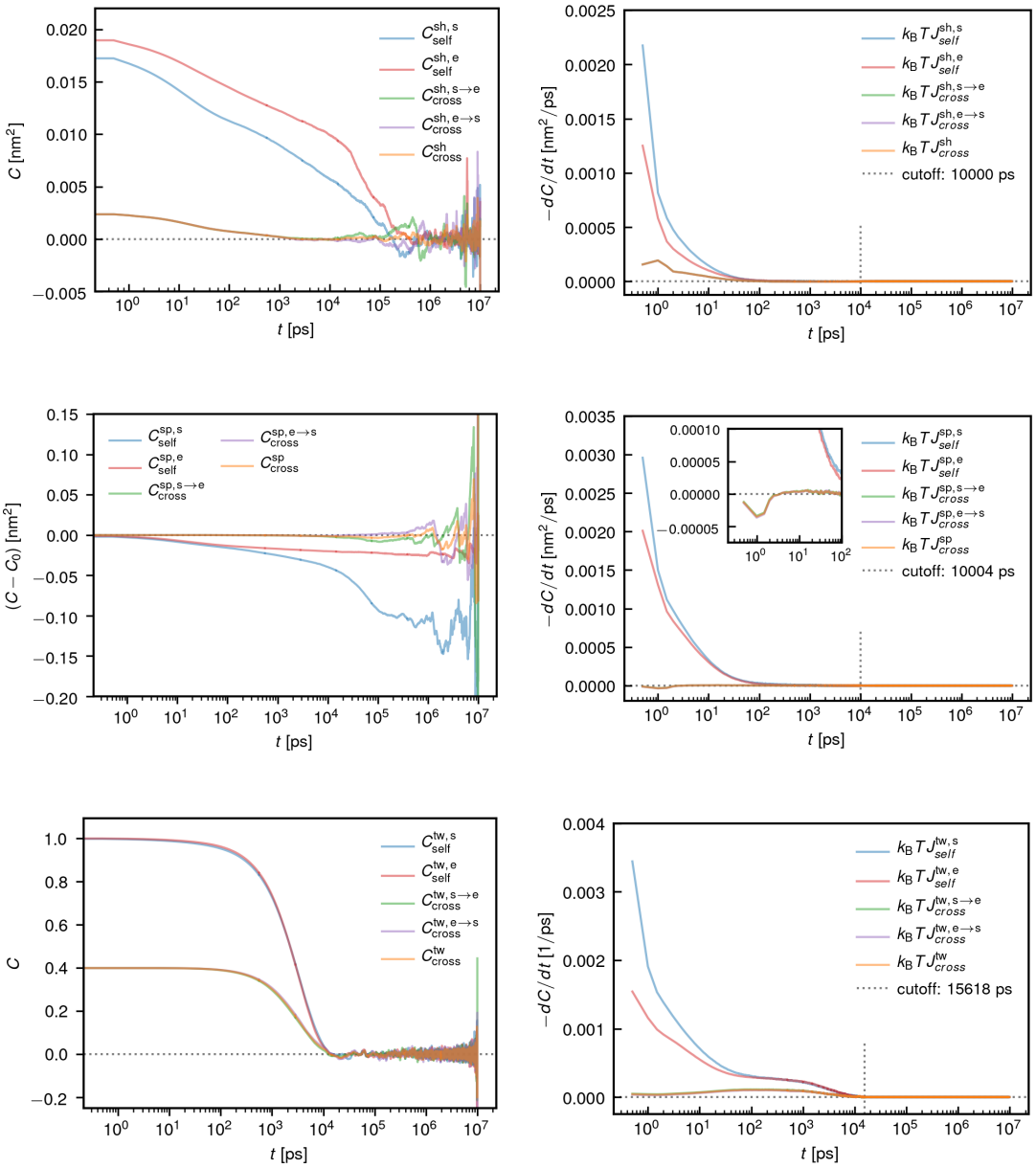

Figure 3.4: Left: Results for the self- and cross-correlation functions for shift, splay, and twist. For the splay, we have to subtract $C_0 = C(t = 0\,\mathrm{s})$ to be able to compare all correlation functions in one graphic. Right: Results for the numerical time derivative of the correlation functions, shown on the left, padded by zero for $t > t_{\mathrm{th}}$, where the threshold t_{th} (indicated by a vertical dotted line) is defined by a common time that satisfies $\mathrm{d}C/\mathrm{d}t \leq 0$ and $t_{\mathrm{th}} > 10\,\mathrm{ns}$. This approach is used to prevent analysis of the noise dominated section of the correlation functions.

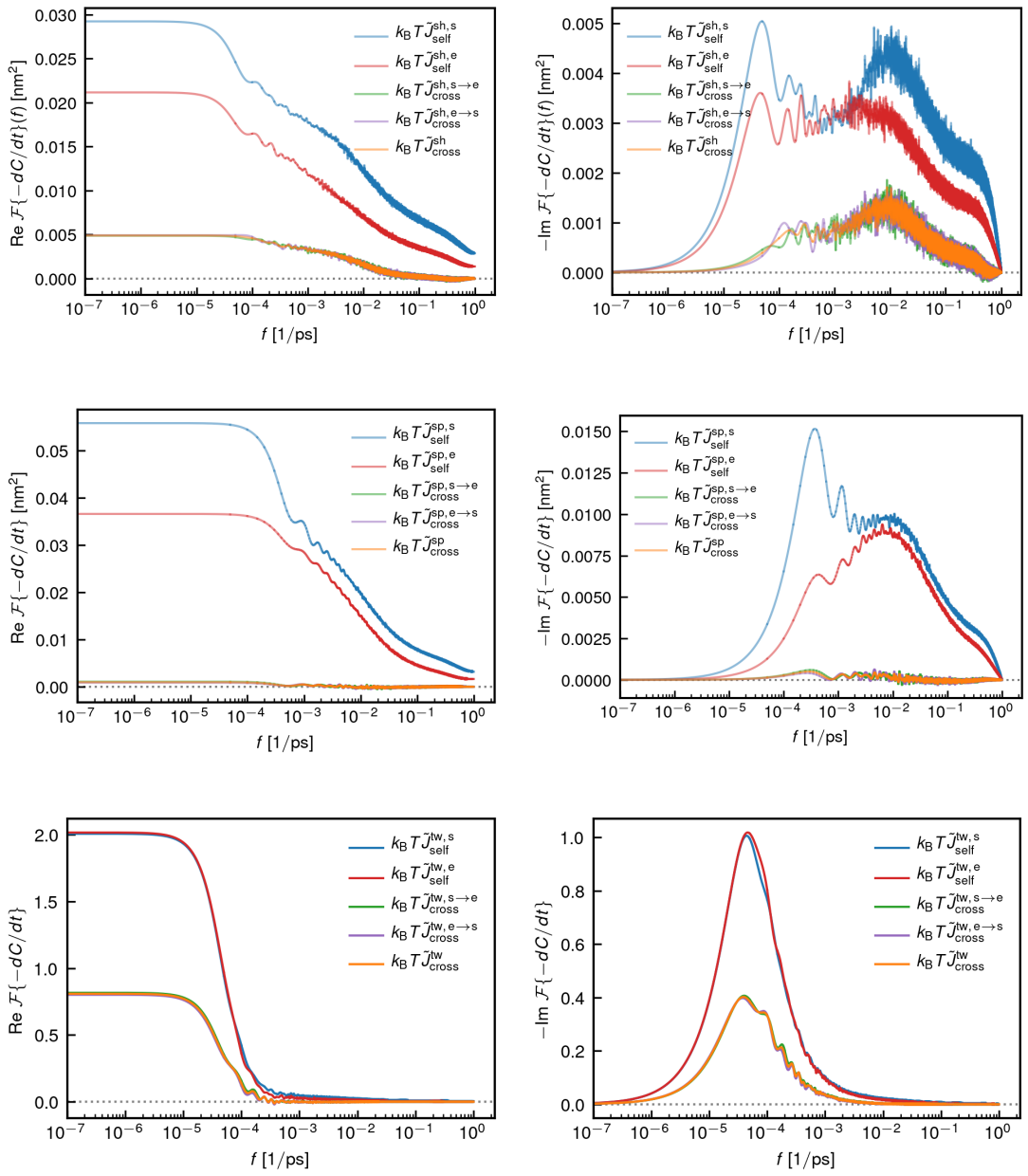

Figure 3.5: FFT transforms of the padded correlation-function derivatives (cf. Figure 3.4) reveal the structure of the individual response function in Fourier space.

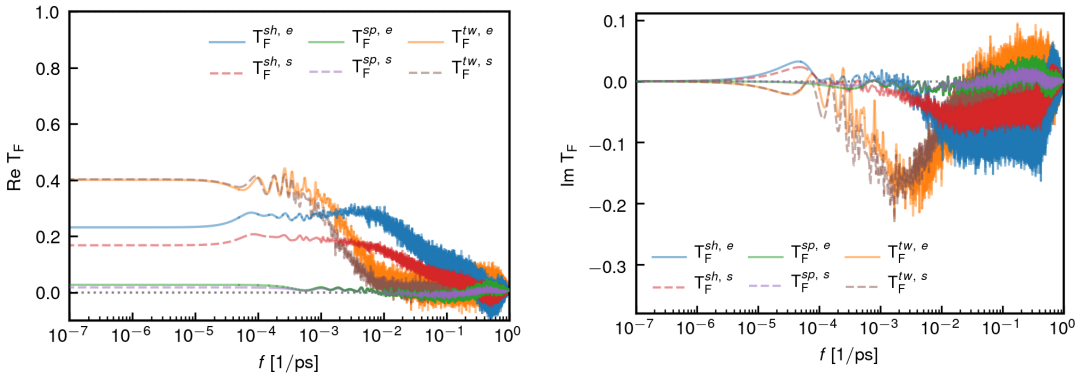

Figure 3.6: Numerical results for the force-transmit functions defined in eq 3.7 from the ratio of evaluated response functions (cf. Figure 3.5).

In the following, we will use the knowledge of the response functions in Fourier space to define transmit functions. We will start with an example derivation of such a transmit function. Let us assume we have a periodic force $\tilde{F}_\mathrm{s}(2\pi f)$ that drives the sensor side of the linker. At the same time, a force $\tilde{F}_\mathrm{e}(2\pi f)$ drives the effector attached side of the linker. The forces would engage a response at the sensor as well as at the effector side, which in Fourier space can be written as

$$\tilde{n}_\mathrm{sh} = \tilde{J}^{\mathrm{sh,\ s}}_{\mathrm{self}}\,\tilde{F}_\mathrm{s} + \tilde{J}^{\mathrm{sh}}_{\mathrm{cross}}\,\tilde{F}_\mathrm{e} \quad , \tag{3.5}$$

$$\tilde{c}_\mathrm{sh} = \tilde{J}^{\mathrm{sh,\ e}}_{\mathrm{self}}\,\tilde{F}_\mathrm{e} + \tilde{J}^{\mathrm{sh}}_{\mathrm{cross}}\,\tilde{F}_\mathrm{s} \quad . \tag{3.6}$$

The idea of a force-transmit function is to define the ratio between a "real" driving force on one side and a "virtual" force on the other side acting such that the resulting response is exactly zero. One example of a force-transmit function is derived by putting $\tilde{c}_\mathrm{sh}$ in eq 3.6 to zero. The resulting equivalent ratios define the corresponding force-transmit function

$$\mathrm{T}^{\mathrm{sh,\ e}}_{\mathrm{F}} = \frac{-\tilde{F}_\mathrm{e}}{\tilde{F}_\mathrm{s}} = \frac{\tilde{J}^{\mathrm{sh}}_{\mathrm{cross}}}{\tilde{J}^{\mathrm{sh,\ e}}_{\mathrm{self}}}. \tag{3.7}$$

Solving eq 3.5 for $\tilde{n}_\mathrm{sh} = 0$, we obtain the definition of the other force-transmit function with respect to shift as $\mathrm{T}^{\mathrm{sh,\ s}}_{\mathrm{F}} \equiv \tilde{J}^{\mathrm{sh}}_{\mathrm{cross}}/\tilde{J}^{\mathrm{sh,\ s}}_{\mathrm{self}}$. In an analogous fashion, the force-transmit functions for splay and twist are defined. The numerical results for all six force-transmit functions are shown in Figure 3.6. We see that for lower frequencies (up to $1 \times 10^{-3}\,\mathrm{ps}^{-1}$) the twist pathway is most efficient for force-transmission, whereas for higher frequencies (between $1 \times 10^{-3}\,\mathrm{ps}^{-1}$ and $1 \times 10^{-1}\,\mathrm{ps}^{-1}$) the shift pathway becomes dominant. Splay seems to have a negligible impact on the force-transmission.

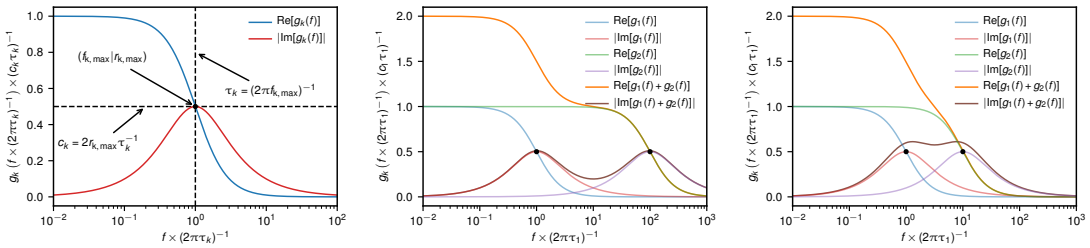

Figure 3.7: (a) General course of the absolute values of the real and imaginary part of a single exponential function. (b) Linear combination of two single exponential functions, where $\tau_2 = \tau_1 \times 10^{-2}$ and $c_2 = c_1 \times 10^2$. (c) Linear combination of two single exponential functions, where $\tau_2 = \tau_1 \times 10^{-1}$ and $c_2 = c_1 \times 10^1$. The narrower the gap between the maxima, the more difficult the estimates become.

3.2.1 Correlation Parameter Analysis of the Response in Fourier Space

In the following, we characterize the response functions in terms of correlation strengths and correlation times. Therefore, we assume a multiple exponential function for each correlation, which can be written as

$$c(t) = \theta(t) \times \sum_{k=1}^{N} c_k \, \exp\left(-t/\tau_k\right) = \sum_{k=1}^{N} g_k(t) \ , \tag{3.8}$$

where θ the Heaviside step function. The Fourier-transform of each summand is given by

$$g_k(\omega) = \frac{c_k}{\tau_k^{-1} + i\omega} = \frac{c_k \ (\tau_k^{-1} - i\omega)}{\tau_k^{-2} \ (1 + \omega^2\tau_k^2)} = \frac{c_k \ \tau_k}{1 + \omega^2\tau_k^2} - i \ \frac{c_k \ \tau_k^2 \ \omega}{1 + \omega^2\tau_k^2} \tag{3.9}$$

For each summand, we obtain a contribution to the real part of the fit function in terms of the frequency given as

$$\mathrm{Re}\left[g_k(f)\right] = \frac{c_k\tau_k}{1 + 4\pi^2\tau_k^2 \ f^2} \ , \tag{3.10}$$

and an imaginary part given as

$$\mathrm{Im}\left[g_k(f)\right] = -\frac{2\pi c_k\tau_k^2 \ f}{1 + 4\pi^2\tau_k^2 \ f^2} \ , \tag{3.11}$$

where $k \in \{1, 2, 3, \dots\}$ refers to the first, second, third summand in eq 3.9, respectively. Each contribution g_k to the response function has a distinct shape in Fourier space, which general form is shown in Figure 3.7. The frequency $f_{k,\max}$, at which $|\mathrm{Im}\left[g_k\right]|$ takes its maximum value $|\mathrm{Im}\left[g_k(f_{k,\max})\right]| \equiv r_{k,\max}$, reveals the correlation time by

$$\tau_k = \left(2\pi f_{k,\max}\right)^{-1} \ , \tag{3.12}$$

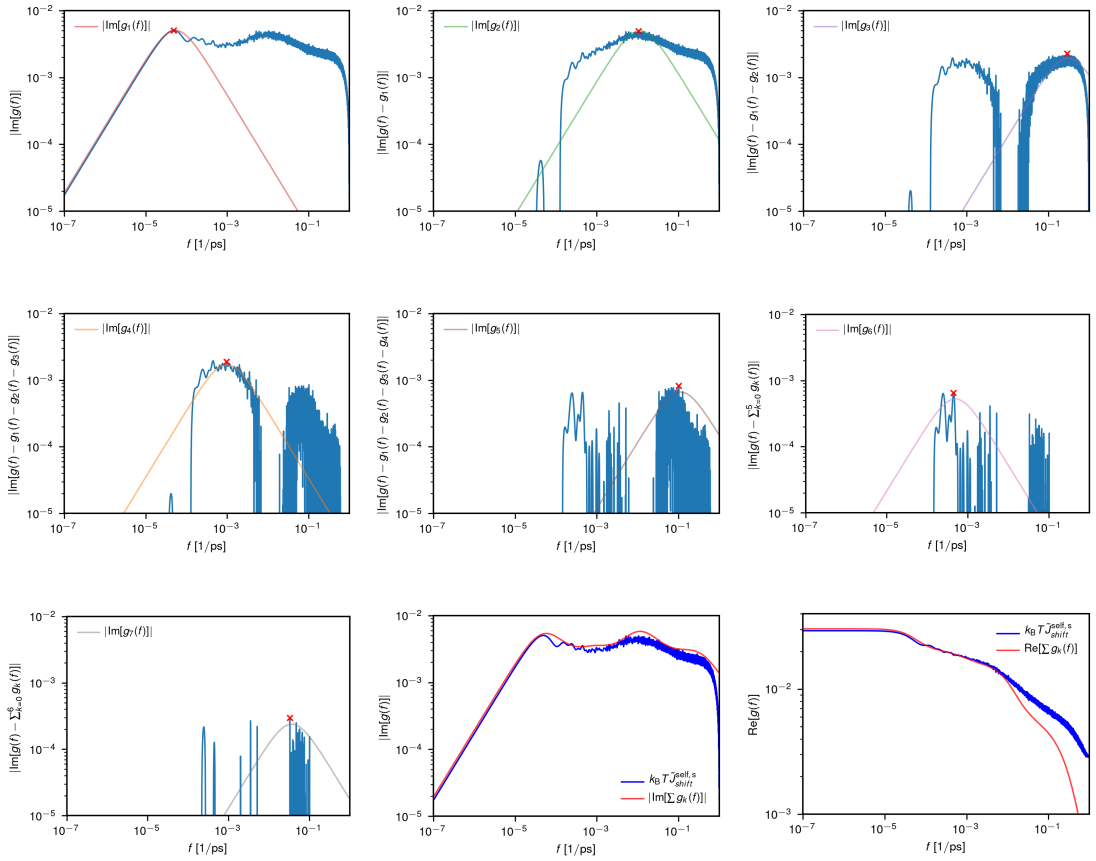

Figure 3.8: This figure provides an example of the fit procedure. Starting from the absolute value of the imaginary part of $k_B T \tilde{J}^{sh,s}_{self}$ (blue line), the global maximum (red point) provides initial values (cf. eqs 3.12 and 3.13) for the fit of a single exponential function according to eq 3.11. Subtracting the obtained single exponential function from the data reveals the next correlation time. Finally, $k_B T \tilde{J}^{sh,s}_{self}$ is compared to the sum of the obtained single exponential functions. The accuracy of the model can be tested by comparison of the real part for data, which in this approach does not contribute to the fit.

from which one can define the remaining factor c_k by

$$c_k = 4\pi f_{k,\max} r_{k,\max} = 2 r_{k,\max} \tau_k^{-1} \quad . \tag{3.13}$$

Due to the linearity of the Fourier transformation, correlation times can be taken from the data if they differ by at least one order of magnitude or more. However, if there are many single exponential functions contributing to the response function and their correlation times are of the same order of magnitude, fits become more difficult to perform due to overlap (cf. Figure 3.7). Considering the stated theoretical approach, the fit procedure is performed as shown as an example in Figure 3.8 for the response $k_B T \tilde{J}^{sh,s}_{self}$.

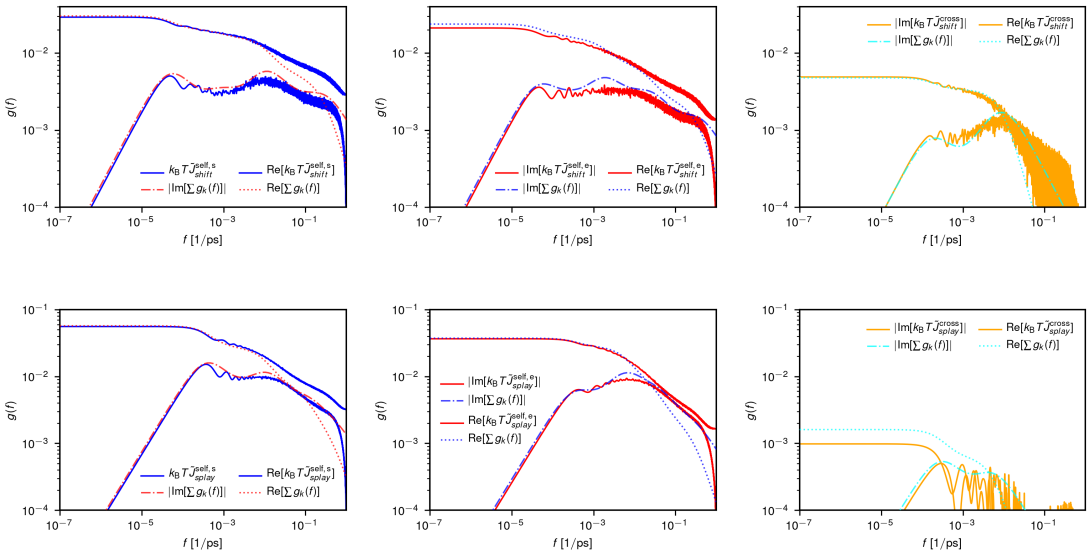

Figure 3.9: Fits of the response functions from Figure 3.5 by a sum of multiple exponential functions (cf. eq 3.8 ff.) for shift (first row) and splay (second row). Fit parameters are shown in Table 3.1.

	$k_\mathrm{B}T\tilde{J}^{\mathrm{sh,s}}_{\mathrm{self}}$	$k_\mathrm{B}T\tilde{J}^{\mathrm{sh,e}}_{\mathrm{self}}$	$k_\mathrm{B}T\tilde{J}^{\mathrm{sh}}_{\mathrm{cross}}$	$k_\mathrm{B}T\tilde{J}^{\mathrm{sp,s}}_{\mathrm{self}}$	$k_\mathrm{B}T\tilde{J}^{\mathrm{sp,e}}_{\mathrm{self}}$	$k_\mathrm{B}T\tilde{J}^{\mathrm{sp}}_{\mathrm{cross}}$
τ_1 [ps]	$2.95 \cdot 10^{3}$	$8.56 \cdot 10^{1}$	$1.79 \cdot 10^{1}$	$3.85 \cdot 10^{2}$	$2.50 \cdot 10^{1}$	$5.42 \cdot 10^{2}$
τ_2 [ps]	$1.39 \cdot 10^{1}$	$3.18 \cdot 10^{3}$	$8.48 \cdot 10^{2}$	$1.44 \cdot 10^{1}$	$4.22 \cdot 10^{2}$	$3.08 \cdot 10^{1}$
τ_3 [ps]	$5.33 \cdot 10^{-1}$	$6.34 \cdot 10^{0}$	–	$1.44 \cdot 10^{0}$	$4.52 \cdot 10^{0}$	–
τ_4 [ps]	$1.63 \cdot 10^{2}$	$1.70 \cdot 10^{1}$	–	$5.12 \cdot 10^{1}$	$6.01 \cdot 10^{-1}$	–
τ_5 [ps]	$1.41 \cdot 10^{0}$	$4.21 \cdot 10^{-1}$	–	$3.45 \cdot 10^{-1}$	–	–
τ_6 [ps]	$3.22 \cdot 10^{2}$	$5.70 \cdot 10^{2}$	–	–	–	–
τ_7 [ps]	$4.32 \cdot 10^{0}$	$7.39 \cdot 10^{-1}$	–	–	–	–
c_1 [nm^2/ps]	$3.42 \cdot 10^{-6}$	$8.96 \cdot 10^{-5}$	$1.87 \cdot 10^{-4}$	$7.81 \cdot 10^{-5}$	$7.64 \cdot 10^{-4}$	$1.84 \cdot 10^{-6}$
c_2 [nm^2/ps]	$7.18 \cdot 10^{-4}$	$2.13 \cdot 10^{-6}$	$1.68 \cdot 10^{-6}$	$1.31 \cdot 10^{-3}$	$2.30 \cdot 10^{-5}$	$1.97 \cdot 10^{-5}$
c_3 [nm^2/ps]	$7.32 \cdot 10^{-3}$	$6.45 \cdot 10^{-4}$	–	$3.84 \cdot 10^{-3}$	$1.47 \cdot 10^{-3}$	–
c_4 [nm^2/ps]	$2.10 \cdot 10^{-5}$	$6.12 \cdot 10^{-5}$	–	$2.69 \cdot 10^{-5}$	$3.02 \cdot 10^{-3}$	–
c_5 [nm^2/ps]	$9.43 \cdot 10^{-4}$	$4.42 \cdot 10^{-3}$	–	$3.90 \cdot 10^{-3}$	–	–
c_6 [nm^2/ps]	$3.28 \cdot 10^{-6}$	$3.31 \cdot 10^{-6}$	–	–	–	–
c_7 [nm^2/ps]	$1.11 \cdot 10^{-4}$	$5.71 \cdot 10^{-4}$	–	–	–	–

Table 3.1: Fit parameters of the Fourier transforms for the padded correlation-function derivatives (cf. Figure 3.5) for shift and splay.

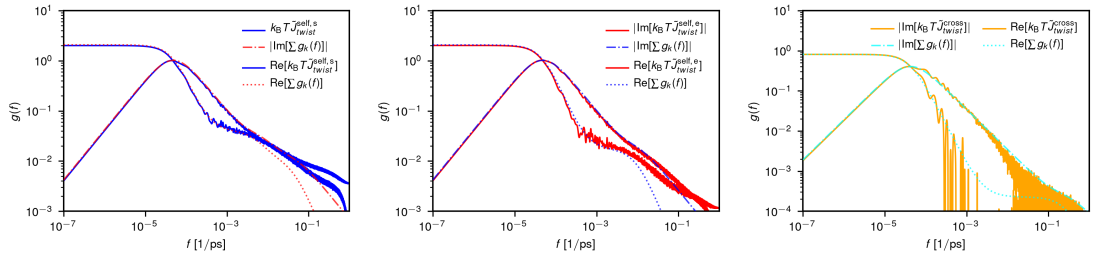

Figure 3.10: Fits of the response functions from Figure 3.5 by a sum of multiple exponential functions (cf. eq 3.8 ff.) for twist. Fit parameters are shown in Table 3.2.

	$k_\mathrm{B}T\tilde{J}^{\mathrm{tw,\,s}}_{\mathrm{self}}$	$k_\mathrm{B}T\tilde{J}^{\mathrm{tw,\,e}}_{\mathrm{self}}$	$k_\mathrm{B}T\tilde{J}^{\mathrm{tw}}_{\mathrm{cross}}$
τ_1 [ps]	$3.26 \cdot 10^{3}$	$3.29 \cdot 10^{3}$	$3.73 \cdot 10^{3}$
τ_2 [ps]	$4.09 \cdot 10^{3}$	$1.70 \cdot 10^{1}$	$6.27 \cdot 10^{-1}$
τ_3 [ps]	$2.81 \cdot 10^{1}$	$1.57 \cdot 10^{3}$	–
τ_4 [ps]	$3.70 \cdot 10^{0}$	–	–
τ_5 [ps]	–	–	–
τ_6 [ps]	–	–	–
τ_7 [ps]	–	–	–
c_1 [nm^2/ps]	$6.12 \cdot 10^{-4}$	$6.15 \cdot 10^{-4}$	$2.17 \cdot 10^{-4}$
c_2 [nm^2/ps]	$1.08 \cdot 10^{-5}$	$1.01 \cdot 10^{-3}$	$3.61 \cdot 10^{-4}$
c_3 [nm^2/ps]	$1.05 \cdot 10^{-3}$	$1.48 \cdot 10^{-5}$	–
c_4 [nm^2/ps]	$2.71 \cdot 10^{-3}$	–	–
c_5 [nm^2/ps]	–	–	–
c_6 [nm^2/ps]	–	–	–
c_7 [nm^2/ps]	–	–	–

Table 3.2: Fit parameters of the Fourier transforms for the padded correlation-function derivatives (cf. Figure 3.5) for twist.

In a first step, the global maximum provides the initial guesses according to eqs 3.12 and 3.13, which we use to fit the first single exponential function. In a second step, the first exponential fit $g_1(f)$ is subtracted from data as $|\mathrm{Im}[g(f) - g_1(f)\ldots]|$ to obtain the next most prominent contribution $g_2(f)$, starting from the global maximum of $|\mathrm{Im}[g(f) - g_1(f)\ldots]|$ for the initial values. The accuracy of the fit can be checked by comparison of the real part of the data and the model function $\mathrm{Re}[g(f)]$ provided by the fit parameters. Results of fits for all response functions from Figure 3.5 are shown in Figures 3.9 and 3.10. We present the obtained fit parameters in Tables 3.1 and 3.2.

We use the fit parameters to calculate the force-transmit functions as explained in eqs 3.5 to 3.7. The results are compared to the transmission functions obtained from the MD simulations data in Figure 3.11. From the real part of the force-transmit function,

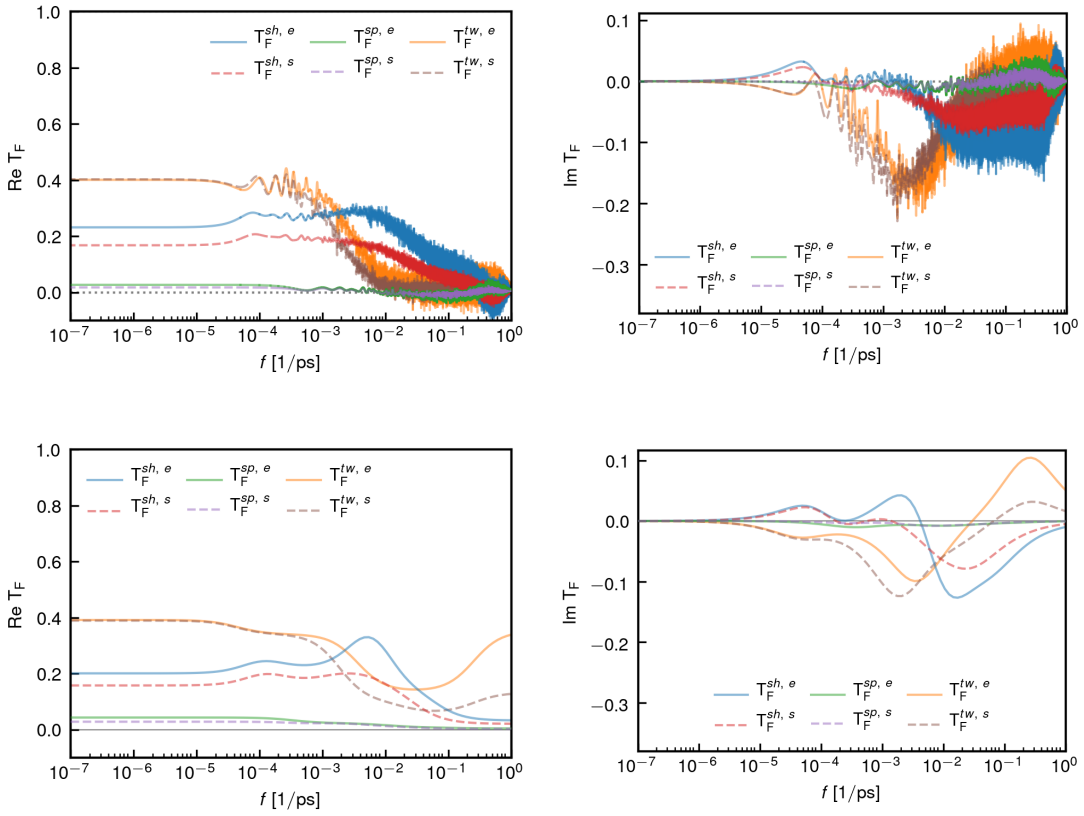

Figure 3.11: Numerical results for the force-transmit functions (cf. eq 3.7) from MD simulations as the ratio of the obtained response functions (cf. Figure 3.5) (upper row) in comparison to the results from obtained fits of the response functions by multi-exponential functions (cf. eq 3.8) (lower row).

we obtain the most efficient signaling mode for coiled coil linker example. The results suggest that for force signals up to a frequency range of $2 \times 10^{-3}\,\mathrm{ps}^{-1}$ or 2 GHz, twist is the most efficient mode for signal transmission. For frequencies higher than 2 GHz, the shift mode becomes more efficient than the twist mode. Throughout the frequency spectrum analysed here, the splay mode is significantly less efficient than the other two modes in its ability of signal transmission through the coiled coil linker. The results for the frequency band above $3 \times 10^{-2}\,\mathrm{ps}^{-1}$ or 30 GHz must be carefully interpreted as the fits of the response functions are less accurate in that spectrum. Both the numerical results from MD simulations and the respective fits of the response functions suggest that for higher frequencies, twist again becomes the most efficient way of signal transmission through the coiled coil linker. The threshold for this transition can be roughly located at $1 \times 10^{-1}\,\mathrm{ps}^{-1}$ or 100 GHz from our results.

3.3 Conclusions

We present MD simulation results of a coiled coil linker, which consists of two α-helices, with focus on the force transmission between two ends of the linker by one of three modes (shift, splay, and twist). Analysis of the three modes shows that the system itself is stable in simulations. Numerical results of the response functions for shift, splay, and twist are translated into Fourier space and consequently used to calculate the transmission function, which gives the transmission coefficient dependency on the frequency of the driving force. These response functions are fitted by a multi-exponential model consisting of a sum of up to seven single exponential functions. The fit parameters allow for analytic expressions for the force-transmit functions, which help to pinpoint transitions between the most efficient modes for signal transmission through the coiled coil linker. Comparison of the numerical results from MD simulations and the analytic expressions for the force-transmit functions reveal the dominant part of the twist mode as the most efficient way of signaling over almost the entire frequency spectrum between 100 kHz and 1 THz. In the intermediate regime from 2 GHz to roughly 30 GHz, the shift mode becomes more efficient for signal transmission than the twist mode. The upper bound of this intermediate regime can only be interpreted as a crude estimate as the fit functions for the response functions are less accurate in that frequency regime. However, the qualitative result is consistent between the numerical results from MD simulations and the results from the fitted analytic expressions, namely the twist mode overcomes the shift modes efficiency again for higher frequencies. Therefore, only the exact threshold must be carefully interpreted. With this analysis, we have given a road map on how to distinguish different translational and rotational modes in their ability to transmit signals throughout a double-helical linker depending on the frequency with which these modes are driven. We have shown that some modes will be more likely to be present at given parts of the frequency spectrum.

3.4 Methods

We start with the PDB structure for the blue-light photoreceptor 4GCZ[169] available from the protein data bank.[170] The suspected coiled coil motive[72] is located between the residues 126 and 148, which appears two times in the protein due to its dimeric structure. For the extraction of the two coils into a new pdb-file, we consider one more residue on each end so we can do the acetylation and amidation. Each coil is capped using the gromacs[171,172] tool pdb2gmx with the force-field CHARMM27.[173,174] The N-terminus of the helices at the side of ILE$-$126 is NH_2 and the C-terminus at ARG$-$148 is an N-Methylamide C-terminus (CT_3), which is given by CO$-$NH$-CH_3$. Both termini have a neutral net charge. One α-helix consists of 23 residues comprised of 387 atoms. The combined mass of the two coils is 5486.117 u or $9.109\,91 \times 10^{-24}$ kg. The sequence of each coil is ITEHQQTQARLQELQSELVHVSR. Charged residues of the sequence are GLU ($-e$) and ARG ($+e$), resulting in a total net charge of $-e$ per α-helix. The

system of the two coils is put into the center of a dodecahedron box with the box vector lengths 6.35 nm, box angles 60°, 60° and 90° which yields a box volume of 181.07 nm^3 using the gromacs[171,172] tool editconf. The system is subsequently relaxed by a steepest descent with 20000 steps, a maximum force parameter (emtol) of 1 $kJ\,mol^{-1}\,nm^{-1}$, an initial step size (emstep) of 0.01 nm, Particle-Mesh Ewald electrostatics, the Verlet cutoff scheme and no constraints. The system is solvated by adding 5646 water molecules using the gromacs[171,172] tool solvate with the employed water force-field TIP3P,[175] which yields a density of 986.686 g/L. To account for the negative charge of the coils in the system, two water molecules of the system are replaced by sodium ions, leading to a zero total net charge. The system is subsequently relaxed again by the same steepest descent settings as before. The simulation of the coiled coil system is run over the course of 10 μs with a time step of 2 fs. Positions of all atoms are written to a trajectory file after every 10 ps. The center of mass translational velocity is removed (comm-mode = linear). The Verlet cutoff scheme is used. The neighbor list is updated every 10 steps. The neighbor search type is set to grid. Fast smooth Particle-Mesh Ewald (SPME) electrostatics are employed with a coulomb cutoff of 1 nm. For temperature coupling, the velocity rescaling method[176] is used with a reference temperature of 300 K and a coupling time constant of 0.1 ps. Protein, solvent, and ions are set to be three separate temperature-coupling groups. We use Parrinello-Rahman pressure coupling which is isotropic.[177] The pressure coupling time constant is set to 0.5 ps, the reference pressure for coupling to 1 bar and the compressibility to $4.5 \times 10^{-5}\,bar^{-1}$.

For fast Fourier transforms for calculations of correlations the python wrapper pyFFTW is used to employ FFTW3, a comprehensive C library for computing discrete Fourier transforms.[178–183]

Chapter 4

Opposing Temperature Dependence of the Stretching Response of Single PEG and PNiPAM Polymers

Bibliographic information: This chapter and appendix B have previously been published. Reprinted with permission from Ref. [iii], https://doi.org/10.1021/jacs.9b04383.

Author contribution statement: Richard Schwarzl carried out all simulations and the analysis of the data. The presentation of this data by Roland R. Netz at the group of Torsten Hugel encouraged the experimental investigation of the temperature dependence of the force-extension relation for PEG and PNiPAM by Adrianna Kolberg under the supervision of Bizan N. Balzer. At the start of the experimental investigation, Richard Schwarzl provided a written-down overview of simulation results, analysis of these data and figures. In preparation of the publication, Richard Schwarzl provided his manuscript for the temperature dependence of the force-extension relation of PEG to Bizan N. Balzer. Bizan N. Balzer wrote the first version of the manuscript except the methods part for the simulations, which has been written by Richard Schwarzl. Bizan N. Balzer created all figures except figures 4.5 a and 4.5 b and the simulation snapshots of the molecular dynamic simulations in figure 4.1, which have been created by Richard Schwarzl. The table B.1 in appendix B has been created and provided for publication by Richard Schwarzl. All authors contributed to the final version of the manuscript, which is published under: A. Kolberg, C. Wenzel, K. Hackenstrass, R. Schwarzl, C. Rüttiger, T. Hugel, M. Gallei, R. R. Netz, and B. N. Balzer, Opposing Temperature Dependence of the Stretching Response of Single PEG and PNiPAM Polymers, Journal of the American Chemical Society 141, 11603 (2019).

4.1 Introduction

Polymer coatings, blends, and composites are common in every household and became a part of our everyday life in the past century. They are fundamental for industrial applications due to their unique molding ability, their robustness, and their light weight.[184–186] Even though we benefit from all their advantages on a daily basis, their behavior is still not completely understood. In particular, their response to external stimuli like force or temperature change is often only understood at a phenomenological level.

The temperature response of polymers is important for both technical applications and the fundamental understanding of polymer physics.[187–191] Depending on the technical application, polymer properties have to be maintained over a large temperature range (e.g., in cars), or coil to globule transitions are used to obtain stimuli-responsive materials (e.g., for triggered drug release).[192–194] In polymer physics, temperature is a fundamental parameter. Therefore, the dependence of polymer properties on temperature is a crucial part of the understanding of polymer mechanics.

Atomic force microscopy (AFM) based single molecule force spectroscopy (SMFS) is a versatile tool for investigating temperature-dependent single polymer mechanics in a liquid environment, in particular when combined with molecular dynamics (MD) simulations.[48,195–201] Here we focus on two widely used water-soluble polymers with different temperature response, namely, polyethylene glycol (PEG) and poly(Nisopropylacrylamide) (PNiPAM).

In bulk experiments PNiPAM in water undergoes a transition from a coil to a globular conformation at its lower critical solution temperature (LCST) of around 305 K.[202,203] This LCST is close to the temperature at which most physiological processes occur, which makes PNiPAM promising for the development of controlled drug delivery systems.[204–207] The coil conformation of PNiPAM below the LCST is thought to be stabilized via formation of hydrogen bond bridges between water molecules and the amide side groups.[208] The water molecules align around the hydrophobic backbone, making the polymer soluble in water and leading to energetic stabilization. At temperatures above the LCST, the entropy of the polymer-water system dominates, which is unfavorable for the exothermic formation of hydrogen bonds. Thus, the bound water molecules are released to increase their entropy and the polymers collapse into a globular state.[209] It still remains unclear whether this is a bulk effect or would also be observed for a single polymer chain. The single molecule stretching response at different temperatures has been measured by AFM but with controversial results. Kutnyanszky et al. have found a linear temperature response without any sign of a sharp transition or minimum around the LCST.[210] Cui et al. have claimed that the stretching force has a minimum at the LCST.[199] Liang et al. have found a transition of the force-extension profile from wormlike chain behavior to a Rayleigh- Plateau of constant force at the LCST.[200] Furthermore, Zhang et al. have investigated the solvent-dependent single molecule stretching response of PNiPAM, observing thermally induced multisite adsorption above its LCST.[201] The first study was restricted to a small temperature

range of 299 K to 313 K, while the other three studies used the nanofishing method for their AFM-based experiments. There, a polymer physisorbed on a surface, e.g., glass or Au(111), is randomly picked up with a cantilever tip. This leads to several problems, namely, that interactions between different polymer chains physisorbed on the substrate cannot be excluded (bulk effects) and that every time a different polymer might be picked. These issues, as discussed later, led us to revisit PNiPAM's temperature behavior.
PEG is a linear macromolecule consisting of $-(CH_2-CH_2-O)-$ repeating units. It is used for medical and technological purposes.[211–214] Unlike most polymers, PEG is generally soluble in water even for a high degree of polymerization.[215] PEG does not exhibit a LCST transition and could be expected to behave like an ideal entropic elastic spring. This has indeed been confirmed in hexadecane, where the force-extension relation of PEG is in accordance with the freely jointed chain model (FJC).[216,217] However, in water the situation changes and PEG no longer shows the characteristics of an ideal entropic spring at high stretching forces.[48,216] The reason is found in the structural change from gauche to trans.[217] The ratio of monomers in the trans and gauche conformation during stretching and the number of water bridges was extracted from water-explicit MD simulations. Altogether, a dominant solvent related effect of energy over entropy was suggested at high stretching forces.[48] Again temperature-dependent SMFS experiments should be able to clarify these points.
Here we compare the force response of PEG and PNiPAM at various temperatures in a combined experimental and theoretical study. This allows us to delineate the molecular details of the different temperature responses of PEG and PNiPAM. While PEG becomes softer at higher temperatures, PNiPAM stiffens with increasing temperature. These seemingly contradictory results can be explained in molecular detail with our combined approach. We anticipate that this will help to guide the development of tailored polymeric materials that have to function over a wide force and temperature range.

4.2 Methods

Chemicals. The chemicals used for cleaning of glassware were ammonia solution (Roth, Karlsruhe, Germany, $28.0-30.0\%$), hydrogen peroxide solution (Sigma-Aldrich, St. Louis, MO, USA, $\geq 30\%$), and ultrapure water (Purelab Chorus 1, Elga LabWater, Celle, Germany, 18.2 MΩ cm) for preparing RCA solution with a ratio of 1:1:5. For the functionalization process toluene(Fisher Chemicals, Hampton, NH, USA, 99.99%), ethanol (Roth, Karlsruhe, Germany, $\geq 99.9\%$), HEPES buffer (Pan-Reac AppliChem, Darmstadt, Germany, 99.5%, 10 mM, pH = 7, 50 mM NaCl), silane-PEG-mal (NANOCS, Boston, MA, USA, $M_w = 5$ kDa, $l_{cont} = 41$ nm), and HEPES buffer (10 mM HEPES, NaCl 50 mM, pH 7) were used. For the synthesis of PNiPAM all solvents and reagents were purchased from Alfa Aesar (Haverhill, MA, USA), Sigma-Aldrich (St. Louis, MO, USA), Fisher Scientific (Hampton, NH, USA), ABCR (Karlsruhe, Germany) and used

as received unless otherwise stated. Deuterated solvents were purchased from Sigma-Aldrich. *N*-Isopropylacrylamide (NiPAM) was recrystallized out of toluene and *n*-hexane (1:1) and dried in vacuum. $Cu^{(I)}Br$ was washed five times with glacial acetic acid and ethanol. Tris[2-(dimethylamino)ethyl]amine (Me_6TREN), *N*, *N*-dimethylformamide (DMF), 2 bromoisobutyric *tert*-butyl ester (*t*BbiB) were stored under argon atmosphere.

Polymers. The polymer used for the PEG experiments was purchased as thiol-PEG-thiol (HS-PEG-SH, Creative PEGWorks, NC, USA, $M_w = 35\,kDa$). The expected mean contour length for the experiments was calculated to 282 nm with a monomer length of 0.356 nm and a molecular weight of 44.05 Da.[48,217] Adding the silane-PEG-mal linker length with about 41 nm leads to a total length of 323 nm.

PNiPAM was synthesized as follows. The corresponding reaction path can be found in Figure B.1a: 9.00 g (79.53 mmol) of NiPAM and 3.20 µL (0.018 mmol) of *t*BbiB were placed in a Schlenk tube, and an amount of 18 mL of a 50:50 mixture of ultrapure water and DMF was added. The mixture was degassed twice, and the polymerization was started by adding 90 µL (0.018 mmol) of a 0.2 M solution of $Cu^{I}(Me_6TREN)Br$ in DMF. After 40 min an amount of 12 mg (0.075 mmol) of potassium ethyl xanthogenate was added. After 10 min the reaction was cooled in an ice bath for 30 min. The mixture was diluted with 160 mL of THF and filtered through an aluminum column to remove the residual copper catalyst. The polymer was precipitated in 800 mL diethyl ether and dried in vacuum (yield, 4.06 g; $M_n = 497\,kDa$; $Đ = 1.28$).

An amount of 500 mg (0.001 mmol) of the CTA-end-capped PNiPAM was dissolved in 20 mL of ultrapure water, and an amount of 100 mg (2.64 mmol) of $NaBH_4$ was added. After 2 h the polymer/solvent mixture was dialyzed against water for 4 days. The polymer was obtained by lyophilization (452 mg). An amount of 300 mg of the polymer was dissolved in 10 mL of DMF, and an amount of 45 mg (0.16 mmol) of tris(2-carboxyethyl)phosphine hydrochloride (TCEP) was added. After 24 h the mixture was diluted with water and dialyzed against water for 4 days again. An amount of 243 mg of the resulting polymer was obtained after lyophilization ($M_n = 510\,kDa$, $Đ = 1.28$; see Figure B.1b).

For PNiPAM, the monomer length was calculated with respect to the backbone using a C – C bond length of 154 pm and a bond angle of 109.5°.[218] With a calculated monomer length of around 252 pm and a monomer weight of 113 Da, the average contour length could be calculated to 1.14 µm with 4513 repeating units. Adding the silane-PEG-mal linker length with about 41 nm leads to a total length of 1.18 µm.

Polymer Characterization. Standard size-exclusion chromatography (SEC) was performed with a system composed of a 1260 IsoPump G1310B (Agilent Technologies, Santa Clara, CA, USA), a 1260 VW detector G1314F at 254 nm (Agilent Technologies), and a 1260 RI detector G1362A at 35 °C (Agilent Technologies), DMF (with LiCl, 1 g/L) as the mobile phase (flow rate 1 mL/min) on a GRAM column set for DMF (at 50 °C) from PSS (Polymer Standard Service (PSS), Mainz, Germany) (GRAM 30, GRAM 1000, GRAM 1000). Calibration was carried out using PMMA standards for DMF (from PSS). Samples were measured with concentrations between 1 and 3 mg/mL. For

data acquisition and evaluation of the measurements, PSS WinGPC UniChrom 8.2 was used.
NMR spectra were recorded on a Bruker DRX 500 spectrometer (Billerica, MA, USA) working at 500 MHz. NMR chemical shifts were referenced relative to the used solvent (D_2O). For data acquisition and evaluation of the measurements, NMR software MestReNova 11.0 was used.
Simulation Details. All molecular dynamics simulations are performed with the GROMACS simulation package (version 4.6.5 or newer).[219] The time step is set to 2 fs. The temperature is set to a fixed value for each individual simulation. For temperature and pressure coupling, the v-rescale and Parinello-Rahman algorithms are used.[220,221] The pressure is isotropic and set to 1 bar with a water compressibility of $4.5 \times 10^{-5}\,\mathrm{bar}^{-1}$. All simulations are performed with periodic boundary conditions in all three directions. The cutoff of nonbonded interactions is set to 1.0 nm. The particle mesh Ewald method is used for the long-range electrostatic interactions.[222] For PEG the force field charmm35r is used.[223] The elongated ($H-[CH_2-O-CH_2]_{12}-H$) chain is placed in a $3\,\mathrm{nm} \times 3\,\mathrm{nm} \times 9.6\,\mathrm{nm}$ box with 2900 tip3p water molecules. To equilibrate the system, the initial energy minimization of the system is followed by a 10 ps NVT simulation with constant volume and without pressure coupling and a 2 ns NPT simulation with an isotropic pressure of 1 bar. For the production run, the first and the last oxygen atoms are defined as pulling groups. A constant force between 1 pN and 600 pN is applied in the z direction. For low forces, we additionally performed simulations using a longer chain ($H-[CH_2-O-CH_2]_{24}-H$) placed in a $4.5\,\mathrm{nm} \times 4.5\,\mathrm{nm} \times 20\,\mathrm{nm}$ box with 13433 water molecules. Each pulling simulation is performed for at least 200 ns. The temperature remains unchanged throughout a single simulation run and is set to 250, 300, 325, 350, and 400 K, respectively.
For simulations of PNiPAM, parameters remain the same as for PEG if not stated otherwise. For PNiPAM we use a recently modified version of the OPLS-AA force field with partial charges optimized by comparison to quantum mechanical simulations together with the SPC/E water model.[224–227] The first and the last C atom of the backbone of $H-[C_6H_{11}NO]_{20}-H$, which are adjacent to the side chain of the polymer, are defined as pulling groups. A constant force between 1 pN and 500 pN is applied in the z direction. We simulate isotactic (meso-diad) PNiPAM, where the side chains are located on one side of the backbone, and syndiotactic (racemo-diad) PNiPAM, where the side chains are on alternating sides of the chain. The elongated chain is placed in a $3\,\mathrm{nm} \times 3\,\mathrm{nm} \times 11\,\mathrm{nm}$ box with 3121 SPC/E water molecules. Each pulling simulation is performed for at least 1000 ns. The temperature remains unchanged throughout a single simulation run and is set to 288, 298, 308, and 318 K, respectively.
For both PNiPAM and PEG, the extension in the pull direction is calculated as the time average of the separation in the z direction of the two pulling groups over the course of a simulation. The extension of PEG is normalized by the contour length $L_{C,0} = 11 \times 0.356\,\mathrm{nm}$ or $L_{C,0} = 23 \times 0.356\,\mathrm{nm}$, depending on the polymer length and in accordance to Liese et al.[48] For isotactic PNiPAM the contour length used for normalization is $L_{C,0} = 19 \times 0.266\,\mathrm{nm}$ and for syndiotactic PNiPAM $L_{C,0} = 19 \times 0.264\,\mathrm{nm}$

in accordance to Kanduč et al.[226]

AFM Cantilever Tip Functionalization. The covalent attachment of one single polymer to a cantilever tip is decisive for single molecule force experiments. It enables a high reproducibility when performing force spectroscopy with a certain polymer on a specific cantilever tip. Influences on the measurements like differences in the contour length due to different attachment points to the cantilever tip, variation of the spring constant of the cantilever, or interactions with further polymers can be widely prevented.[228] Furthermore, a high yield of single molecule events can be obtained (19% for PEG and 42% for PNiPAM).

Silicon nitride AFM cantilevers, namely, MLCT and MLCT-BIODC (both: Bruker AFM probes, Camarillo, CA, USA) were used for all measurements. First, the cantilevers were activated with oxygen plasma to gain hydroxyl groups on the surface of the cantilever tips. While the MLCT probes were treated for 1 min with 20% power, the thermally more stable MLCT-BIO-DC probes were treated for 2 min with 40% power, both at a pressure of 0.1 mbar. As a next step, a 5 kDa silane-PEG-mal (NANOCS, Boston, MA, USA) linker was bound to the cantilever tip. The linker enabled us to couple a probe molecule to the cantilever tip via a covalent bond. Therefore, the cantilevers were incubated in a solution of silane-PEG-mal in toluene (1.25 mg/mL, 3 h, 60 °C).[229] Even though the cantilever tip is covered with maleimide groups, these undergo a hydrolysis in water (inactive PEGs) leaving just few binding sites for the single probe polymer to be attached.[230] The inactive PEGs serve as a passivation layer to reduce undesirable interaction between the cantilever tip and an underlying surface as well as between the single PEG polymer and the cantilever tip. For functionalization with PEG, the PEGylated cantilevers were rinsed in toluene and incubated in a solution of SH-PEG-SH in toluene (1.25 µg/mL, 1 h, 60 °C). For functionalization with PNiPAM, the PEGylated cantilevers were rinsed in toluene and ethanol before incubation in a solution of PNiPAM-SH in ethanol (1.25 µg/mL, 3 h, room temperature). After a final rinsing, the cantilevers were stored in HEPES buffer at 4 °C until use in the AFM experiment.

For every functionalization, control cantilevers were additionally prepared by the same procedure incubating the cantilevers in the pure solvent instead of the SH-PEG-SH or the PNiPAM-SH solution. A scheme of an AFM-based single molecule force spectroscopy setup can be found in Figure 4.1.

AFM Measurements. All measurements were performed with a Cypher ES (Asylum Research, an Oxford Instruments company, Santa Barbara, CA, USA) using a heating and cooling sample stage for temperature variation. All measurements took place in ultrapure water on a silicon oxide wafer cleaned in ethanol using a sonicator (Elmasonic S15, Elma, Singen, Germany). Before every measurement, the inverse optical lever sensitivity (InvOLS) was determined by fitting a linear function to the repulsive regime of a force-extension curve. In order to reduce errors, the determination of the InvOLS was performed by using an average of at least five individual InvOLS values. The spring constant of the cantilever was determined by the thermal noise method.[231] The measurement parameters were defined as follows: force distance, $1-3\,\mu$m; velocity, $1\,\mu$m/s;

trigger point, 500 pN; sampling rate, 5 kHz; dwell time toward the surface, $0 - 1$ s. To minimize the influence of the probe, force-extension curves were recorded in a gridlike manner with 10×10 points covering $20 \times 20\,\mu$m (force maps). At least two force maps were obtained per cantilever, with and without dwell. The temperature was varied in a random order. Following a temperature change, force-extension curves were collected after a stabilization time of at least 5 min. Prior to a series of measurements, at least one control cantilever was measured on different spots to ensure the cleanliness of the SiO_x surface and a contamination-free functionalization. Once the control cantilevers showed an absence of stretching events, the PEG or PNiPAM functionalized cantilevers

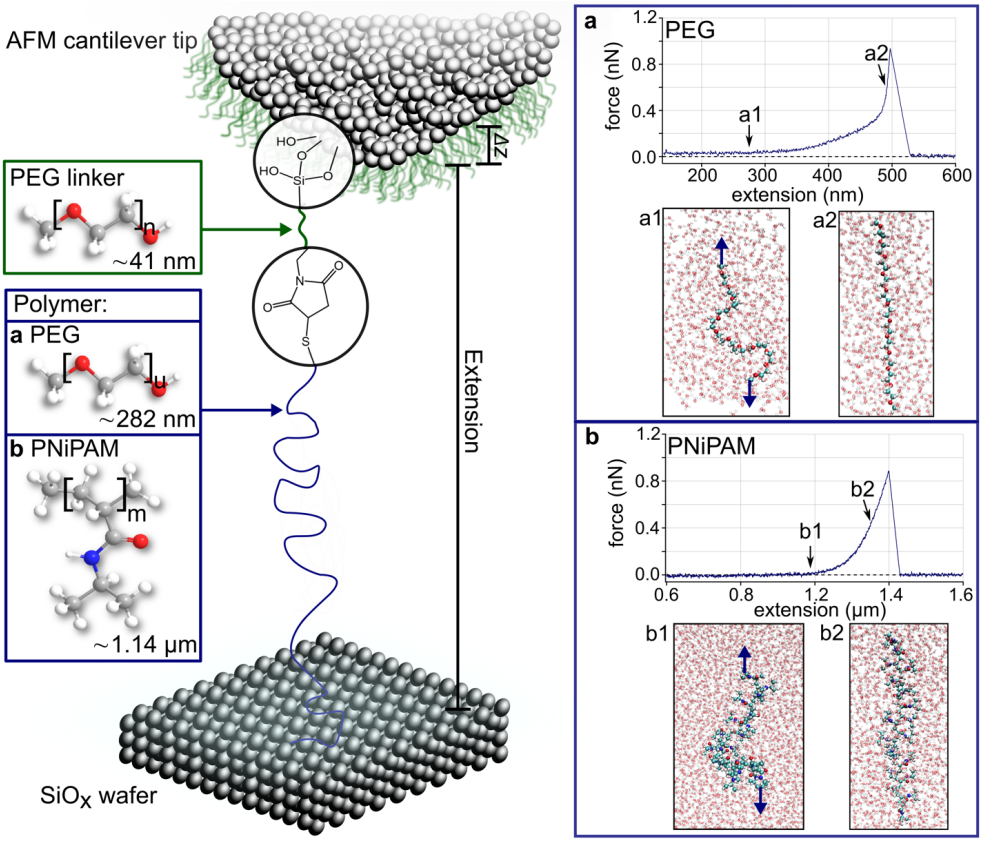

Figure 4.1: Scheme of an AFM single molecule setup with a zoom-in to the functional groups (circular frames) and an exemplary monomeric unit for the PEG linker (green box) and the polymer (blue box) at room temperature. On the right examples of force-extension curves at 298 K are shown for (a) PEG and (b) PNiPAM including snapshots of the MD simulations at the forces indicated in the force-extension traces. These forces are 15 pN and 600 pN for PEG (a1, a2) and 20 pN and 500 pN for isotactic PNiPAM (b1, b2). The expected monomer numbers in the experiments are $n = 114$ (41 nm) for the PEG linker, $u = 795$ (282 nm) for the PEG, and $m = 4513$ (1.14 µm) for the PNiPAM polymer. Δz indicates a possible vertical shift corresponding to the anchoring position of the polymer on the cantilever tip.

were measured, respectively.
For data evaluation, a self-programmed evaluation software based on Igor Pro (Wavemetrics, Portland, OR, USA) was used. The force- extension curves were corrected for drift by fitting a linear function to the baseline after the last stretch. Then, the linear function was subtracted from the force-extension curve leading to curves such as shown in Figure 4.1a and Figure 4.1b.
Even though we used PNiPAM polymers with a low polydispersity index value $Đ = 1.28$, significant differences in the polymer lengths were observed in the AFM experiments. This observation can be explained by different phenomena, which have already been described in literature before.[48] The common method to detect the molecular weight and the polydispersity is size-exclusion chromatography (SEC), which determines a relative weight of the polymer compared to standards like polystyrene or poly(methyl methacrylate).[232] As polymers can significantly differ with respect to their hydrodynamic volume compared to these standards, a deviation of the determined molecular weight of PNIPAM from the absolute molecular weight is expected. Another important influence is given by the silan layer. During the functionalization process in toluene spurious water might start an oligomerization of the silane molecules prior to the attachment to the cantilever tip. This leads to a flexible silane network with fewer anchor points.[233] Furthermore, the anchoringpoint of the polymer to the cantilever tip might not necessarily be at the apex.[48] As the cantilever detects only a force component in vertical direction, a nonvertical orientation of the polymer between a pinpoint on the substrate and the cantilever tip might lead to a shift of the detected force according to Serr et al.[234] Yet for long polymers such as the PEG and PNiPAM polymers presented here, the deviation from a vertical orientation is expected to be less than 1°, leading to a force variation below the detection limit of the AFM.[235] For PEG, a broad mass distribution is expected (PDI is not indicated by the manufacturer). Furthermore, for HS-PEG-SH it is chemically possible that the ends of two polymers oxidize and react with each other to give a disulfide bridge.[236] That might lead to length values that are multiples of the contour length. Even though these phenomena have an influence on the observed absolute contour length of the polymer, they do not affect the stretching response of the respective polymer itself. Therefore, all these effects are not expected to show any dependence on temperature and should not affect the general results found here.

4.3 Results and Discussion

Figure 4.1 shows a schematic of the AFM-based single molecule force experiments including example traces and simulation snapshots. A single stretching event at a contour length of about 350 nm such as given in Figure 4.1a was observed in the PEG data in 95 of the 500 measured force-extension curves (fraction of 19%). For PNiPAM, 252 out of 600 force- extension curves (42%) were found, such as shown in Figure 4.1b. In order to discuss the temperature dependence of the force-extension traces, a single

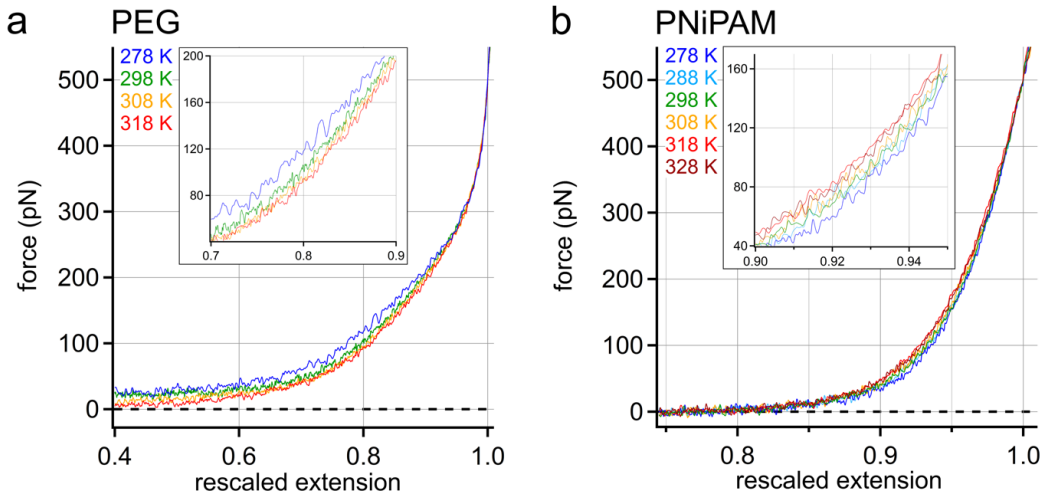

Figure 4.2: Experimental AFM data: (a) master curves of PEG showing a decreasing stretching force with increasing temperature; (b) master curves of PNiPAM showing an opposite temperature dependence compared to PEG. A single master curve for every temperature was determined based on force-extension curves comprising a stretching event to at least 500 pN. After rescaling of the extensions to the length L_0 at a force of 500 pN, the force-extension curves were averaged by a binomial smoothing.

master curve for every temperature was determined using only those curves that show a stretching event to at least 500 pN (see Figures B.2 and B.5). Then, the extensions were rescaled to a length L_0 at a force of 500 pN where conformational fluctuations and solvent effects are negligible.[237] Finally, the force-extension curves were averaged by a binomial smoothing, where a Gaussian filter convolves the data with normalized coefficients derived from Pascals triangle at a level equal to the smoothing parameter 20.[238] These rescaled traces are shown in Figure 4.2.

For the PEG master curves depicted in Figure 4.2a we used 19 traces (4%) in total that reached forces of at least 500 pN in order to investigate the polymer behavior at intermediate and high stretching forces. We focus on the extension range from 0.4 to 1.0 L_0 because the temperature effect is best identified here. Furthermore, we can be sure that this extension range only comprises the stretching of a single molecule (for raw data see Figure 4.2). The difference between the force-extension curves for PEG measured at different temperatures (Figure 4.2a and Figure B.3) can be described as a decrease of the force with increasing temperature at a given rescaled extension, which is discussed in detail below. In other words, an increase of approximately 5% of rescaled extension (at an applied force of 100 pN) is observed when increasing the temperature from 278 K to 318 K. Note that it is crucial to compare the temperature dependence for data taken with one and the same cantilever and for one identical set of polymers. Otherwise, variations of the spring constant of different cantilevers and possibly the contour length of polymers could mask the temperature effects (see Methods section for details). A

second data set confirms the observed temperature response (Figure B.4).
For PNiPAM, the contour length varies significantly even for a single cantilever tip. In order to minimize the effects of contour length, we selected only traces with contour lengths between 1.0 µm and 2.5 µm and detachment forces of more than 500 pN. This resulted in 20 traces (3%), which are shown in the master curves depicted in Figure 4.2b. The raw data can be found in Figure B.5. Additionally, Figure B.6 shows all master curves for different temperatures. Again, a temperaturedependent shift in the stretching force can be observed but this time in the opposite direction compared to PEG. The stretching forces increase with increasing temperature, i.e., the chain becomes stiffer, for a given rescaled extension (see Figures B.6 and B.7). In other words, an decrease of approximately 1% of rescaled extension (at an applied force of 100 pN) is observed when increasing the temperature from 278 K to 328 K. It is noteworthy that there is no sudden change in the shape or frequency of the recorded force-extension curves when comparing temperatures below and above the LCST. This agrees with the expectation that a highly stretched single molecule does not show cooperative effects, which would rather be expected for weakly stretched chains that can self-interact.

This is in contrast to the study by Cui et al., which claimed that the stretching force has a minimum at the LCST when examining the temperature range of 304 K to 313 K with a difference of relative extension of up to 10% at 200 pN.[199] Furthermore, we did not observe any plateaus in our force- extension curves over the whole range of temperature values from 278 K to 328 K such as observed by Liang et al.[200] Yet both Cui et al. and Liang et al. performed nanofishing experiments. Zhang et al. have already pointed out that cantilever tip functionalization might be a better way to obtain clean and real single molecule stretching events.[201] Nanofishing might lead to cooperative effects that strongly affect the outcome of a single molecule study due to additional substrate-adsorbed molecules.[239] The covalent attachment of a single molecule to the cantilever tip as presented here enables us to exclude any interactions with neighboring polymers. Therefore, our results are consistent with the study by Kutnyanszky et al.,[210] in which single molecule attachment to a cantilever tip had also been carried out. Yet our significantly larger force and temperature ranges allow us to deduce the molecular mechanism for this behavior. A second data set for PNiPAM taken with a different cantilever confirms the observed temperature dependence (Figure B.7). To deepen our understanding of these observations, MD simulations were performed and compared to the experimental data.
Figure 4.3a shows a comparison between the experimental master curves and the MD simulations for PEG. The distinct tripartite structure with a middle section exhibiting an almost constant force-extension slope is well reproduced by the simulations. Also, the temperature shift agrees well with the experimental data. This validation enables us to extract the molecular mechanisms for PEG from the MD simulations (see below). Figure 4.3b and Figure 4.3c show the comparison of the experimental master curves for PNiPAM with two sets of MD simulations. As the polymer was synthesized by a controlled radical polymerization without any manipulation of the propagating chain ends, a predominantly atactic arrangement of the side groups is expected. This is confirmed

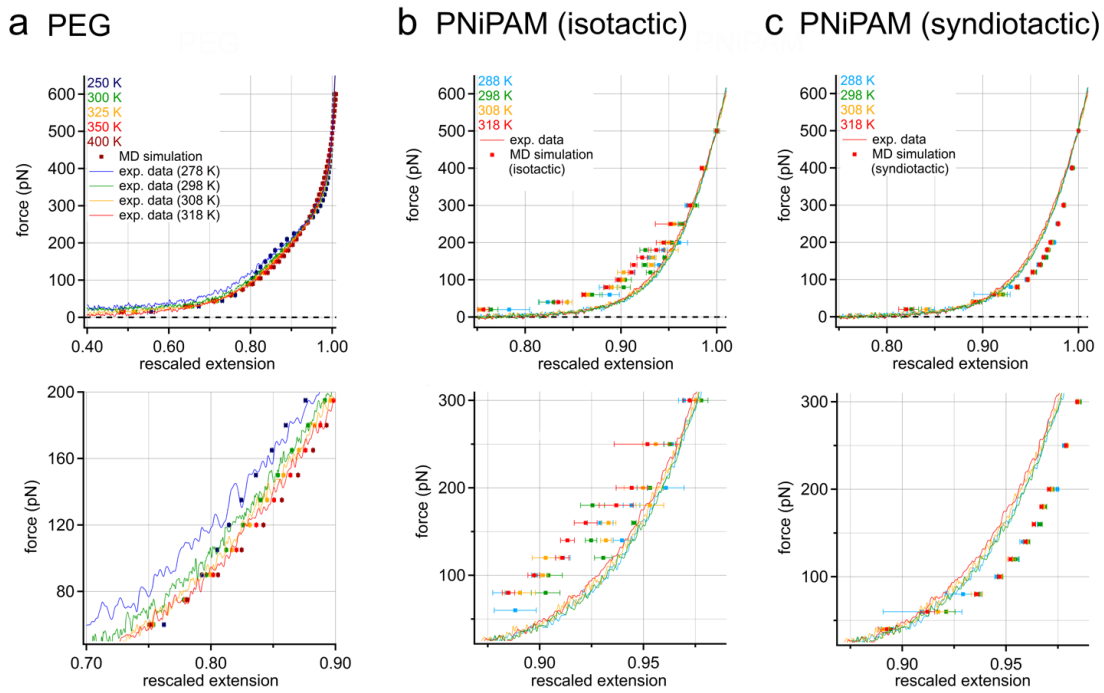

Figure 4.3: Comparison of MD simulations (circles) with the experimental data (lines): (a) MD simulations for a PEG molecule for a wide temperature range showing the same characteristics as the experimental data. Note the significantly larger temperature range in the simulations. (b) MD simulations of an isotactic and (c) of a syndiotactic PNiPAM polymer compared to the experimental data for atactic PNiPAM, respectively. The experimental force-extension traces are situated between the MD simulations of the syndiotactic and isotactic PNiPAM. Also, the magnitude of the temperature-induced force shift is between the two extreme cases considered in the MD simulations. Respective zoom-ins are shown in the bottom row for better comparison of the relevant mid-force range.

by the ^{13}C-NMR data, which show the expected ratios between the signals in the range of 30 ppm to 45 ppm (Figure B.1c).[240] Accordingly, the experimental force-extension curves are situated between force-extension curves from MD simulations representing the extreme cases of a fully isotactic and a fully syndiotactic polymer, as shown in Figure 4.3b (isotactic) and Figure 4.3c (syndiotactic). For the isotactic simulations, an extremely slow relaxation of the PNiPAM chain leads to a strong variation of the stretching force, masking any clear trend with respect to temperature. By contrast, the syndiotactic simulations exhibit small error values and present a clear force-extension course for the different temperatures. In particular, the temperature shift in the force response shows the same qualitative behavior for both AFM experiment and MD simulation, although differing quantitatively. The quantitative difference presumably results from the difference between atactic (experiment) and syndiotactic (MD simulation) arrangements.

The temperature dependence of the free energy per length F/L_0 can generally be ap-

proximated as T^n with an exponent n . An ideal entropic behavior is predicted by the FJC model,[241]

$$\frac{z_{\mathrm{ete}}}{L_c} = \coth \frac{f\,b}{k_B T} - \frac{k_B T}{f\,b} \tag{4.1}$$

while the wormlike chain (WLC) model is not purely entropic,[242]

$$f = \frac{k_B T}{l_p}\left[\frac{z_{\mathrm{ete}}}{L_c} + \frac{1}{4\left(1-\frac{z_{\mathrm{ete}}}{L_c}\right)^2} - \frac{1}{4}\right] \tag{4.2}$$

Here z_{ete} is the rescaled end-to-end distance, L_c the contour length, b the temperature independent Kuhn length (see Table B.1), and f the applied force. The persistence length is given by $l_p = \kappa/(k_B T)$, where the bending rigidity κ is assumed to be temperature independent. Next, the free energy F is given by

$$F = U - TS \tag{4.3}$$

While the FJC model leads to $U/F = 0$ and $-TS/F = 1$, the WLC model leads to $U/F = -1$ and $-TS/F = 2$ with the energy U and the entropy S.[48] While in both cases TS/F is constant, F is proportional to T^n with $n = 1$ for the FJC model (for a temperature independent Kuhn length, see Table B.1) and $n = 2$ for the WLC model (for a temperature independent bending rigidity κ). By contrast, a purely energetic stretching response should be temperature independent, i.e., $n = 0$. We name regimes with exponents $n > 1$ as superentropic, $n < 0$ as superenergetic, and with $0 < n < 1$ as mixed.

The commonly used FJC and WLC models fail to describe the force-extension behavior of both PEG and PNiPAM over the whole force range (Figures B.8 and B.9).[48] In particular, both polymers deviate from a purely entropic spring model at intermediate and highly stretched states. In fact, they represent superenergetic or mixed springs with different temperature behavior, as discussed below.

The temperature-dependent force response of the PEG polymer is best analyzed by normalization with respect to T^n in order to find the optimal exponent n. The optimal value for n is obtained when the normalized free energy-force curves for the different temperatures superimpose. In particular, the optimal exponent n is found by the lowest coefficient of variation (ratio of standard deviation and mean value) for the different temperatures at each stretching force value (Figure B.10). Thus, the different regimes (entropic and energetic) can be distinguished along the course of the stretching force.

In Figure 4.4 the stretching free energy per length F/L_0, rescaled with various scaling exponents n, is shown in order to compare the regimes obtained from experiment and simulation. F is determined by integration of the master curves (force vs rescaled extension) given in Figures 4.2 and 4.3. Considering the different temperature ranges for the experiment and the MD simulation, the data agree qualitatively well. For low forces below 150 pN , the MD simulation data are best described by a scaling exponent $n = 1$,

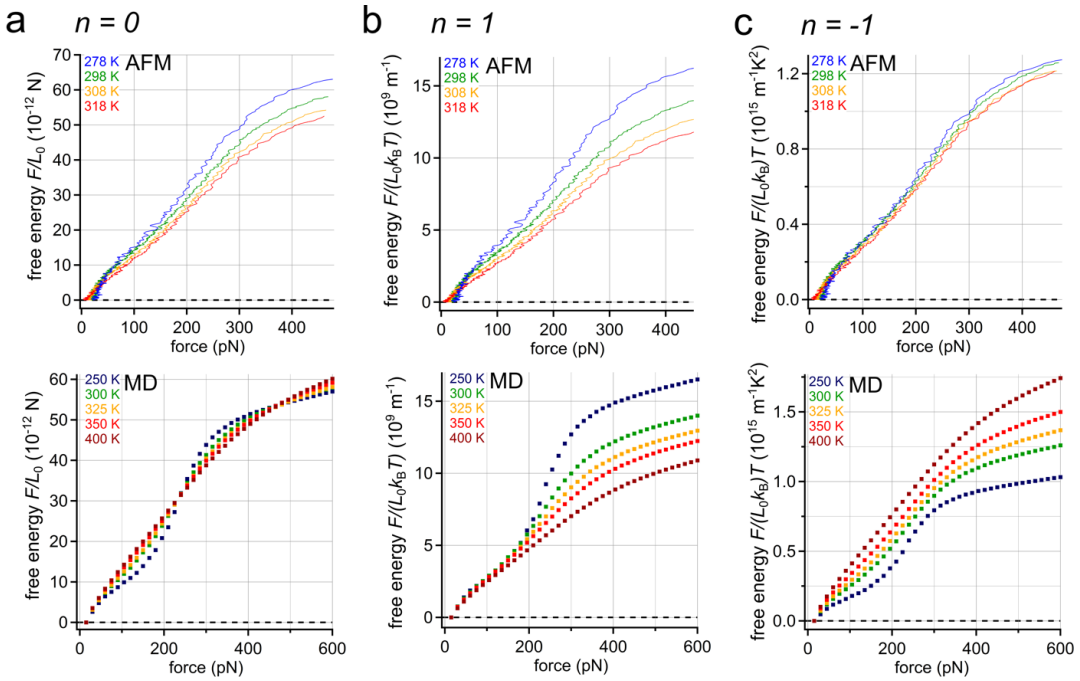

Figure 4.4: Temperature dependence of the stretching free energy F for experimental AFM data and the MD simulations of PEG: (a) stretching free energy F per L_0 (extension at a force of 500 pN) vs force (case $n = 0$); (b) F per L_0 divided by k_BT ($n = 1$); (c) F per L_0 divided by k_BT^{-1} ($n = -1$). Note the significantly larger temperature range in the simulations.

indicating purely entropic behavior (Figure 4.4b). In the AFM experiments, this purely entropic regime is already left at forces below 100 pN. Then, above 150 pN, more and more energy-dominated behavior is found for both the MD simulations and the AFM experiments. The AFM experiments even reach the superenergetic regime with $n = -1$ (Figure 4.4c). The MD simulation for the lowest temperature (250 K) shows a nonlinear course, but this temperature cannot be probed in experiments. At higher temperatures (300 K, 325 K, 350 K), where experiment and simulation can directly be compared, the shape of the curves qualitatively agrees well.

Altogether, the MD simulations are best described by an entropy dominated chain ($n = 1$) for forces up to 150 pN and an energetic chain ($n = 0$) starting at this intermediate force. The experiments already show significant superenergetic behavior starting from below 100 pN and finally dominant energetic contributions ($n = -1$) at higher stretching forces.

In order to understand the shift from entropic to energetic behavior, we examined the mean fraction of gauche and trans states in the PEG chain according to MD simulations. Figure 4.5a shows the mean fraction of monomers in the trans state for different temperatures as a function of force. The initially shallower increase of Φ_{trans} for low temperatures can be explained by a higher number of water bridges forming two hydrogen bonds with the PEG backbone, as depicted in Figure 4.5b. The decrease in the

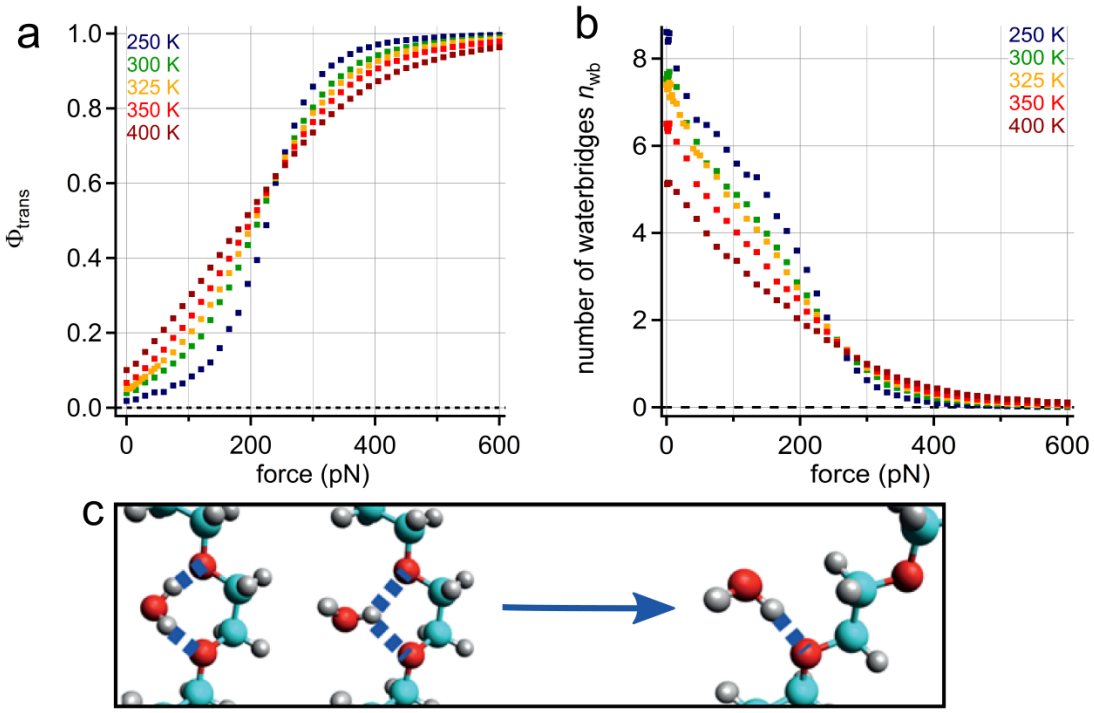

Figure 4.5: Molecular mechanism of PEG revealed by MD simulation data: (a) mean fraction of monomers in the trans state and (b) number of water bridges n_{wb} vs the stretching force for PEG at different temperatures ranging from 250 K to 400 K (with a PEG chain comprising 11 monomers). (c) Schematic picture of PEG in the gauche state with two hydrogen bonds (water bridge) involved (left) and a water molecule forming a single hydrogen bond with PEG in the trans state (right).[48]

number of water bridges explains the overall decrease in F/L_0 with increasing temperature (Figure 4.4a). In addition, the pronounced nonlinear behavior of Φ_{trans} for low temperatures around 250 pN can explain the increase in the slope of F/L_0 observed in Figure 4.4a at this force. Here the water bridges stabilize the gauche state, which has a smaller contour length compared to the trans state. This also explains the temperature-dependent crossover of PEG around 250 pN , which can be observed in Figure 4.4a and Figure 4.5. Note that a temperature-dependent contour length can be obtained using the FJC model to fit PEG force-extension curves (see Figure B.8) if a temperature independent Kuhn length is assumed (see Table B.1). Such a temperature-dependent contour length would just be a fit parameter with no real physical meaning, and we therefore argue that the exponent n discussed above better describes the underlying physical processes.

Figure 4.6 shows the stretching free energy for PNiPAM vs force for different temperatures determined analogously to the PEG data. In general, AFM experiments and MD simulations agree well. Again, we optimize the coefficient of variation to find the exponent n in the temperature dependence (Figure B.11). For the syndiotactic MD sim-

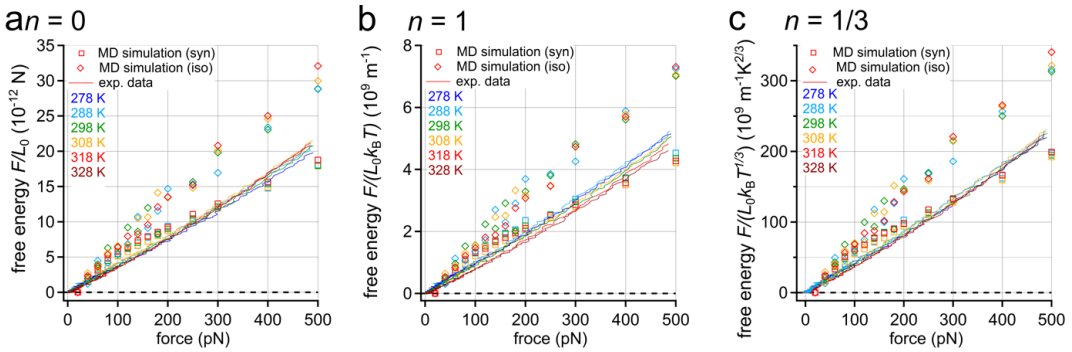

Figure 4.6: Temperature dependence of the stretching free energy F for the MD simulations of isotactic PNiPAM (open diamonds) and of syndiotactic PNiPAM (open squares) compared to experimental AFM data (atactic, lines): (a) stretching free energy F per L_0 (extension at a force of 500 pN) vs force (n = 0); (b) F per L_0 divided by k_BT ($n = 1$); (c) F per L_0 divided by $k_BT^{1/3}$ ($n = 1/3$).

ulations, a dominance of entropy ($n = 1$) up to 100 pN can be observed (Figure 4.6b). But for higher forces, $n = 1/3$ describes well the course of the temperature dependence of F/L_0, resulting in a dominance of the energetic character. In fact, the syndiotactic MD simulations are quite close to the atactic experimental data. Altogether, we obtain the best fit for $n = 1/3$, i.e. $F/L_0 \sim T^{1/3}$ (Figure 4.6c). In general, PNiPAM shows a mixed behavior ($0 < n < 1$) for the investigated stretching forces.

At the molecular scale the temperature-dependent stretching response of PNiPAM can be understood as follows:[208,243–246] At low temperatures, hydrogen bond bridges are formed between water molecules and the amide side groups. Thus, the polymer comprising a hydrophobic backbone is made soluble in water. When the temperature is increased, exothermic formation of hydrogen bonds becomes unfavorable. Therefore, the bound water molecules are released leading to a partial dehydration of the polymer. In parallel, intramolecular hydrogen bonding between the amide groups is favored (attractive interaction). Therefore, the polymer tends to collapse into a globular state, i.e., more force is required to keep the polymer at a certain extension compared to a lower temperature. For single PNiPAM molecules, as investigated here, we do not observe a sharp transition, which is rather attributed to cooperative effects as discussed in Futscher et al.,[209] but a gradual change.

The simulation of isotactic PNiPAM (Figure 4.6a, open rhombi) shows a similar linear relation of free energy F/L_0 with force. Here, due to the one-sided arrangement of the NiPAM monomer units, hydrogen bond bridges can be formed between two monomers. This presumably leads to a greater influence of the hydrogen bond bridges compared to the syndiotactic polymer, where the NiPAM monomer units are arranged in an alternating fashion with respect to the backbone leading to a less pronounced increase of free energy F/L_0 with force (Figure 4.6a, filled squares). Additionally, the magnitude of the experimental values for free energy per length F/L_0 (atactic polymer, Figure 4.6a, solid lines) is close to the simulated syndiotactic data (Figure 4.6a, open squares) while the

simulated isotactic values (Figure 4.6a, open diamonds) are about 1.5 times higher for a given force in the range of 200 pN to 500 pN. In conclusion, the tactility of PNiPAM is more important for the free energy to stretch the polymer at a given force than a change of temperature from 278 K to 328 K.

4.4 Conclusions

In a combined experimental and simulation approach, we have scrutinized the temperature dependence of single PEG and PNiPAM polymers. We have been able to develop a reliable procedure to covalently attach long polymers (at least 300 nm) to the tip of a Si_3N_4 AFM cantilever. This allows us to measure highly reproducible single polymer force-extension curves up to high stretching forces (approximately 800 pN), excluding any interactions with neighboring polymer chains, which proved difficult in other experiments (e.g., nanofishing). Our truly single molecule experiments are consistent with MD simulations in explicit solvent at various temperatures. For PNiPAM we could show that neither the shape nor the frequency of the recorded force-extension curves is significantly changed around the LCST at the investigated forces. The LCST is therefore indeed a cooperative effect.
In addition, we find that PEG and PNiPAM show a contrasting temperature stretching response in water. While the stretching force increases with increasing temperature for PNiPAM, a decrease in the stretching force for increasing temperatures can be observed for PEG. The experimental temperature-dependent stretching response of PEG and PNiPAM is also in good agreement with the MD simulation.
Furthermore, both experimental data and MD simulations show a decrease of the force dependent stretching free energy of PEG with increasing temperature for stretching forces starting at about 100 pN. This can be explained by the influence of temperature on the mean fraction of gauche and trans states of the PEG chain and the corresponding reduction of the number of water bridges during stretching. PNiPAM already shows a nonlinear dependence of the free energy per length on temperature at the lowest probed stretching forces (approximately 10 pN).
In summary both single PEG and PNiPAM molecules do not represent purely entropic springs. Their stretching free energy is dominated by energetic solvation effects at a wide range of stretching forces. This shows that although the FJC and WLC models are very helpful for comparing polymer properties, the physical interpretation of the resulting parameters has to be done with care. In particular, as has been found before, both models do not mimic the force- extension behavior over the full range of stretching forces. Here we could further show that they also do not correctly describe the temperature-dependent force-extension behavior, in particular for highly stretched polymers under aqueous conditions.
We propose using the exponent n of the temperature dependence of the normalized stretching free energy (F/L_0) as a measure for the degree of energetic vs entropic character of a polymer. A purely entropic chain is defined by $n = 1$, as obtained in the FJC

model with temperature independent Kuhn length. For PEG we find a superenergetic stretching response with $n < 0$. For PNiPAM, we find a mixed stretching response with $0 < n < 1$. Thus, we are able to classify the temperature stretching response of different polymers and to show that PEG has a more dominant energetic character than PNiPAM. At the molecular level, both polymers lose hydrogen bonds with the surrounding water with rising temperature. At the same time, for PNiPAM, intermolecular hydrogen bonds are formed that compensate for that loss. Thus, PNiPAM shows an antagonistic temperature-dependent force-extension stretching response compared to PEG.
This paves the way for understanding temperature responsive polymers and for designing block copolymer structures for a tailor-made temperature behavior. Materials comprising blocks with antagonistic temperature dependence could be used for switches or actuators[191,247] analogous to the bimetallic effect. In molecular switches, prestressed building blocks could be used to adjust the force range. In addition, current thermoresponsive materials are often cross-linked polymer hydrogels.[248] In hydrogels, tensile stress might be concentrated on a small fraction of available chains, which locally leads to a very high tensile stress. In addition, small molecular effects, as observed here, might translate into significant macroscopic effects, e.g., in hierarchical structures,[249] or the devices might be implemented at significant prestress to increase the temperature response. Finally, some future adaptive force sensors could use a polymeric system that can reach or operate in a highly stretched state.[250]

Chapter 5

Hydrodynamic Shear Effects on Grafted and Non-Grafted Collapsed Polymers

Bibliographic information: This chapter and appendix C have previously been published. Reprinted with permission from Ref. [iv], https://doi.org/10.3390/polym10080926. License: CC BY 4.0.

Author contribution statement: Richard Schwarzl carried out all simulations and the analysis of the data. Roland R. Netz supervised the project. Richard Schwarzl created all figures and wrote the first version of the manuscript. Both authors contributed to the final version of the manuscripts, which is published under: R. Schwarzl and R. R. Netz, Hydrodynamic Shear Effects on Grafted and Non- Grafted Collapsed Polymers, Polymers 10, 926 (2018).

5.1 Introduction

The von Willebrand factor (VWF) is a large glycoprotein that is crucially involved in primary hemostasis.[76] The ability to mediate platelet adhesion at sites of vascular injury depends on the activation stage of VWF[77,251,252] and its insufficiency has been linked to bleeding disorders.[253]
The proposed mechanism for the activation of the VWF is the elongation and partial unfolding by elevated shear flow conditions due to vasoconstriction.[74,75,251,254] This implicates a collapsed state of VWF present under normal shear flow conditions and a shear-flow induced transition into a partly unfolded state.[75] The behavior of collapsed as well as coiled polymers in shear flow has been at the focus of theoretical and experimental research.[74,75,255–259] Previous studies have used simulations and theoretical considerations to explain the globular-coil transition due to linear shear flow for collapsed polymers in the vicinity of the vessel wall.[74,260,261] Despite the fact that the grafted scenario might be even more relevant, the non-grafted scenario has been studied

intensively in simulations so far. The relevance of the grafted scenario arises from the fact that upon activation, VWF binds to sub-endothelial collagen.[68,83,252,262–264]
In the present study, we focus on the grafted scenario, which frequently appears in atomic force microscopy (AFM) measurements,[68,252,265] and compare it to the non-grafted scenario. We conduct Brownian dynamics simulations including long range hydrodynamic interactions (HI) on the Rotne-Prager level[40,266] under linear shear flow conditions. Although some stationary dynamic chain properties are independent of hydrodynamic effects,[267] hydrodynamic interactions crucially influence the scaling behaviour of the critical shear rate of the globular-coil transition.[74,75] These results shed light on time scales relevant for the regulatory mechanisms linked to the domain opening of VWF in the grafted scenario. One of the additional regulatory mechanisms that has been studied in more detail, is the cleavage of VWF by means of the enzyme ADAMTS-13.[80,81] Relating simulations and results from atomic force microscopy (AFM) via rate theories[68,268–271] has been argued to offer a promising route to investigate domain specific activation times of VWF.
In the first part of this study, scaling laws for the critical shear rate are deduced from simulation results. We find the dependence of the critical shear rate on the number of monomers to be inverted for the grafted compared to the non-grafted scenario, i.e., for the grafted scenario, an increase in polymer size reduces the critical shear rate while for the non-grafted scenario the critical shear rate is increased. In the second part, we connect the unfolding of the polymer to the tensile force profile and investigate the interplay of drag and lift force that determines the configurations of the grafted chain. In addition, we investigate the mean and the maximum of the tensile force profile for the grafted and non-grafted chain at the critical shear rate. These forces and their scaling with the number of monomers are relevant for the shear-dependent folding and unfolding times of VWF domains.

5.2 Methods

5.2.1 The Model

We describe the VWF by a bead-spring model. The beads are numerated from 1 up to the total number of beads, N. Each bead has a radius of a which is associated with an effective radius of a VWF dimer of 73 nm.[81] A schematic description of the VWF model is given in Figure 5.1. The position vectors of the beads are denoted by $\mathbf{r}_1, \ldots, \mathbf{r}_N$. The backbone of the chain is realized by a series of springs, with a spring constant $\kappa = 200\,\mathrm{k_B Ta^{-2}}$, that connect neighbouring beads. The potential of each spring is given as

$$U_{\mathrm{SP}}(|\mathbf{r}_{i+1} - \mathbf{r}_i|) = \frac{\kappa}{2}\left(|\mathbf{r}_{i+1} - \mathbf{r}_i| - 2a\right)^2 . \tag{5.1}$$

All beads interact pairwise by a Lennard-Jones interaction with a cohesion strength ε, which in our study is set to $2\mathrm{k_B T}$,

$$U_{\mathrm{LJ}}(|\boldsymbol{r}_i - \boldsymbol{r}_j|) = \varepsilon \left[\left(\frac{2a}{|\boldsymbol{r}_i - \boldsymbol{r}_j|} \right)^{12} - 2 \left(\frac{2a}{|\boldsymbol{r}_i - \boldsymbol{r}_j|} \right)^{6} \right]. \tag{5.2}$$

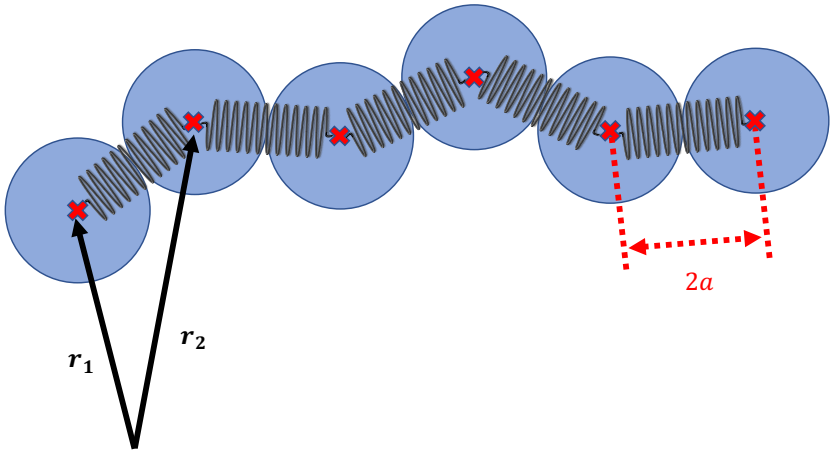

Figure 5.1: Schematic picture of the bead-spring model of the von Willebrand factor. The beads are numerated from 1 to N and their respective position vectors are denoted by $\mathbf{r}_1, \ldots, \mathbf{r}_N$. The harmonic springs connecting consecutive beads have a stiffness of $\kappa = 200\,\mathrm{k_B Ta^{-2}}$.

The value for the cohesion strength was previously obtained by fitting simulation results of the bead-spring model for the globule-to-coil transition to experimental data.[75] Note that for the relatively large VWF monomers considered here, the dispersion interaction will, for small separation, lead to a different interaction potential than the Lennard-Jones interaction given in eq 5.2. We thus view eq 5.2 as a model potential, in line with previous work. The total potential energy of our system follows as

$$U(\mathbf{r}_1, ..., \mathbf{r}_N) = \sum_{i=1}^{N-1} \sum_{j>i}^{N} U_{\mathrm{LJ}} \left(|\mathbf{r}_i - \mathbf{r}_j| \right) + \sum_{i=1}^{N-1} U_{\mathrm{SP}} \left(|\mathbf{r}_{i+1} - \mathbf{r}_i| \right). \tag{5.3}$$

5.2.2 Simulation Details

We perform Brownian dynamics simulations of a single chain using a discretized version of the over-damped Langevin equation,[40,261]

$$\frac{\mathbf{r}_i(t + \Delta t) - \mathbf{r}_i(t)}{\Delta t} = \dot{\gamma} z_i \mu_0^{-1} \boldsymbol{\mu}_{ii} \cdot \hat{\mathbf{x}} - \sum_{j=1}^{N} \boldsymbol{\mu}_{ij} \cdot \left[\nabla_{\mathbf{r}_j(t)} U(\mathbf{r}_1, ..., \mathbf{r}_N) \right] + k_{\mathrm{B}} T \frac{\mathrm{d}\mu_{ii}^{zz}}{\mathrm{d}z} \Big|_{z=z_i} \hat{\mathbf{z}} + \boldsymbol{\xi}_i(t), \tag{5.4}$$

which is used to recursively calculate the displacement of a bead i in a specified time step Δt. The first term on the right-hand side of eq 5.4 accounts for the linear shear

flow proportional to the shear rate $\dot{\gamma}$. The direction of the flow is given by the unit vector in x direction, denoted as $\hat{\mathbf{x}}$. The mobility tensor $\boldsymbol{\mu}$ and random velocity $\boldsymbol{\xi}_i$ are different for the grafted and non-grafted scenarios.
For the non-grafted situation, we use the Rotne-Prager-Yamakawa tensor to calculate the mobility of all beads. Due to the absence of a no-slip boundary in this scenario, the third term on the right side of eq 5.4 vanishes. The Rotne-Prager-Yamakawa tensor is given by [272]

$$\boldsymbol{\mu}_{ij} = \boldsymbol{\mu}^{\mathrm{RPY}}\left(\boldsymbol{r}_{ij} = \boldsymbol{r}_i - \boldsymbol{r}_j\right) = \begin{cases} \frac{1}{8\pi\eta r_{ij}}\left[\left(1 + \frac{2a^2}{3r_{ij}^2}\right)\mathbb{1} + \left(1 - \frac{2a^2}{r_{ij}^2}\right)\hat{\mathbf{r}}_{ij} \otimes \hat{\mathbf{r}}_{ij}\right] & \text{if } r_{ij} > 2a \\ \frac{1}{6\pi\eta a}\left[\left(1 - \frac{9r_{ij}}{32a}\right)\mathbb{1} + \frac{3r_{ij}}{32a}\hat{\mathbf{r}}_{ij} \otimes \hat{\mathbf{r}}_{ij}\right] & \text{if } r_{ij} \leq 2a \end{cases}, \tag{5.5}$$

where $r_{ij} = |\boldsymbol{r}_i - \boldsymbol{r}_j|$.
For the grafted scenario which includes a no-slip boundary at $z = 0$, we use the Rotne-Prager-Blake tensor that was previously derived, [266]

$$\boldsymbol{\mu}_{ij} = \boldsymbol{\mu}^{\mathrm{RPB}}\left(\boldsymbol{r}_i, \boldsymbol{r}_j\right) = \boldsymbol{\mu}^{\mathrm{RP}}\left(\boldsymbol{r}_i - \boldsymbol{r}_j\right) - \boldsymbol{\mu}^{\mathrm{RP}}\left(\boldsymbol{r}_i - \bar{\boldsymbol{r}}_j\right) + \boldsymbol{\Delta\mu}\left(\boldsymbol{r}_i, \boldsymbol{r}_j\right), \tag{5.6}$$

where $\bar{\boldsymbol{r}}_j = (x_j, y_j, -z_j)^{\mathrm{T}}$ is the mirror image position and $\boldsymbol{\mu}^{\mathrm{RP}}$ is the Rotne-Prager tensor. The explicit terms of the Rotne-Prager-Blake tensor are given in the supplementary material.
The random velocity in eq 5.4, $\boldsymbol{\xi}_i$, follows from the fluctuation-dissipation theorem,

$$\langle \boldsymbol{\xi}_i(t) \otimes \boldsymbol{\xi}_j(t') \rangle = 2k_{\mathrm{B}}T\boldsymbol{\mu}_{ij}\delta(t - t'). \tag{5.7}$$

We use the Cholesky factorization to decompose the entire mobility matrix $\boldsymbol{\mu}$ into a lower triangular matrix $\mathbf{L}$ and its transposed. The lower triangular matrix is then multiplied with a random Gaussian vector to obtain correlated values that obey the required variance condition given by eq 5.7.
For the grafted scenario, we introduce an additional repulsive potential that prevents the beads to cross the no-slip boundary at $z = 0$. This potential is given by [273]

$$U_{\mathrm{R}}(\boldsymbol{r}_i) = \begin{cases} \frac{2\pi k_{\mathrm{B}}T\sigma_R}{a}\left[\frac{2}{5}\left(\frac{\sigma_{\mathrm{R}}}{z_i}\right)^{10} - \left(\frac{\sigma_{\mathrm{R}}}{z_i}\right)^{4} + \frac{3}{5}\right] & \text{if } z_i \leq \sigma_{\mathrm{R}} \\ 0 & \text{if } z_i > \sigma_{\mathrm{R}} \end{cases} \tag{5.8}$$

where σ_{R} is chosen to be 1.5 a. This repulsive potential makes sure that the approximation made for the parallel and perpendicular self-mobilities in the derivations of the expressions obtained by Perkins, Jones, Stimson and Jeffery remain valid (cf. von Hansen, et al., Figure 1). [266,274,275]
In simulations for the grafted scenario, the first bead is modelled as an anchor point. The position of the first bead is therefore not updated in the simulation. There is also no hydrodynamic interaction between the first bead and any other bead in the simulation. Hence the mobility matrix for this case is not $3N$ dimensional but rather $3(N-1)$

dimensional.
Simulation parameters and results are given in rescaled units. These units are the bead radius a, the thermal energy k_BT and the diffusion time $\tau = 6\pi\eta\ a^3/(k_BT) = a^2/(\mu_0 k_BT)$. The simulation time step is consistently chosen to be $\Delta t/\tau = 5\times10^{-4}$ and simulations are run for at least 2×10^8 steps, resulting in a minimum simulation time of $10^5\tau$. Positions of all beads are saved at least every 10^5 steps. When we calculate an observable from trajectories, we always omit the first 10^6 steps for equilibration.
Throughout our simulations, we do not observe self-entanglement effects, which experimentally are known to exist for DNA.[276] Note that in similar simulations at larger cohesion strength, a non-monotonic behaviour of the chain size on shear rate has been reported and rationalized by entanglement effects.[277]

5.3 Results

In our study, we systematically vary the shear rate, $\dot{\gamma}$, as well as the number of beads, N, of the bead-spring chain and therefore its contour length which is given as $L = 2(N-1)a$.

5.3.1 Scaling of Critical Shear Rate

As we show in Figure 5.2, both the grafted as well as the non-grafted scenarios exhibit a shear-induced globule-to-coil transition. We identify this transition by calculating the mean-squared radius of gyration of the chain for different shear rates defined as

$$R_G^2 = \frac{1}{2N}\sum_{i=1}^{N}\sum_{j=1}^{N}(\boldsymbol{r}_i - \boldsymbol{r}_j)^2. \tag{5.9}$$

In Figure 5.2, we see a narrow shear rate range over which a significant increase of the time-averaged radius of gyration is observed. This reflects a conformational change of the bead-spring chain from a collapsed state caused by cohesion, which is verified by the scaling relation of $R_G^2 \sim (N-1)^{2/3}$ at $\dot{\gamma} = 0$ shown in Figure 5.3, to a non-collapsed state.

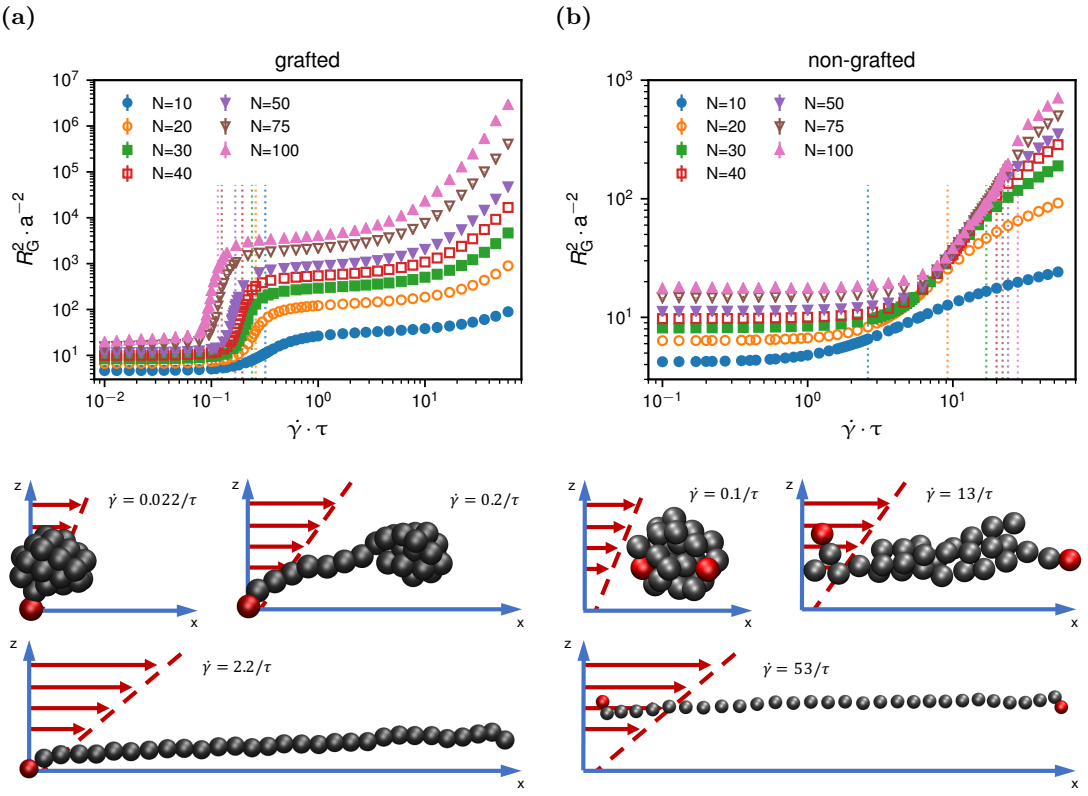

Figure 5.2: An increase of the shear rate $\dot{\gamma}$ above a certain threshold, which depends on the size of the chain, initiates a transition from a collapsed to a coiled or extended state. The vertical dashed lines relate to the steepest increase of the mean-squared radius of gyration as a function of the shear rate. We present results for different monomer numbers N. Subfigures (**a**,**b**) show the grafted and non-grafted cases, respectively. We also show simulation snapshots for $N = 30$ below, at and above the critical shear rate of $\dot{\gamma}^* = 0.24\ \tau^{-1}$ for the grafted and $\dot{\gamma}^* = 13\ \tau^{-1}$ for the non-grafted scenario.

Chains in shear flow show large size fluctuations.[278] To determine the transition between the collapsed and non-collapsed states, we analyse quantities that characteristically depend on the shear rate and exhibit an extremum at the transition. Previous publications used R_S^2, a quantity that measures the mean-squared extension of the bead-spring chain in flow-direction.[81,260,261] This quantity is defined as the maximal squared distance between any two beads after projecting their positions onto the flow-direction:

$$R_S^2(t) = \max_{i,j \in \{1,\ldots,N\}} \left[(\boldsymbol{r}_{ij} \cdot \hat{\mathbf{x}})^2 \right]. \tag{5.10}$$

The motivation behind this definition is that the relative fluctuation of the squared extension in flow direction, defined as

$$\sigma_{R_S^2} / R_S^2 = \sqrt{\langle R_S^4(t) \rangle - \langle R_S^2(t) \rangle^2} / \langle R_S^2(t) \rangle, \tag{5.11}$$

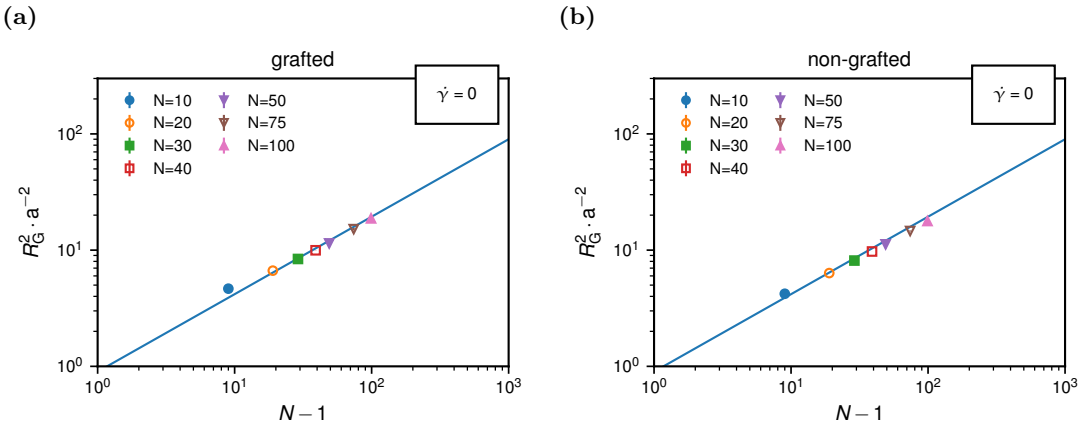

Figure 5.3: Equilibrium results for zero shear rate ($\dot{\gamma} = 0$): The mean-squared radius of gyration, R_G^2, as function of the monomer number, $N-1$, is described by the expected scaling law for collapsed polymers, $R_G^2 \sim (N-1)^{2/3}$, shown as a blue line both in (**a**) the grafted and (**b**) the non-grafted scenarios.

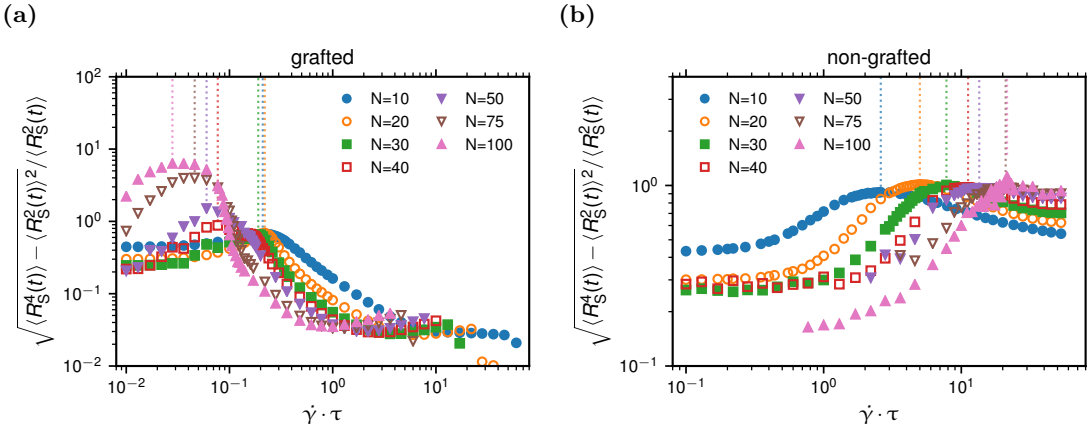

Figure 5.4: The maximum of the normalized standard deviation of the mean-squared elongation of the chain in flow direction, $\sqrt{\langle R_S^4(t)\rangle - \langle R_S^2(t)\rangle^2}/\langle R_S^2(t)\rangle$, has previously been used to define the critical shear rate indicated by dashed lines.[260] Subfigures (**a**,**b**) depict the grafted and the non-grafted scenario, respectively.

is maximal, when the probability of the bead-spring chain for changing from a collapsed to a non-collapsed state is the highest. For comparison with previous publications, we show $\sigma_{R_S^2}/R_S^2$ over $\dot{\gamma}$ in Figure 5.4.

In addition to the relative fluctuations $\sigma_{R_S^2}/R_S^2$, we analysed several other quantities in terms of their dependence on the shear rate which we present in the supplementary material. In Figure 5.5, we compare the results for the critical shear rate as a function of N deduced from the maximum of the relative fluctuations and from the maximum

of the numerical derivative of the two measures, R_S^2 and R_G^2, with respect to $\dot{\gamma}$. Note that the grafted and the non-grafted scenario show qualitatively different behaviours of the critical shear rate upon increasing the chain length. In the non-grafted case, an increase of the chain length leads to an increase in critical shear rate, whereas for the grafted scenario, an increase in chain length actually decreases the critical shear rate. Our results for the critical shear rate in the non-grafted case are in reasonable agreement with the previously derived scaling relation in the presence of hydrodynamic interactions, $\dot{\gamma}^* \sim (N-1)^{1/3}$.[260] From our simulation results, we find that the grafted scenario exhibits a different scaling according to $\dot{\gamma}^* \sim (N-1)^{-1/3}$ which we show Figure 5.5a. This scaling can be explained by the fact that the anchor of the chain forms a protrusion, as soon as the cohesion force, $F_C \sim \varepsilon/a \sim k_B T/a$, can be overcome. Below the critical shear rate, the drag force acting on the globule is given by $F_D \sim \dot{\gamma}\,(N-1)^{1/3}$ assuming that the drag force is proportional to the flow velocity at the position of the center of mass of the chain. Equating these two forces, we find $\dot{\gamma}^* \sim (N-1)^{-1/3}$. Hence, we find the scaling laws

$$\dot{\gamma}^* \sim \begin{cases} (N-1)^{-1/3} & \text{(HI, grafted)} \\ (N-1)^{1/3} & \text{(HI, non-grafted)} \end{cases}, \tag{5.12}$$

which in Figure 5.5 are presented as solid lines and shown to describe the simulation data well.

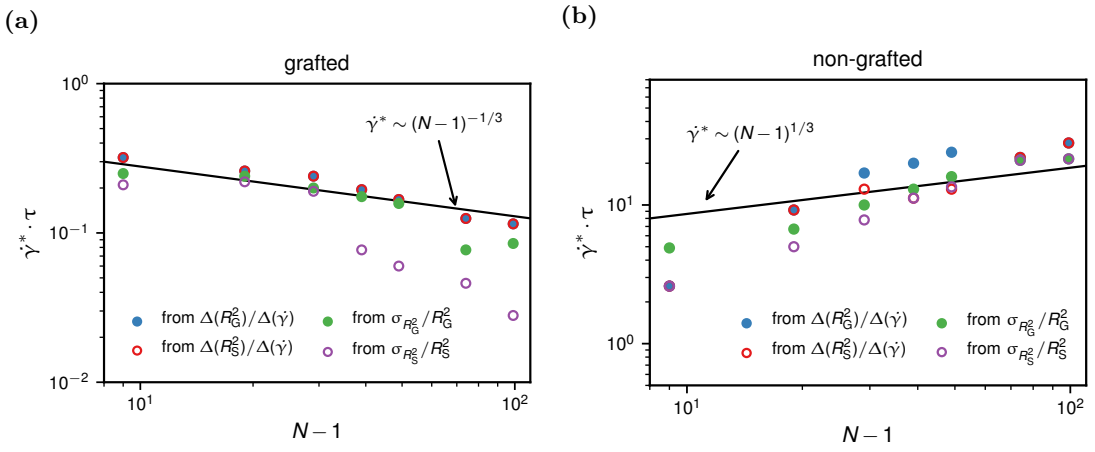

Figure 5.5: The critical shear rate, $\dot{\gamma}^*$, for the grafted and non-grafted scenarios as determined by four different criteria. We present the numerical derivatives and the normalized standard deviations of R_G^2 and R_S^2, indicated by dashed vertical lines in Figures 5.2 and 5.4, as a function of $N-1$. The scaling predictions according to eq 5.12 are shown as solid lines.

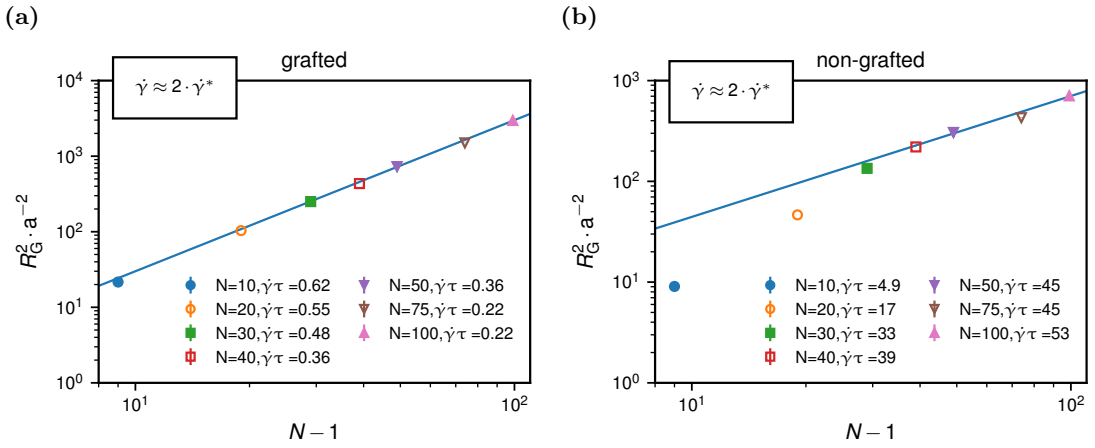

Figure 5.6: Squared radius of gyration slightly above the critical shear rate at $\dot{\gamma} \approx 2\dot{\gamma}^*$: The course of R_G^2 as a function of $N-1$ suggests for (**a**) the grafted scenario that the chain is fully stretched, $R_G^2 \sim N^2$, and (**b**) the non-grafted scenario that the chain is swollen, $R_G^2 \sim N^{6/5}$. The scaling relations shown as blue lines are given in eq 5.13.

In Figure 5.6, we present R_G^2 at twice the critical shear rate in dependence of $N-1$. This characterizes the chain conformation slightly above the critical shear rate. We find a fully stretched conformation for the grafted scenario, while for the non-grafted case the conformation corresponds to a
swollen polymer:

$$R_G^2 \sim \begin{cases} (N-1)^2 & (\text{at } \dot{\gamma} = 2\dot{\gamma}^*, \text{ grafted}) \\ (N-1)^{6/5} & (\text{at } \dot{\gamma} = 2\dot{\gamma}^*, \text{ non-grafted}) \end{cases}. \tag{5.13}$$

We note that shear-induced transitions are usually referred to as globular-coil transitions.[75,81,279] However, in the grafted scenario the transition turns out to be rather a globular-stretch transition.

5.3.2 Tensile Force Profiles

The transition from a collapsed to a coiled or a stretched polymer upon increase of the shear rate is driven by a change in the tensile force profile inside the chain. The linear springs that connect the polymer beads act as force sensors for the tensile stress which counteracts the sum of shear stress and Lennard-Jones interactions. The absolute value of the distance between two beads along the chain contour determines the tensile force as

$$f_i = \kappa \left(|\mathbf{r}_{i+1} - \mathbf{r}_i| - 2a \right) \quad , i \in \{1, \ldots, N-1\}. \tag{5.14}$$

Tensile forces shown in the following are always averaged over the course of a simulation by averaging the distance between consecutive beads.

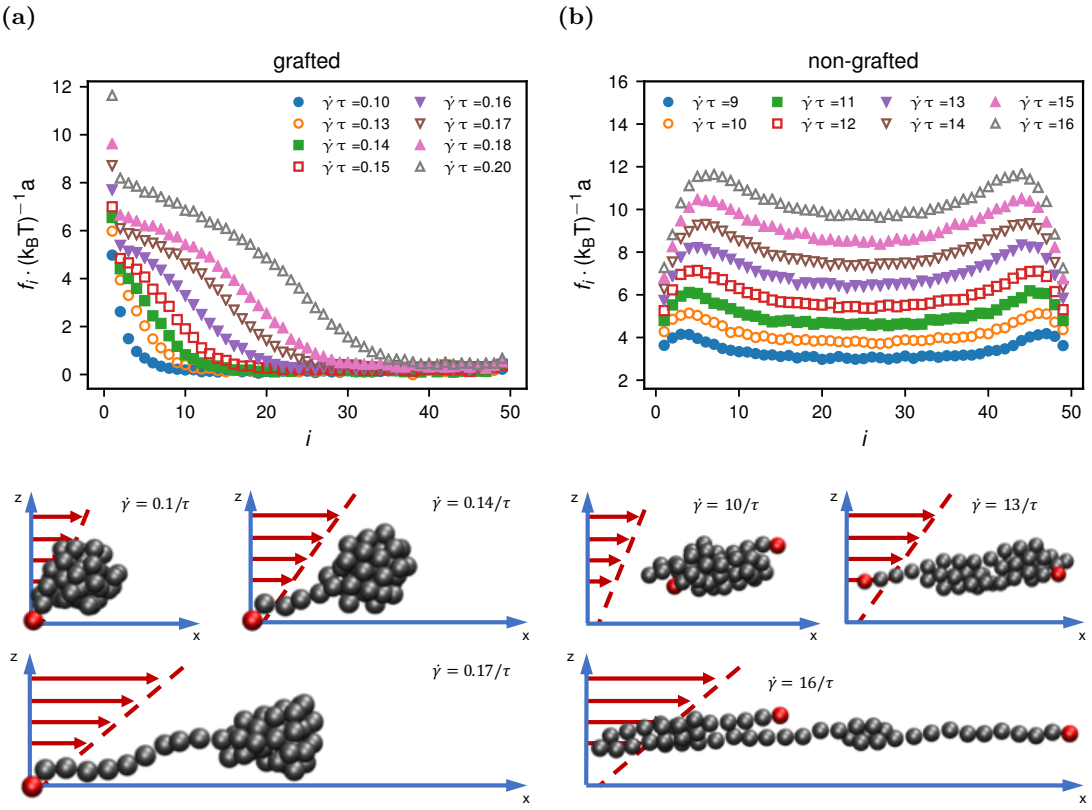

Figure 5.7: Comparison of tensile force profiles of a bead-spring chain with $N = 50$ for different shear rates in the vicinity of the critical shear rate $\dot{\gamma}^* = 0.168\ \tau^{-1}$ for the (**a**) grafted and $\dot{\gamma}^* = 13\ \tau^{-1}$ for the (**b**) non-grafted case. These critical shear rates are based on the maximum of the numerical derivatives of R_g^2. We also present simulation snapshots that illustrate the different unfolding mechanisms in the grafted and non-grafted scenarios.

In Figure 5.7, we show the tensile force profiles in a small shear rate range around the critical shear rate for $N = 50$ of $\dot{\gamma}^* = 0.168\ \tau^{-1}$ in the grafted and $\dot{\gamma}^* = 13\ \tau^{-1}$ in the non-grafted scenarios. These tensile force profiles significantly differ between the grafted and non-grafted scenarios. The grafted case shows a maximum of the tensile force at the grafted monomer, followed by a monotonic decrease along the chain. Below the critical shear rate $\dot{\gamma}^* = 0.168\ \tau^{-1}$, most of the beads on average feel no tensile force. In the vicinity of the critical shear rate, the number of stretched bonds increases. What this shows is that depending on the shear rate, a subsection of the chain is elongated while the remaining part is still collapsed. In contrast, for the non-grafted case the maximum of the tensile force propagates towards the middle of the chain with increasing $\dot{\gamma}$, consistent with the protrusion mechanism for shear-induced unfolding introduced previously.[75,81,260]

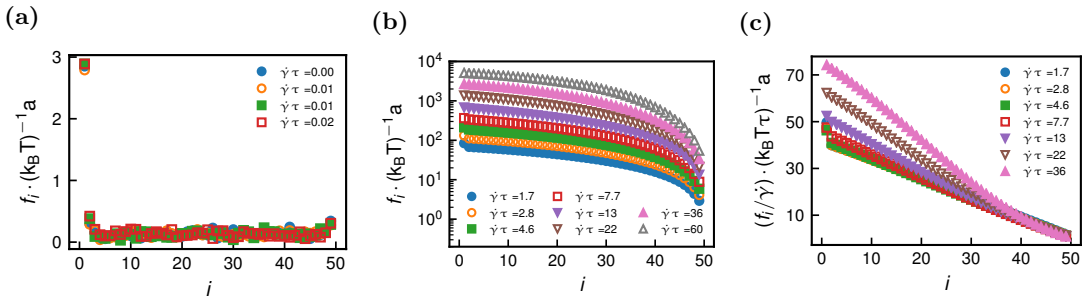

Figure 5.8: Grafted scenario: Tensile force profiles ($N = 50$) for shear rates (**a**) far below and (**b**) far above the critical shear rate $\dot\gamma^* = 0.168\ \tau^{-1}$. In subfigure (**c**), we demonstrate the strong-stretching scaling collapse $f_i \sim \dot\gamma$ predicted by Sing and Alexander-Katz.[280] Deviations from the scaling collapse coincide with a strong increase in mean radius of gyration shown in Figure 5.2a and are due to the extensible chain model.

When $\dot\gamma$ becomes significantly larger than $\dot\gamma^*$, the tensile force profile takes a characteristic form, shown in Figure 5.8b, which has been studied in detail both theoretically and in simulations by Sing and Alexander-Katz.[280] Figure 5.8c demonstrates the predicted scaling relation, $f_i \sim \dot\gamma$. Above a certain shear rate value, we see deviations from the strong stretching scaling $f_i \sim \dot\gamma$, which is accompanied by a steep increase of R_G^2 with $\dot\gamma$ in Figure 5.2a and which is due to our usage of an extensible chain model.

5.3.3 Scaling of Lift and Drag for the Grafted Chain

In Figure 5.9b, we show the mean positions of individual beads in the $x - z$ plane for a chain with $N = 50$ for different shear rates. In Figure 5.9a we also add the standard deviations, which demonstrates that the chain positions fluctuate significantly. To characterize the change in conformation of the bead-spring chain for the grafted case, we calculate the mean center of mass of the chain, which is defined as

$$\langle \mathbf{r}_{\mathrm{com}} \rangle = \frac{1}{N} \sum_{i=1}^{N} \langle \mathbf{r}_i \rangle, \tag{5.15}$$

and project it onto the plane of the shear flow. We define the angle α between the wall and the center of mass as shown in Figure 5.9c. To determine the scaling of α with N in different shear rate regimes, we examine the scaling of the projected center of mass positions $\langle r_{\mathrm{com,x}} \rangle$ and $\langle r_{\mathrm{com,z}} \rangle$. Figure 5.10 shows simulation results from which we extract the following heuristic scaling relations,

$$\langle r_{\mathrm{com,x}} \rangle \sim \begin{cases} (N-1)\ \dot\gamma & (\text{below } \dot\gamma^*) \\ (N-1) & (\text{above } \dot\gamma^*) \\ (N-1)^2\ \dot\gamma & (\text{far above } \dot\gamma^*) \end{cases} \tag{5.16}$$

and

$$\langle r_{\mathrm{com,z}} \rangle \sim \begin{cases} (N-1)^{1/3} & \text{(below } \dot{\gamma}^*\text{)} \\ \text{approximately independent of } (N-1) \text{ and } \dot{\gamma} & \text{(above } \dot{\gamma}^*\text{)} \end{cases}. \tag{5.17}$$

We discuss the scaling of the angle α by considering the geometric relation $\tan(\alpha) = \langle r_{\mathrm{com,z}}/r_{\mathrm{com,x}} \rangle$. Note that $\tan(\alpha)$ directly relates to the force balance between the drag force, F_{D}, exerted on the chain by shear flow, and the hydrodynamic lift force, F_{L}. As long as that angle is much larger than 45°, which corresponds to the regime below the critical shear rate, we can use the relation $\arctan(x) \approx \pi/2 - 1/x$ to deduce from eqs 5.16 and 5.17 the scaling of α as

$$\alpha \approx \frac{\pi}{2} - \frac{\langle r_{\mathrm{com,x}} \rangle}{\langle r_{\mathrm{com,z}} \rangle} = \frac{\pi}{2} - \text{const } \dot{\gamma}\ (N-1)^{2/3} \quad \text{(below } \dot{\gamma}^*\text{)}, \tag{5.18}$$

which is confirmed in Figure 5.11b. This means that for low shear rates the change in angle α is governed by the drag force $F_{\mathrm{D}} \sim vR \sim \dot{\gamma}(N-1)^{2/3}$.
When we consider shear rates slightly above the critical shear rate, where α becomes significantly smaller than 45°, we can use $\arctan(x) \approx x$, to derive the scaling given as

$$\alpha \approx \frac{\langle r_{\mathrm{com,z}} \rangle}{\langle r_{\mathrm{com,x}} \rangle} \sim (N-1)^{-1} \quad \text{(above } \dot{\gamma}^*\text{)}, \tag{5.19}$$

which is confirmed in Figure 5.11c. For shear rates far above the critical shear rate, simulation results suggest the scaling $\alpha \sim (N-1)^{-2}\ \dot{\gamma}^{-1}$ which is deduced from eqs 5.16 and 5.17. In Figure 5.12a, we show the results for the dependence of the critical angle α^* on the monomer number, which is well described by the scaling relation $\alpha^* \sim (N-1)^{-2/3}$. To derive this, we use that for the grafted scenario at the critical shear rate, the chain is already significantly stretched, i.e. we can use the same approximation for α^*

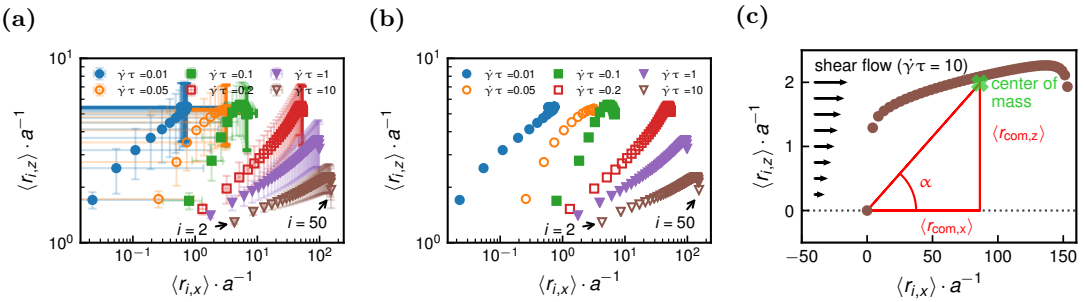

Figure 5.9: Grafted scenario: Subfigure (**a**) depicts the shear-rate-dependent mean position of individual beads of a chain with $N = 50$ in the $x-z$ plane together with the respective standard deviations. Subfigure (**b**) only shows the mean positions. The mean center of mass coordinates in x and z direction, $\langle r_{\mathrm{com,x}} \rangle$ and $\langle r_{\mathrm{com,z}} \rangle$, are exemplarily shown for the shear rate $\dot{\gamma} = 10\ \tau^{-1}$ in subfigure (**c**).

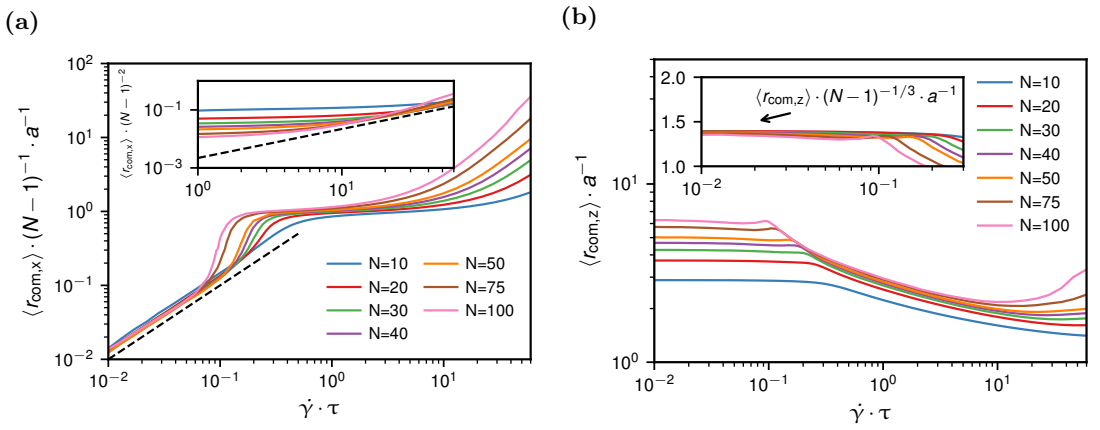

Figure 5.10: Grafted scenario: Subfigures (**a**,**b**) show the scaling collapse of $\langle r_{\mathrm{com,x}}\rangle$ and $\langle r_{\mathrm{com,z}}\rangle$ with respect to the monomer number as a function of the shear rate $\dot{\gamma}$ according to eqs 5.16 and 5.17. The dashed lines in subfigure (**a**) have slopes one and illustrate the proportionality to $\dot{\gamma}$.

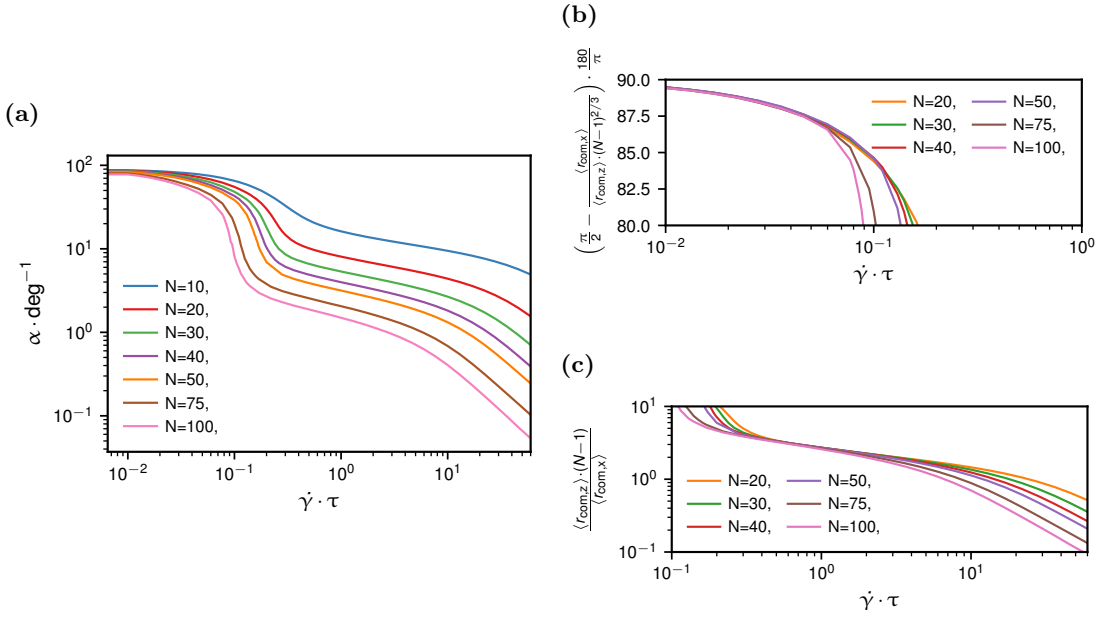

Figure 5.11: Grafted scenario: Subfigure (**a**) shows the dependence of the angle α, graphically defined in Figure 5.9c, on the chain length and on the shear rate. The scaling relations for the projections of the center of mass positions given by eqs 5.16 and 5.17 lead to the scaling of α below the critical shear rate, given by eq 5.18 and shown in subfigure (**b**) and above the critical shear rate, given by eq 5.19 and shown in subfigure (**c**).

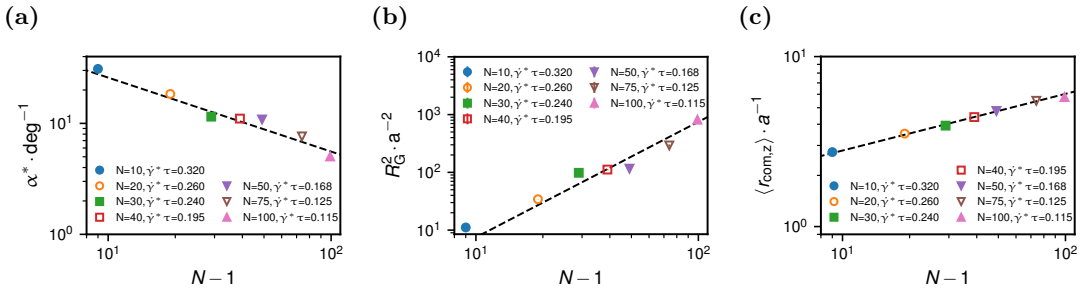

Figure 5.12: Grafted scenario at the critical shear rate $\dot{\gamma}^*$: Subfigure (**a**) depicts the simulation results for the angle α, subfigure (**b**) for the mean-square radius of gyration R_G^2 and subfigure (**c**) for the projection $\langle r_{com,z} \rangle$ depending on the monomer number, $N-1$. The deduced heuristic scaling relations which are indicated by dashed lines are $\alpha \sim (N-1)^{-2/3}$, $R_G^2 \sim (N-1)^2$ and $\langle r_{com,z} \rangle \sim (N-1)^{1/3}$.

as in eq 5.19, $\alpha \approx \langle r_{com,z}/r_{com,x} \rangle$ which is equal to the ratio between lift and drag force magnitudes, F_L/F_D. Assuming Stokes's law for the drag force, $F_D^* \approx 6\pi\eta R^* \dot{\gamma}^* \langle r_{com,z} \rangle^*$, where η is the viscosity, the scaling of $\left(R_G^2\right)^*$ and $\langle r_{com,z} \rangle^*$ in Figure 5.12b,c with the monomer number, given as $\left(R_G^2\right)^* \sim (N-1)^2$ and $\langle r_{com,z} \rangle^* \sim (N-1)^{1/3}$, and the dependence $\dot{\gamma}^* \sim (N-1)^{-1/3}$ in eq 5.12 allow us to deduce the dependence of the drag force at the critical shear rate on the chain length as

$$F_D^* \sim (N-1). \tag{5.20}$$

This relation arises due to the fact that the dependences of $\dot{\gamma}^*$ and $\langle r_{com,z} \rangle^*$ on $N-1$ cancel each other. When we combine the results for the scaling relations of F_D^* and α^* in eqs 5.19 and 5.20, we find for the grafted scenario that the lift force at the critical shear rate is proportional to the mean z-position of the center of mass,

$$F_L^* \approx (\alpha^* \; F_D^*) \sim (N-1)^{1/3}. \tag{5.21}$$

A similar result has previously been derived by Sing and Alexander-Katz for the strong stretching limit [280] and apparently also is a good approximation at the critical shear rate. Note that the approximation becomes better for an increasing number of beads because the angle α^* decreases and we move closer to the strong stretching limit.

5.3.4 Comparison of Mean and Maximal Tensile Forces at Critical Shear Rate

Finally, we analyse the dependence of the tensile force profile in terms of its maximum and the mean value at the critical shear rate, defined as

$$f_{max}^* = \max_{i \in \{1,\ldots,N-1\}} (f_i^*)\,, \tag{5.22}$$

$$f^*_{\text{mean}} = \frac{1}{N} \sum_{i=1}^{N-1} f^*_i. \tag{5.23}$$

Note that these quantities and their dependence on the number of monomers are relevant in relation to mechanosensitive folding and unfolding of VWF domains.[68,268–271] In Figure 5.13a, we show the mean positions of the beads for the grafted scenario at the critical shear rate. We analyse the corresponding tensile force profiles, shown in Figure 5.13b, in terms of their maximum values, shown in Figure 5.13c, and in terms of their mean values, shown in Figure 5.13d. The numerical results for the maximum and mean tensile forces for the grafted scenario at the critical shear rate suggest the following heuristic dependencies on the number of monomers:

$$f^*_{\text{max}} \sim (\dot{\gamma}^*)^{-1} \sim (N-1)^{1/3} \quad \text{(grafted)}, \tag{5.24}$$

$$f^*_{\text{mean}} \sim (\dot{\gamma}^*)^{-1/3} \sim (N-1)^{1/9} \quad \text{(grafted)}. \tag{5.25}$$

The small range of monomer numbers considered for the scaling law shown in Figure 5.13d limits the precision with which we are able to determine the scaling exponent. Hence, we would argue that the exponent we use in the heuristic law in eq 5.25 is merely meant to be a satisfactory fit to the existing data. We find that for the grafted scenario at the critical shear rate, f^*_{max}, which corresponds to the tensile force acting on the grafted monomer, is directly proportional to the radius of the collapsed chain while the mean tensile force becomes almost independent of the chain length, even though the drag force increases. The simulation results in Figure 5.14 for the tensile force profiles show that the maximum and the mean tensile forces are almost identical. Heuristically, we find for $N \geq 20$ the relation

$$f^*_{\text{max/mean}} \sim (\dot{\gamma}^*)^{3/2} \sim (N-1)^{1/2} \quad \text{(non-grafted)}, \tag{5.26}$$

which is shown to describe the simulation results well in Figure 5.14.

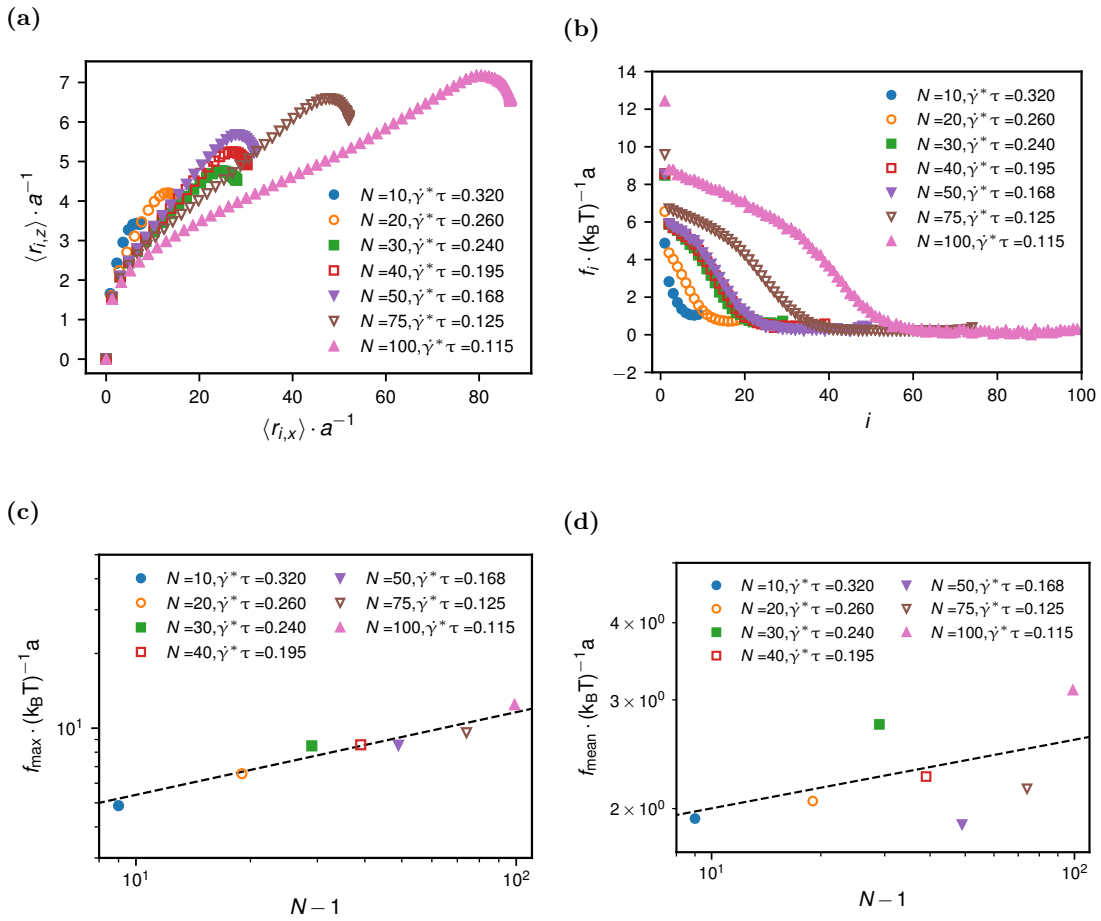

Figure 5.13: Grafted scenario at the critical shear rate $\dot{\gamma}^*$: Subfigure (**a**) shows the mean monomer positions $\langle x\rangle(i)$ and $\langle z\rangle(i)$. The resulting tensile force profiles are depicted in subfigure (**b**). Subfigures (**c**,**d**) show how the maximum and the mean of the tensile force profiles scale with the monomer number $N-1$. The simulation results suggest heuristic scaling laws, indicated as dashed lines, which are given in eqs 5.24 and 5.25.

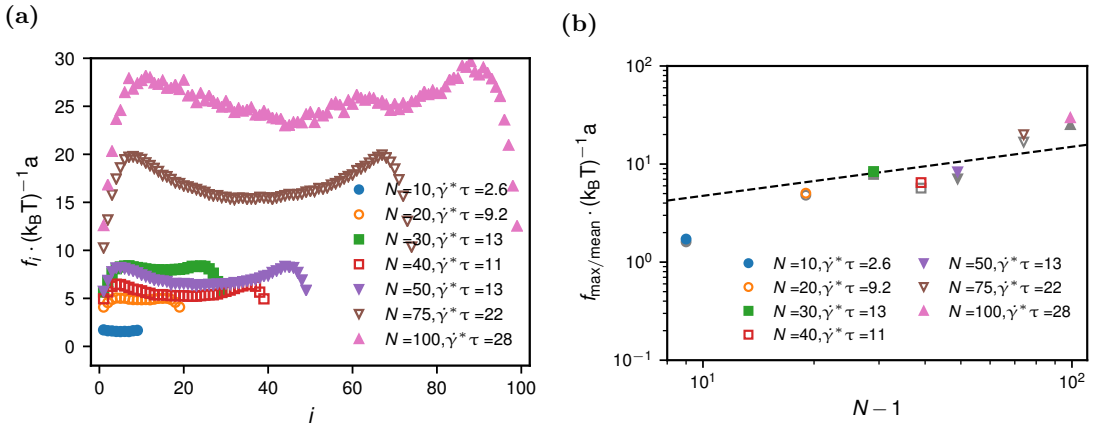

Figure 5.14: Non-grafted scenario at the critical shear rate $\dot{\gamma}^*$: Subfigure (**a**) shows the tensile force profiles at the critical shear rates for different monomer numbers. In subfigure (**b**) we show the maximum of the tensile force profiles in colour and the mean of the tensile force profiles in grey. For the non-grafted case, the maximum and mean tensile forces are very similar and are described by the same heuristic scaling given by eq 5.26.

5.4 Conclusions

The grafted scenario for collapsed polymers under the influence of a constant linear shear flow exhibits very different unfolding behaviour compared to the scenario where the polymer is detached but in the vicinity of the vessel wall. Quantitatively, we find that the critical shear rate in the grafted case is inversely proportional to the size of the collapsed polymer. In comparison, we find the critical shear rate for the non-grafted scenario to increase proportionally with the size of the collapsed polymer which is in accordance to previous studies.[74,75,260] The general understanding is that shear activation of VWF is a key factor for the ability to bind blood platelets and thus to initiate the clot formation process and that the activation of VWF is accompanied by binding to exposed sub-endothelial collagen.[68,75,83,251] Hence, the two investigated scenarios are relevant cases to understand VWF's involvement in coagulation especially when discussing possible cooperative effects. Recent studies have investigated the role of single domains of the VWF dimer in the activation process and their ability to bind to certain types of collagen.[68,83,265] Because there is only a preliminary understanding of the binding process and energies, cooperative effects are not at the focus of present VWF studies. However, when we put in physiological relevant parameters for the size of VWF ($N = 50$ and $a = 73\,\mathrm{nm}$[75,81]), we find that the critical shear changes from $\dot{\gamma}^*_{\mathrm{non-grafted}} = 11{,}000$ Hz for the non-grafted scenario to $\dot{\gamma}^*_{\mathrm{grafted}} = 140\,\mathrm{Hz}$ in the grafted scenario, where we use $\eta = 0.6913\,\mathrm{mPa\,s}$ for the dynamic viscosity of water at 37 °C.[281] By this consideration, we expect the attachment of VWF at the site of an injured vessel to considerably promote unfolding and to possibly lead to a cascade of activations of different sub-domains. While the shape of the tensile force profile significantly differs depending on the scenario, we show that the maximum of the tensile force profile at the critical shear rate is rather similar in both scenarios. By comparing the tensile force profiles for shear rates in the vicinity of the critical shear, we are able to illustrate the mechanisms responsible for unfolding in the two different scenarios. We reproduce the previously proposed protrusion mechanism[75,81,260] that governs the turn-over for the non-grafted scenario. We show that for the grafted scenario the mechanism is dominated by the tensile force acting on the grafted monomer and that unfolding of a subsection of the polymer, the size of which depends on the shear rate, characterizes the unfolding mechanism. Simulated tensile forces can be related to rupture forces of VWF domains from AFM measurements to estimate folding and unfolding times when we use transition rate theories.[68,265,268–271] Our analysis of the center of mass position dependence on the shear rate reveals the approximate angles at which the grafted polymer reaches into the solvent and allows for the determination of the relation between acting drag and lift forces. The reason for the opposite dependence of the critical shear rate on the size of the collapsed polymer originates in the distinctively different mechanisms that initiate unfolding. In the non-grafted scenario, protrusions have to build up and due to the rotational motion of the chain become wrapped around the
chain.[74,75,260] Thus, the unfolding mechanism has been described as a nucleation pro-

cess that depends on the sufficiently large size of the protrusions. [74,81,260] For the grafted scenario the chain cannot rotate since the first monomer is anchored. Hence, protrusions do not have to spontaneously occur in this scenario but are inherently present at all times for sufficiently large shear rates. Future work could investigate cooperative effects that might arise from a transition of the non-grafted scenario of VWF to the grafted scenario.

Chapter 6

Summary and Outlook

In this thesis, several research topics relevant to biophysics and medicine like the force-stretching relation of polypeptides, the efficiency of signaling modes in proteins or the unfolding mechanism of collapsed polymeric chains in linear shear flow are elucidated from a physical point of view based on computational simulation results. Quantitative model predictions are deduced. For each study, the model is either based on experimental data or on a theoretical framework which is supported by the comparison of the model predictions with available experimental results. This provides a reference for the accuracy of the models.
In chapter 2, five different homopeptides polyglycine, polyalanine, polyasparagine, poly(glutamic acid), and polylysine are simulated employing all-atom molecular dynamics computations including explicit water. The MD simulation results are compared with the inhomogeneous partially freely rotating chain (iPFRC) model which accounts for the fixed dihedral angle due to the restricted peptide bond configuration. The accuracy of the model is verified by Ramachandran plots of the dihedral angle which characterizes rotations around the peptide bond. The influence of side-chain interactions on the elongation of polypeptides is reviewed. The results shine a light on the fact that those interactions impact the stretching moduli and lead to a significantly different high-force stretching responses between polyglycine, which has no side-chains, and homopeptides with present side-chains. In addition to the stretching moduli, polymer characteristics like the Kuhn length, the equilibrium contour length and the iPFRC model-specific parameter c, which impacts the high-force stretching response, are deduced from the simulation results. We show how to implement the force-dependent contour length stretching into the iPFRC model. The resulting model predictions of the force-extension relation for homopeptides are compared with experimental single molecule force spectroscopy results based on atomic force spectroscopy from Hugel, et al.[107] The comparison yields very good agreement over the entire force-regime without additional freely adjustable parameters. However, the experimental data show a noticeable deviation from the model prediction in the mid-force regime around 200 pN to 400 pN. We cannot link this discrepancy to any underlying physical mechanism.

Further experimental studies in the future could help to resolve this issue. Analysis of the thermodynamic properties by decomposition of the stretching free energy into energetic and entropic contributions shows that the stretching responses of homopeptides are mostly entropic and that water bridges do not occur frequently and thus are unlikely to have the same stabilizing effect that we found for PEG. [48,282]
In chapter 3, MD simulation results of a coiled coil motif for signal transduction in proteins are presented. The system consists of two parallel α-helices in water and two counter-ions as the solvent. Based on linear response theory, the fluctuations of relative motions are deduced from simulations and analyzed to yield response functions that quantify the response of such a relative motion to a periodic force applied to one side of one the two helices. The analyzed relative motions based on simulation results are shift, splay and twist. By definition of a "virtual" periodic force on the opposing signaling site of the coiled coil system, such that the signaling response is suppressed, one can define a frequency-dependent force-transmission function. This force-transmission function quantifies the effectiveness of either shift, splay, or twist to transfer a signal from one end of the coiled coil system to the other as a function of the frequency of the signal itself. Results for the particular coiled coil linker Jα, which is designed based on the light-oxygen-voltage (LOV) histidine kinase YF1, [72,73] suggest that in the frequency range between 100 kHz and 100 MHz the twist mode is double as effective as the shift mode and that the splay mode is only one-tenth as effective as the shift mode. In the frequency range between 1 GHz and 10 GHz, a crossover of the transmission functions of twist and shift appear due to the twist mode becoming much less effective to a point where at 10 GHz it is not significantly more effective for signaling than splay. For frequencies above 10 GHz, the noise of the resulting data coerces the report of no significant difference between the effectiveness of the three modes. Analytic fitting of the response functions and the consequent extraction of correlation parameters suggest that the twist mode could become relevant again towards the far-infrared regime from 100 GHz to 1000 GHz, which reportedly can be attributed to vibrations of weaker intermolecular interactions (e.g., hydrogen bonds). [283–287] Interestingly, based on electron paramagnetic resonance spectroscopy and X-ray solution scattering, the light-induced conformational changes within the LOV sensor have been reported as a splay motion. [73] This could point to either the LOV sensor domain to have a significant impact on the signaling motion pathway or a cooperative effect of several relative motions.
In chapter 4, experimental and simulation results of PEG and PNiPAM are used to reveal temperature-dependent cooperative effects between the solvent and the polymer. We show that these cooperative effects lead to an opposing temperature stretching response of PEG and PNiPAM in water. For PNiPAM, the stretching force increases with increasing temperature, whereas for PEG we obtain a decrease in the stretching force for increasing temperature. The cooperative effect for PEG is linked to the stabilization of the gauche state through water bridges. This effect is quantified by extraction of the fraction of trans states of PEG as a function of the stretching force. The steep non-linear increase of this fraction at roughly 100 pN is temperature-dependent and coincides with the difference in force-extension relation. The slightly shorter gauche

state explains shorter extensions while high fractions of trans states yield longer extensions for the same applied stretching force.[48] The presence of cooperative effects for PNiPAM in water is displayed by the fact that the single molecule force spectroscopy measurements provide no significant change of the shape of the recorded force-extension curves around the lower critical solution temperature (LCST).[282] The analysis of the thermodynamic properties by decomposition of the stretching free energy into energetic and entropic contributions gives evidence for the strong energetic solvation effects especially in the intermediate to large force regime. Comparison of the force-extension curves with predictions for the freely jointed and the worm-like chain model based on parameters obtained from the MD simulations show the discrepancy of descriptions by these models that take only the entropic or energetic properties of the chain itself into account. This demonstrates the importance of validating the applicability of a polymer model for the fit of the force-extension curve. In disregarding this step, one can yield reasonable resulting fits, but the obtained parameters might entail no physical meaning. Our experimental and simulation results show that standard models like the freely-jointed and the worm-like chain model are not sufficient to predict the temperature dependence of the stretching behavior and that the temperature dependence is very much determined by hydration or dehydration of the polymer. An improved understanding of the temperature-dependent stretching behavior of polymers will help to advance the application of thermoresponsive polymers, which could be especially useful in medicine.[288–291]

In chapter 5, collapsed polymers under constant linear shear flow are studied for two relevant scenarios for the shear activation of von Willebrand factor, a large glycoprotein involved in primary hemostasis. In the first scenario, the collapsed polymer is attached to the vessel wall on one side. The other scenario describes the collapsed polymer in a detached scenario in the vicinity of the vessel wall. The critical shear rate is obtained for both scenarios, where the polymer changes from a collapsed to a coiled state. We show that the critical shear rate in the grafted case is inversely proportional to the size of the collapsed polymer. In comparison, we find the critical shear rate for the non-grafted scenario to increase proportionally with the size of the collapsed polymer. From the finding that the grafted scenario significantly lowers the critical shear rate, we expect the attachment of VWF at the site of an injured vessel to considerably promote unfolding and to possibly lead to a cascade of activations of different sub-domains. We determine the mechanical response of the polymer by obtaining the tensile-force profiles as well as the angle, at which the attached polymer reaches into the stream, depending on the shear rate. Even though the tensile-force profiles differ for the grafted and non-grafted scenario, we find that the maximum of the tensile force profile at the critical shear rate is rather similar in both scenarios. The different unfolding mechanisms for the two scenarios are discussed. For the non-grafted scenario, the previously proposed protrusion mechanism is reproduced.[75,81,260] For the grafted scenario, the unfolding mechanism is dominated by the tensile force acting on the grafted monomer. We believe that the elucidation of these two mechanisms could lead to the investigation of cooperative effects of the two mechanisms, which are very likely to both occur during

the activation of von Willebrand factor.[292–295]

In summary, we demonstrate the distinct influences of real polymer properties as opposed to ideal polymer assumptions for the stretching of the contour length depending on the applied stretching force or the hydration and dehydration effects, which render commonly used polymer models insufficient in their description of the force-extension relation for many water-soluble polymers.[282,296] We give insights into the thermodynamic properties of stretched polymers in explicit water by decomposition of the stretching free energy into energetic and entropic contributions. This allows for the distinction of real polymers from polymers that can be described as purely entropic (freely jointed) or by a fixed rigidity (worm-like).[282,296] Mechanical relative motions in two parallel α-helices are modeled to give further insights into possible pathways of signaling in protein structures.[145,154,155,297] Finally, the response of attached and detached polymers under constant linear shear flow conditions is investigated to provide a broader understanding of the role of von Willebrand factor in initiating the blood coagulation process.[76–78,298]

This work contributes to the expansion of the theoretical framework which describes the response of polymers to external forces. We provide quantitative models which can act as references for the improvement of mechano- and thermoresponsive materials.

Appendix A

Force Response of Polypeptide Chains from Water-Explicit MD Simulations

A.1 Stretching Response in Salt Solutions

The single-molecule AFM peptide stretching data by Hugel et al.[107] were obtained in phosphate-buffered saline (PBS) with additional 500 mmol/L sodium chloride. To check for possible effects of salt on the stretching response of polypeptides, we performed additional stretching simulations in water with sodium and chloride at a concentration of 500 mmol/L. Note that for the charged peptides an additional number of counter ions is present in order to neutralize the peptide charge. From the results shown in Figure A.1 we can conclude that the addition of sodium chloride at a concentration of 500 mmol/L has no significant effect on the stretching response of the polypeptides in the force range we investigate in our simulations.

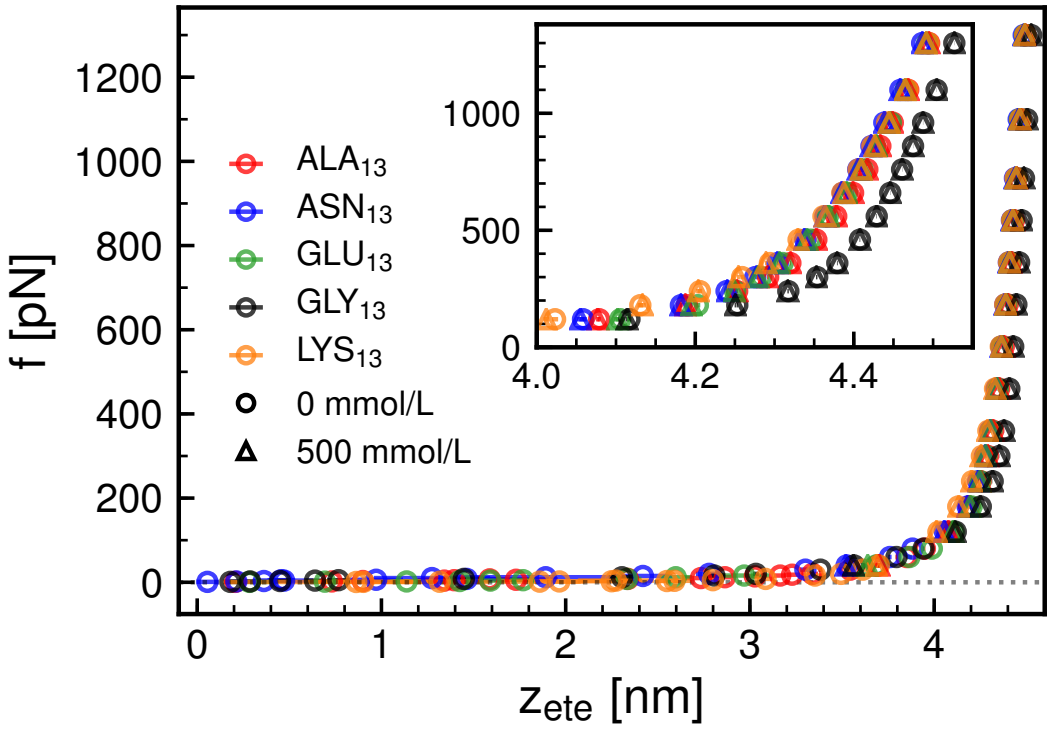

Figure A.1: Comparison of the stretching response from MD simulations for polypeptides at NaCl concentrations of 500 mmol/L (triangles) and for pure water (spheres). Note that in addition 13 counter ions are present in the system for poly-lysine and poly-glutamic acid in order to make the system charge neutral.

A.2 Origin of Different Backbone Stretching Moduli

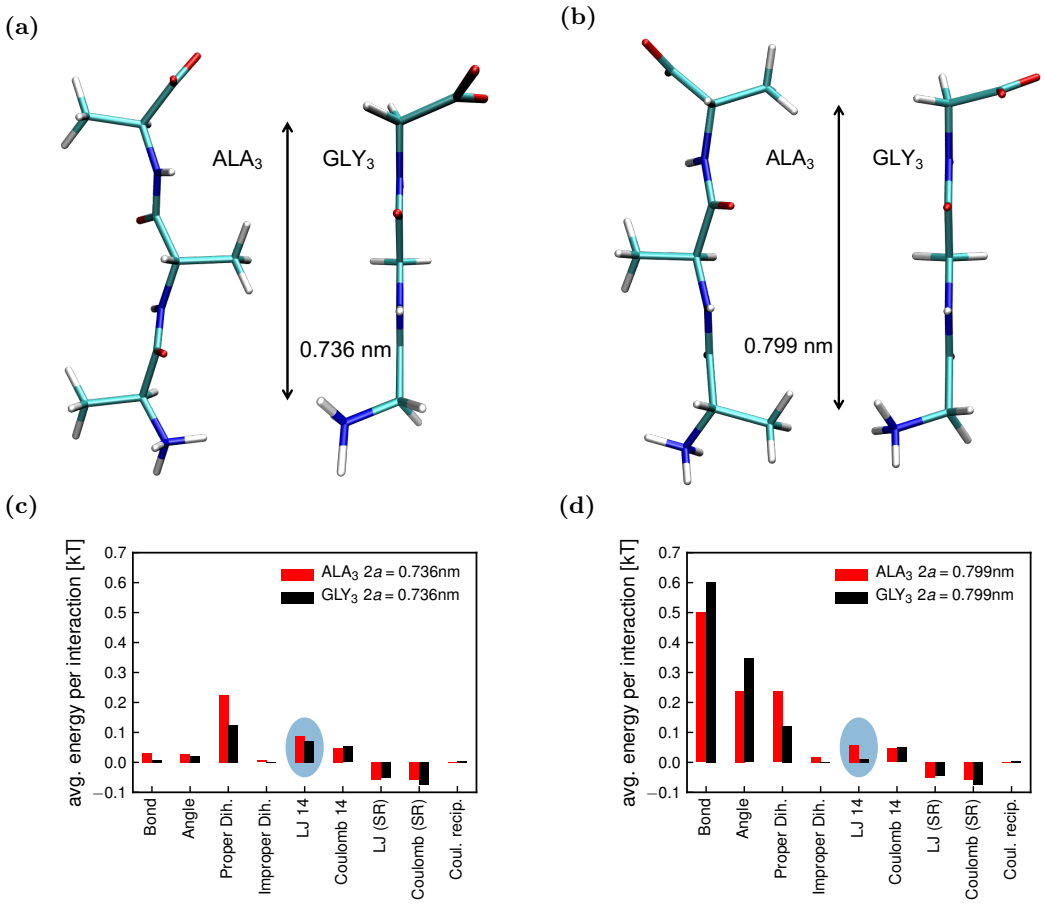

Figure A.2: Comparison of the energetic contributions in the MD simulations of GLY_3 and ALA_3 in vacuum at a fixed distance $2a = 0.736\,\text{nm}$ (corresponding to the equilibrium value $2a_0$ for glycine) and at a significantly stretched distance $2a = 0.799\,\text{nm}$. Upon stretching, we observe a significant increase of the bond length and bond angle energies. For glycine we see that the Lennard Jones 1-4 interaction between further neighboring atoms almost vanishes at large stretching. For alanine on the other hand, we see a much less pronounced drop of the Lennard Jones 1-4 interactions, which reflects a much stronger interaction between side-chains and backbone. As can be seen in the snapshots (a) and (b), these interactions prevent a planar conformation of alanine even for the strongly stretched state.

Appendix B

Opposing Temperature Dependence of the Stretching Response of Single PEG and PNiPAM Polymers

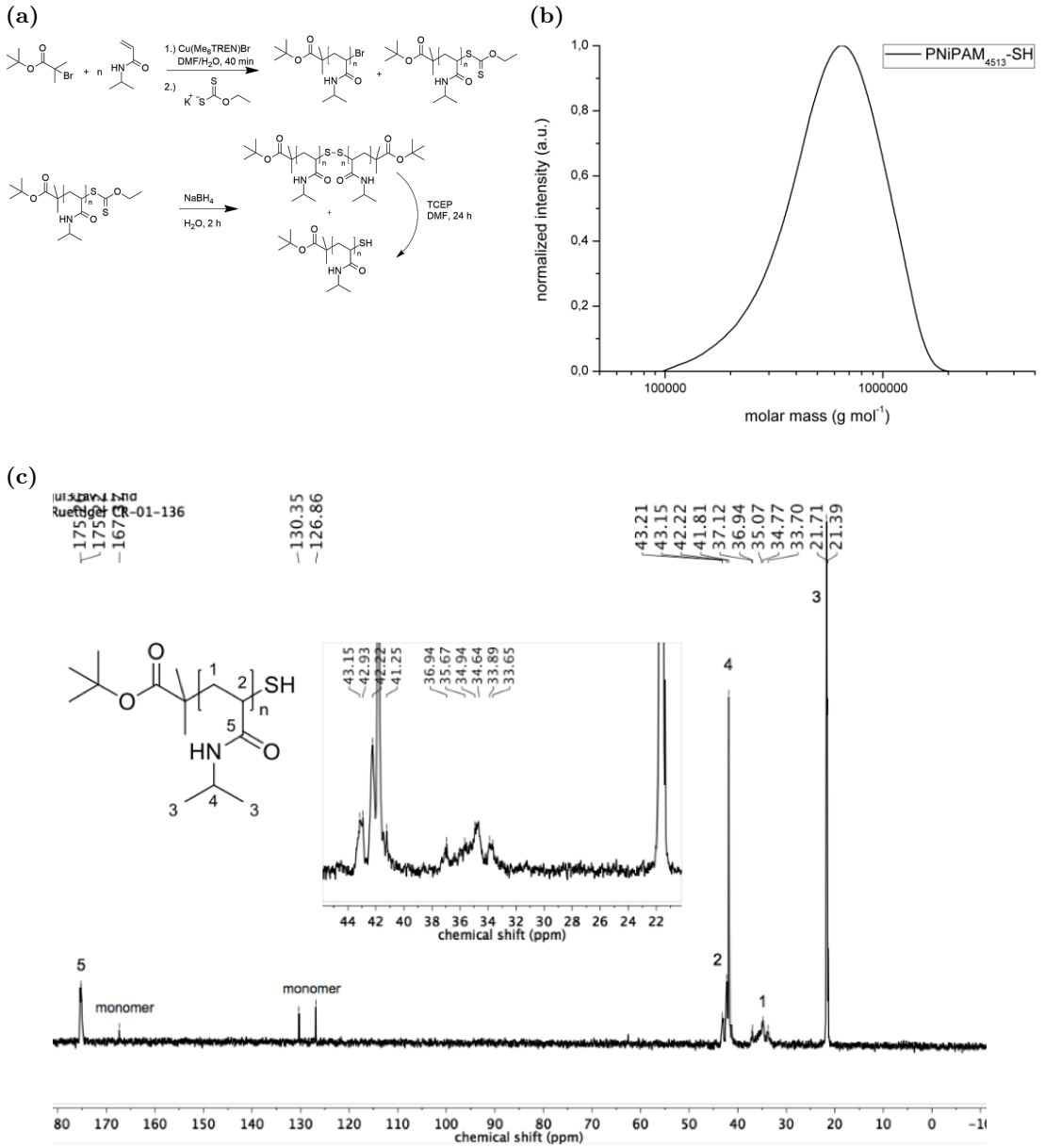

Figure B.1: Synthesis of SH-PNiPAM. (a) The reaction path in modification of the following references.[299,300] (b) Resulting GPC data leading to $M_n = 510\,\mathrm{kDa}$, $Đ = 1.28$. (c) ^{13}C-NMR data (125.8 MHz, D_2O as solvent) of the product with a zoom-in in the region between 22 ppm and 45 ppm, indicating that the SH-PNiPAM is atactic according to Idota et al.[301]

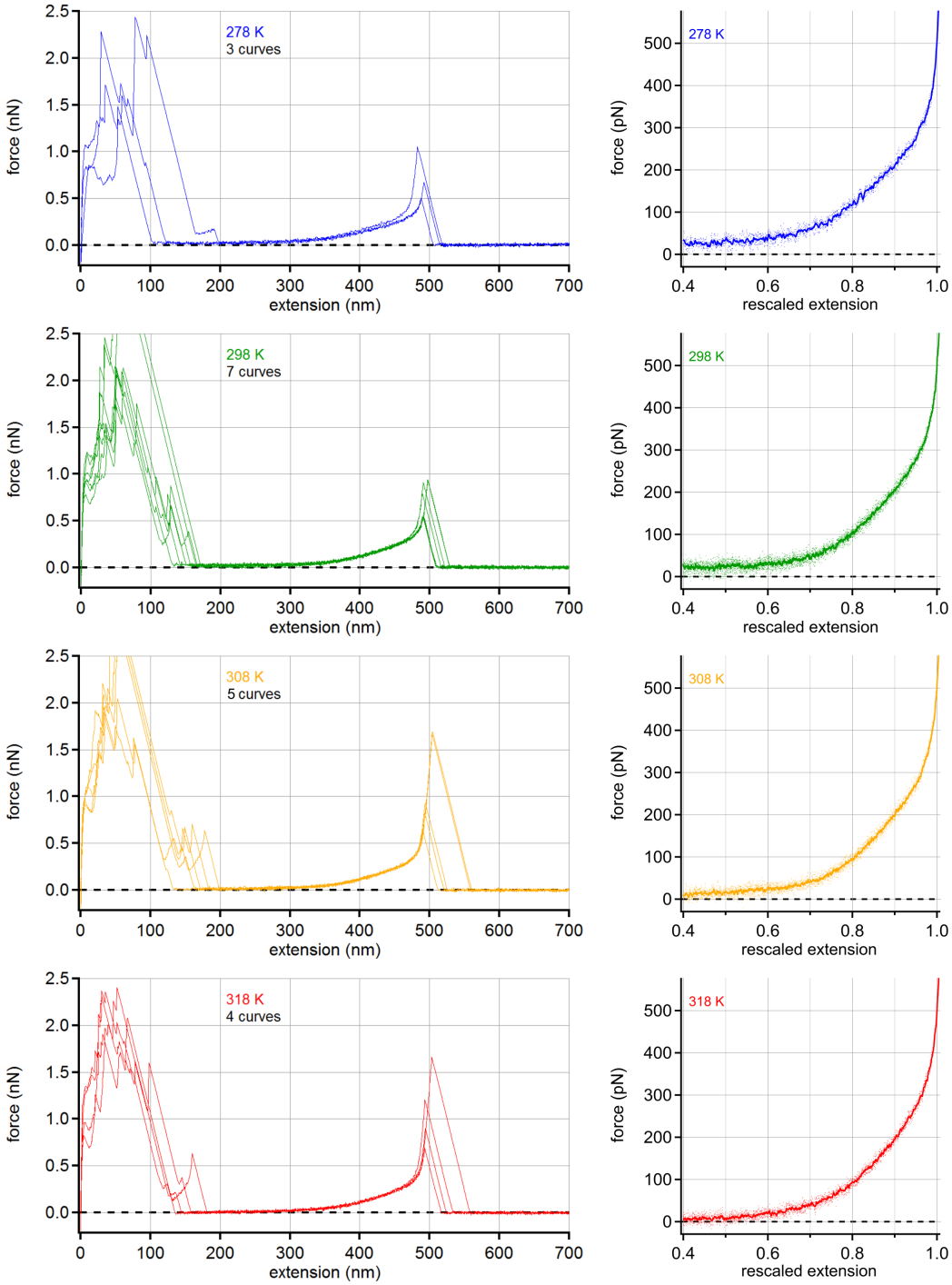

Figure B.2: Experimental force-extension curves and master curves of PEG at different temperatures. For a master curve all traces with rupture events higher than 500 pN were selected (left). The extension of each trace was then rescaled to its extension at 500 pN followed by binomial smoothing with a smoothing parameter of 20 (right). The rescaled curves used to obtain the master curves are given as dots while the master curves are shown as solid lines. The number of forceextension curves used for master curve determination is: 278 K – 3 curves, 298 K – 7 curves, 308 K – 5 curves, 318 K – 4 curves.

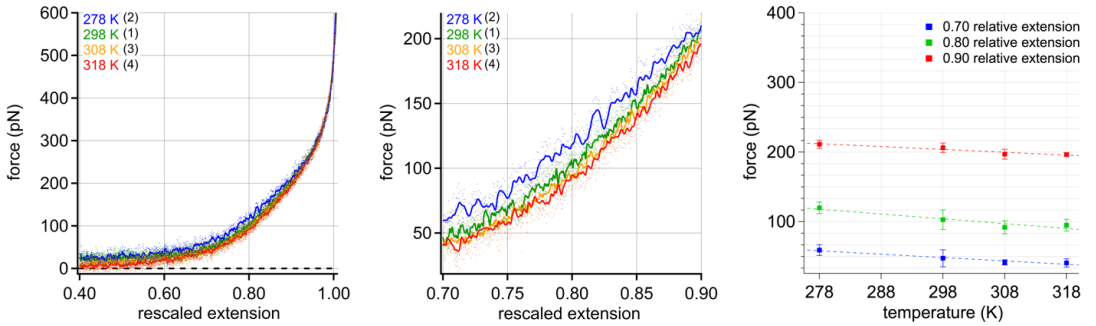

Figure B.3: Master curves for different temperatures obtained experimentally for PEG (left) and zoom-in (middle) corresponding to Figure S2. The rescaled curves used to obtain the master curves are given as dots while the master curves are shown as solid lines. The order of data acquisition is given in brackets, i.e. force-extension curves were first taken at 298 K, then at 278 K, followed by 308 K and 318 K. Furthermore, force-temperature curves for relative extensions of 0.70, 0.80 and 0.90 are shown, respectively (right). The broken lines serve as a guide to the eye and the error bars represent the standard deviation.

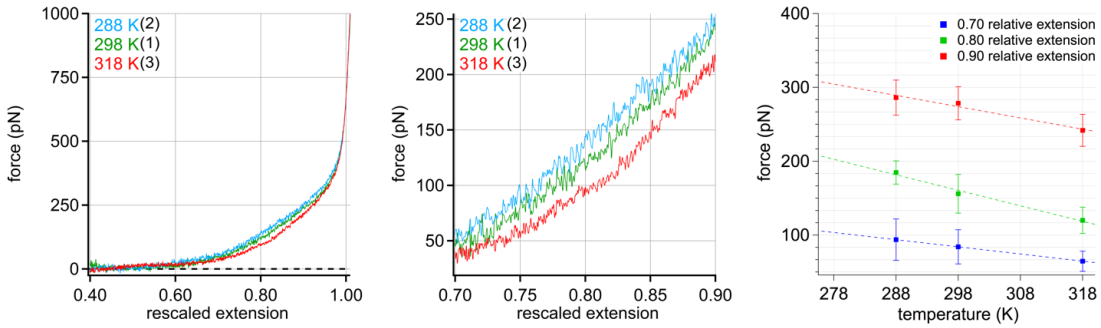

Figure B.4: Master curves for different temperatures for a second experimental PEG data set (left) and zoom-in (middle). The number of force-extension curves used for the master curve determination is: 288 K – 7 curves, 298 K – 7 curves, 318 K – 9 curves. The order of data acquisition is given in brackets. Furthermore, force-temperature curves for relative extensions of 0.70, 0.80 and 0.90 are shown, respectively (right). The broken lines serve as a guide to the eye and the error bars represent the standard deviation.

Figure B.5: Experimental force-extension curves and master curves of PNiPAM at different temperatures. For a master curve all traces with rupture events higher than 500 pN were selected (left). The extension of each trace was then rescaled to its extension at 500 pN followed by binomial smoothing with a smoothing parameter of 20 (right). The rescaled curves used to obtain the master curves are given as dots while the master curves are shown as solid lines. The number of force-extension curves used for master curve determination is: 278 K – 4 curves, 288 K – 3 curves, 298 K – 3 curves, 308 K – 4 curves, 318 K – 3 curves, 328 K – 3 curves .

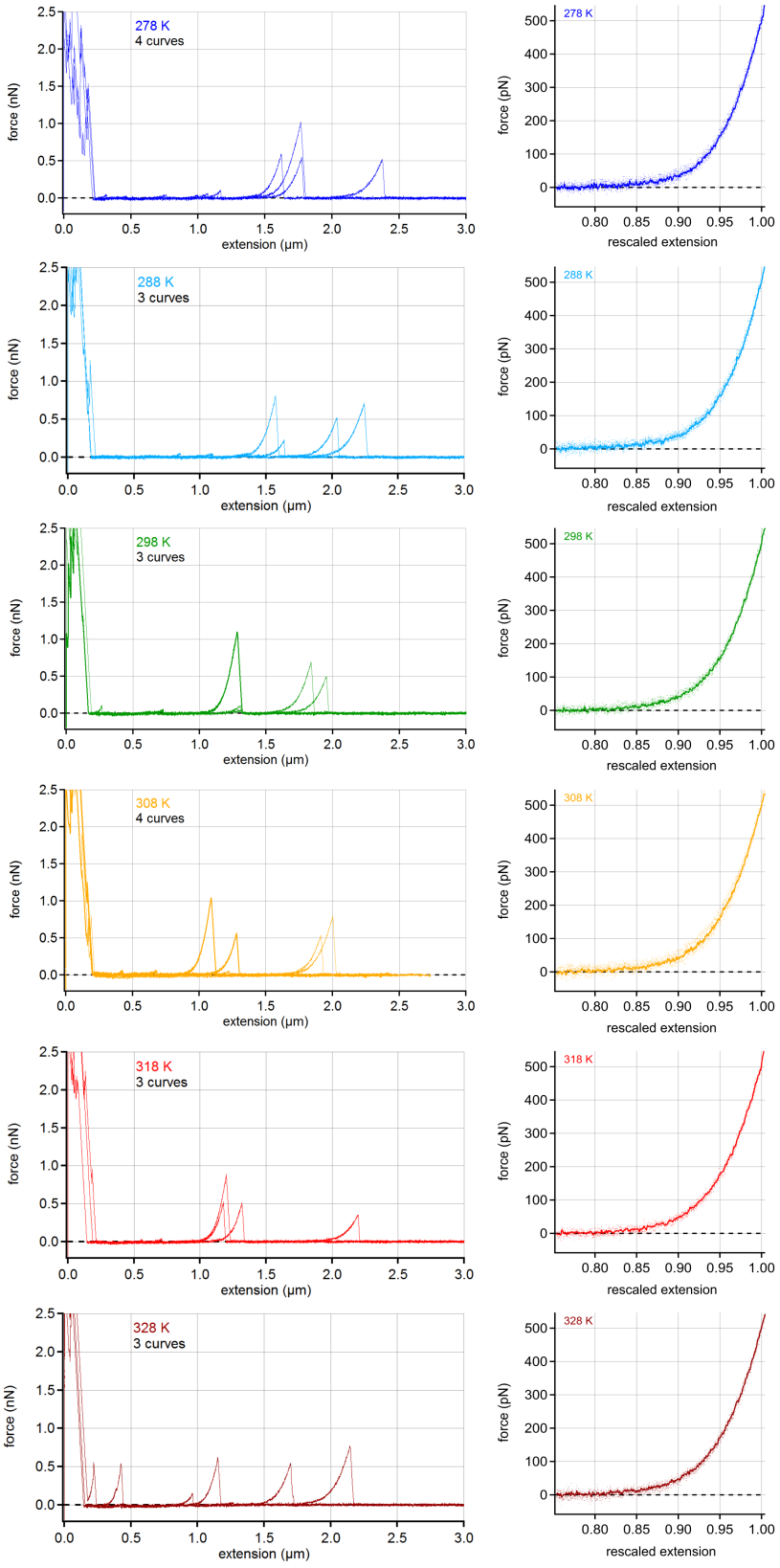

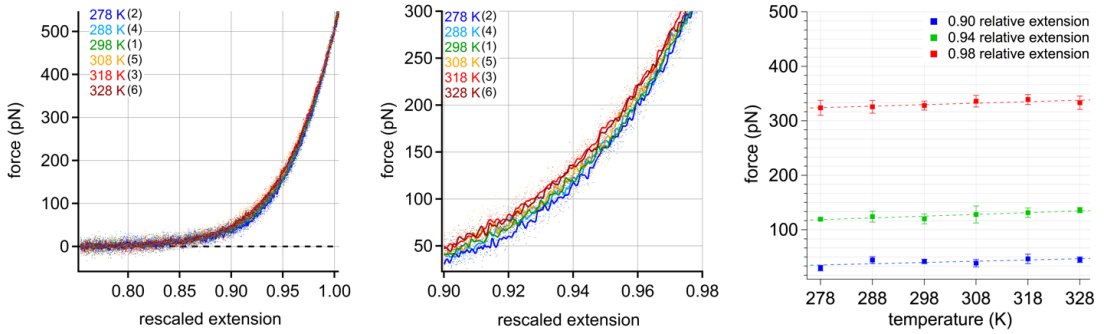

Figure B.6: Master curves for different temperatures obtained experimentally for PNiPAM (left) and zoom-in (middle) corresponding to Figure B.5. The rescaled curves used to obtain master curves are given as dots while the master curves are shown as solid lines. The order of data acquisition is given in brackets. Furthermore, force-temperature curves for relative extensions of 0.90, 0.94 and 0.98 are shown, respectively (right). The broken lines serve as a guide to the eye and the error bars represent the standard deviation.

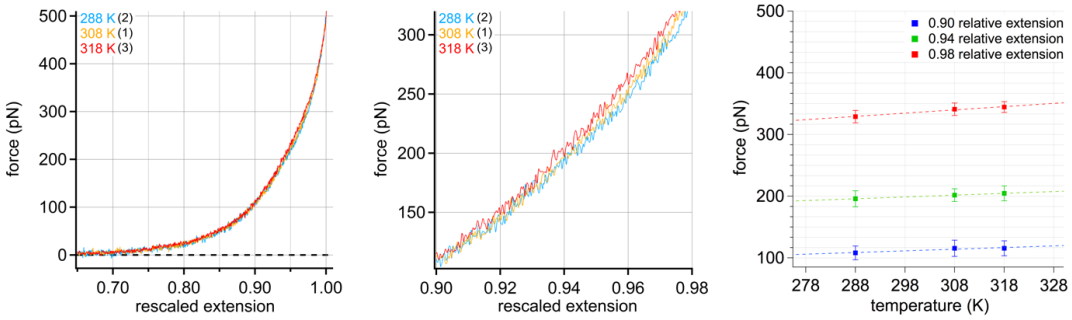

Figure B.7: Master curves for different temperatures for a second experimental PNiPAM data set (left) and zoom-in (middle). The smaller effect compared to Figures 2 and S6 can be explained by the smaller temperature range of 40 K and the different lengths of the measured polymers. The first data set shows contour lengths of about 1.0 to 2.5 µm which is approx. two to four times longer than the contour lengths of the second data set. The number of force-extension curves used for rescaling is: 288 K – 18 curves, 308 K – 18 curves, 318 K – 16 curves. The order of data acquisition is given in brackets. Furthermore, force-temperature curves for relative extensions of 0.90, 0.94 and 0.98 are shown, respectively (right). The broken lines serve as a guide to the eye and the error bars represent the standard deviation.

B.1 Polymer Elasticity Models

To further investigate the elasticity of the polymers, the MD simulation data of PEG was fitted with the linear forceextension relation (linear response theory) in the limit of $f\,b \ll k_B T$:[100,302,303]

$$\frac{z_e te}{L_C} \approx \frac{f\,b}{3k_B T} \quad . \tag{B.1}$$

Temperature (K)	Kuhn length b (nm)
250	0.74 ± 0.02
300	0.75 ± 0.05
350	0.73 ± 0.03
400	0.76 ± 0.02

Table B.1: Kuhn length fit parameter obtained by fitting the low force – extension (1 pN to 4 pN) range of MD simulation data for PEG using eq B.1. No significant change of the Kuhn length over a temperature range of 150 K could be found.

This allows for the determination of the Kuhn length b by fitting the force-extension data in the range of 1 to 4 pN. The fitting of the slope has been done using the conventional method of weighting each point by its squared error, which was obtained by block averaging.[304] The course of the Kuhn length suggests no significant change over a wide range of temperatures (Table B.1). Therefore, we use the mean of the simulated Kuhn lengths, namely b = 0.75 nm to fit the experimental data.

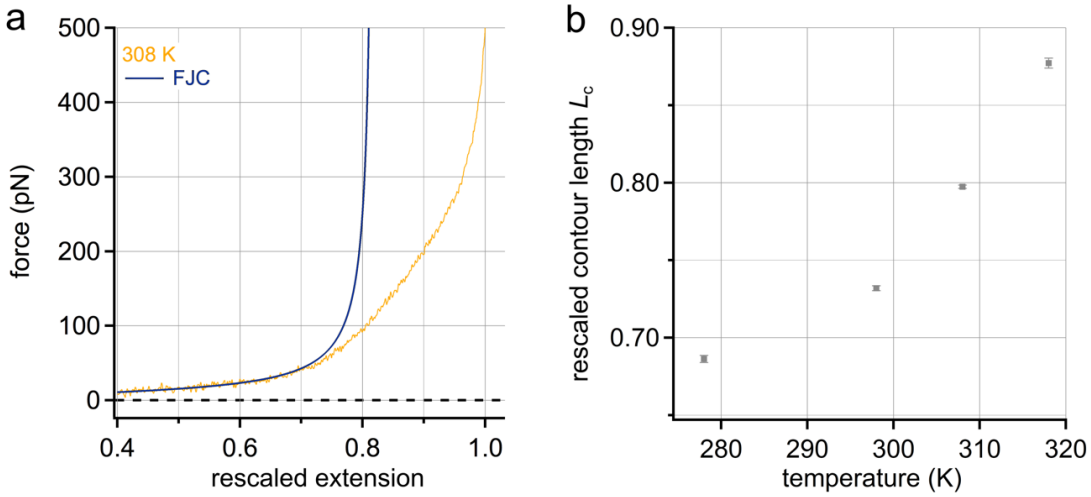

Figure B.8: (a) Master curve of PEG at 308 K with an exemplary FJC fit (blue line, eq B.1. The parameter for the Kuhn length is $b = 0.75$ nm (see Table B.1) and the fit range was chosen between 0 and 80 pN. (b) The resulting rescaled contour length Lc (with respect to the extension at a force of 500 pN) for each master curve is plotted against the respective temperature. The FJC model fits the experimental traces very well at low and intermediate forces. For higher forces the bond elasticity has to be taken into account.[48,100,304,305] Furthermore, fitting the force-extension curves of PEG for different temperatures using the FJC model leads to clear increase of the contour length with increasing temperature. This is consistent with the change of the fraction of monomers that are in the trans conformation, as discussed in the main text.

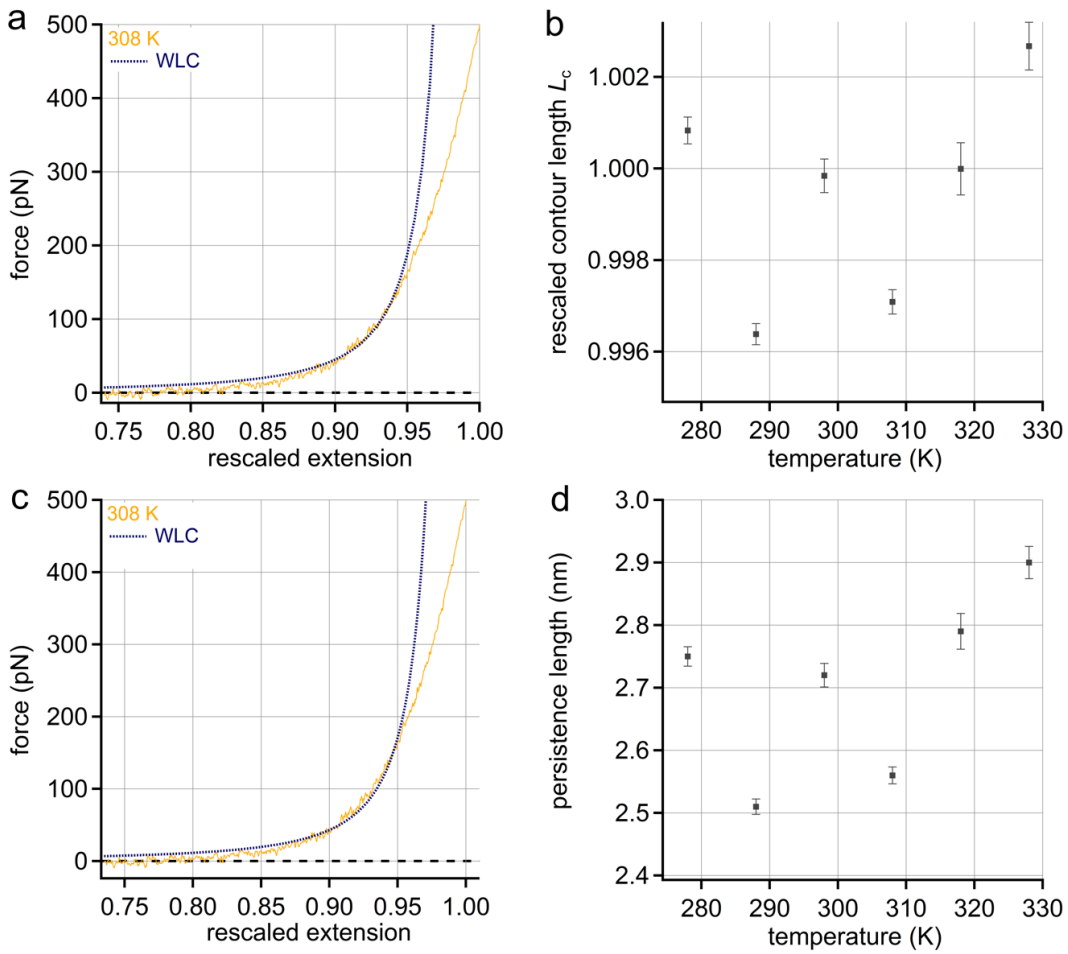

Figure B.9: (a) Master curve of PNiPAM at 308 K with an exemplary WLC fit (dashed blue line, eq. 2). The parameter for the persistence length was kept constant at 2.5 nm 10 and the fit range was chosen between 0 and 80 pN. (b) The resulting rescaled contour length Lc (with respect to the extension at a force of 500 pN) for each master curve is plotted against the respective temperature. Keeping the persistence length constant there is very little variation for the rescaled contour length for different temperatures. (c) Master curve of PNiPAM at 308 K with an exemplary WLC fit (dashed blue line). The parameter for the contour length was kept constant at 0.9995 nm (average value of data points shown in b). (d) The resulting persistence length for each master curve is plotted against the respective temperature. Here we keep the rescaled contour length constant (0.9995nm) for each of the WLC fits and obtain the respective persistence lengths for the different temperatures. In summary, the temperature-dependent stretching response of PNiPAM can neither be clearly assigned to the contour length nor to the persistence length if the WLC model is applied.

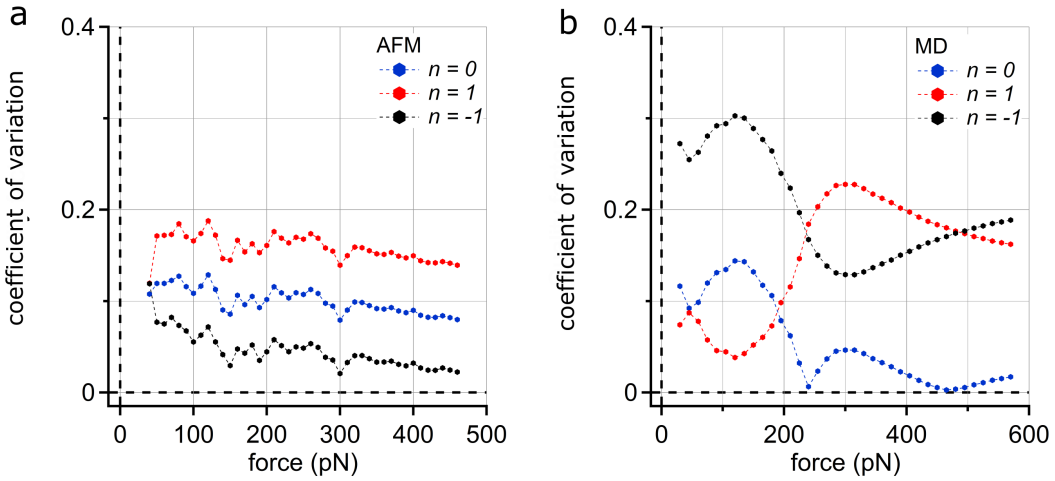

Figure B.10: Coefficient of variation vs force for the PEG data given in Figure 4.4 for (a) AFM experiments and (b) MD simulations. The coefficient of variation indicates the standard deviation over the mean value and is presented for: the stretching free energy F per $L0$ (the extension at a force of 500 pN) which represents the case of $n = 0$, the stretching free energy F per $L0$ divided by k_BT ($n = 1$) and the stretching free energy F per $L0$ divided by k_BT^{-1} ($n = -1$). For experimental data the coefficient of variation was determined in steps of 10 pN while for the MD simulations each data point was used. The lines between the points are a guide to the eye

Figure B.11: Coefficient of variation vs force for the PNiPAM data given in Figure 4.6 for (a) AFM experiments and (b) MD simulations. The coefficient of variation indicates the standard deviation over the mean value and is presented for: the stretching free energy F per $L0$ 0 (the extension at a force of 500 pN) which represents the case of $n = 0$, the stretching free energy F per $L0$ divided by k_BT ($n = 1$) and the stretching free energy F per $L0$ divided by $k_BT^{1/3}$ ($n = 1/3$). For experimental data the coefficient of variation was determined in steps of 10 pN while for the MD simulations each data point was used. The lines between the points are a guide to the eye.

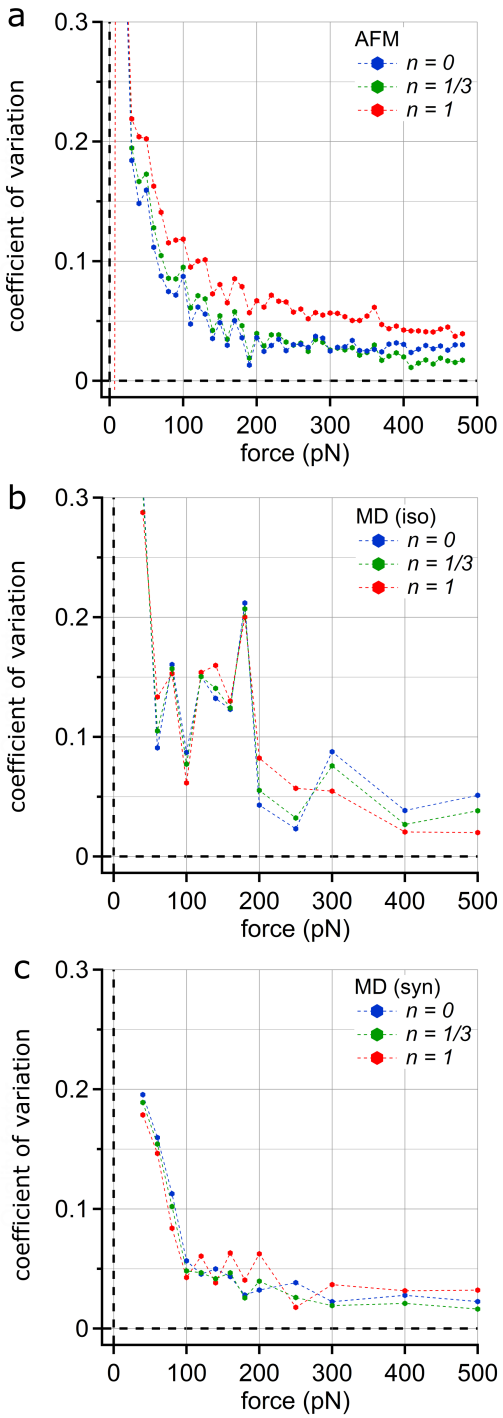

Appendix C

Hydrodynamic Shear Effects on Grafted and Non-Grafted Collapsed Polymers

C.1 Hydrodynamic Mobility Tensors

Let us quickly motivate our over damped Langevin equation by sketching how we arrive at the formula given in the main text,

$$\frac{\mathbf{r}_i(t+\Delta t)-\mathbf{r}_i(t)}{\Delta t} = \mu_0^{-1}\boldsymbol{\mu}_{\mathbf{ii}}\,\dot{\boldsymbol{\gamma}}\,\mathbf{r}_i(t) - \sum_{j=1}^{N}\boldsymbol{\mu}_{ij}\cdot\left[\nabla_{\mathbf{r}_j(t)}U(\mathbf{r}_1,...,\mathbf{r}_N)\right] + \mathbf{v}_i^{\text{correction}}(t) + \boldsymbol{\xi}_i(t). \tag{C.1}$$

The first term is the drag force introduced by the background flow field, $\mathbf{v}_\infty(z)$, without any disturbances. The velocity of the flow field is assumed to depend linearly on z as we want to describe a linear shear flow in x direction in vicinity of a no-slip boundary. The shear tensor is given as

$$\dot{\boldsymbol{\gamma}} = \begin{pmatrix} 0 & 0 & \dot{\gamma} \\ 0 & 0 & 0 \\ 0 & 0 & 0 \end{pmatrix} \tag{C.2}$$

The mobility tensor depending on the situation is either given by the Rotne-Prager-Yamakawa tensor (non-grafted)

$$\boldsymbol{\mu}_{ij} = \boldsymbol{\mu}^{\text{RPY}}\left(\boldsymbol{r}_{ij}=\boldsymbol{r}_i-\boldsymbol{r}_j\right) = \begin{cases} \frac{1}{8\pi\eta r_{ij}}\left[\left(1+\frac{2a^2}{3r_{ij}^2}\right)\mathbb{1} + \left(1-\frac{2a^2}{r_{ij}^2}\right)\hat{\mathbf{r}}_{ij}\otimes\hat{\mathbf{r}}_{ij}\right] & \text{if } r_{ij} > 2a \\ \frac{1}{6\pi\eta a}\left[\left(1-\frac{9r_{ij}}{32a}\right)\mathbb{1} + \frac{3r_{ij}}{32a}\hat{\mathbf{r}}_{ij}\otimes\hat{\mathbf{r}}_{ij}\right] & \text{if } r_{ij} \leq 2a \end{cases}, \tag{C.3}$$

or by the Rotne-Prager-Blake tensor (grafted, no-slip at $z=0$)

$$\boldsymbol{\mu}_{ij} = \boldsymbol{\mu}^{\text{RPB}}\left(\boldsymbol{r}_i,\boldsymbol{r}_j\right) = \boldsymbol{\mu}^{\text{RP}}\left(\boldsymbol{r}_i-\boldsymbol{r}_j\right) - \boldsymbol{\mu}^{\text{RP}}\left(\boldsymbol{r}_i-\bar{\boldsymbol{r}}_j\right) + \boldsymbol{\Delta\mu}\left(\boldsymbol{r}_i,\boldsymbol{r}_j\right), \tag{C.4}$$

where $\bar{\boldsymbol{r}}_j = (x_j, y_j, -z_j)^{\mathrm{T}}$ is the mirror image position and he Rotne-Prager tensor used in this definition is given as

$$\boldsymbol{\mu}^{\mathrm{RP}}(\mathbf{r}) = \frac{1}{8\pi\eta r}\left(\mathbb{1} + \hat{\mathbf{r}} \otimes \hat{\mathbf{r}}\right) + \frac{a^2}{12\pi\eta r^3}\left(\mathbb{1} - 3\ \hat{\mathbf{r}} \otimes \hat{\mathbf{r}}\right). \tag{C.5}$$

The modification term arises from the Stokes and source doublets and has the following specific entries, as derived by von Hansen, et al.,[266]

$$\boldsymbol{\Delta\mu}_{\alpha\alpha} = \frac{1}{4\pi\eta}\left[\frac{-z_i z_j}{R^3}\left(1 - 3\frac{R_\alpha^2}{R^2}\right) + \frac{a^2 R_z^2}{R^5}\left(1 - 5\frac{R_\alpha^2}{R^2}\right)\right] \quad , \text{if } \alpha \in \{x, y\}, \tag{C.6}$$

$$\boldsymbol{\Delta\mu}_{zz} = \frac{1}{4\pi\eta}\left[\frac{z_i z_j}{R^3}\left(1 - 3\frac{R_z^2}{R^2}\right) - \frac{a^2 R_z^2}{R^5}\left(3 - 5\frac{R_z^2}{R^2}\right)\right] \quad , \text{if } \alpha = z, \tag{C.7}$$

$$\boldsymbol{\Delta\mu}_{\alpha\beta} = \frac{1}{4\pi\eta}\left[\frac{3 z_i z_j R_\alpha R_\beta}{R^5} - \frac{5 a^2 R_\alpha R_\beta R_z^2}{R^7}\right] \quad , \text{if } \alpha \in \{x, y\}, \alpha \neq \beta, \tag{C.8}$$

$$\boldsymbol{\Delta\mu}_{\alpha z} = \frac{1}{4\pi\eta}\left[\frac{z_j R_\alpha}{R^3}\left(1 - 3\frac{z_i R_z}{R^2}\right) - \frac{a^2 R_\alpha R_z}{R^5}\left(2 - 5\frac{R_z^2}{R^2}\right)\right] \quad , \text{if } \alpha \in \{x, y\}, \tag{C.9}$$

$$\boldsymbol{\Delta\mu}_{z\alpha} = \frac{1}{4\pi\eta}\left[\frac{z_j R_\alpha}{R^3}\left(1 + 3\frac{z_i R_z}{R^2}\right) - 5\frac{a^2 R_\alpha R_z^3}{R^7}\right] \quad , \text{if } \alpha \in \{x, y\}, \tag{C.10}$$

where $\mathbf{R} = \boldsymbol{r}_i - \bar{\boldsymbol{r}}_j$. For the limit of $\boldsymbol{r}_j$ going to $\boldsymbol{r}_i$, the Rotne-Prager-Blake tensor reduces to the self mobility which is different for the directions parallel to the no-slip boundary and the perpendicular direction:

$$\boldsymbol{\mu}_{ii} = \boldsymbol{\mu}_{\mathrm{self}}^{\mathrm{RPB}}(z) = \lim_{r_{ij}\to 0} \boldsymbol{\mu}^{\mathrm{RPB}}(\boldsymbol{r}_i, \boldsymbol{r}_j) = \begin{pmatrix} \mu_{\parallel}^{\mathrm{RPB}}(z) & 0 & 0 \\ 0 & \mu_{\parallel}^{\mathrm{RPB}}(z) & 0 \\ 0 & 0 & \mu_{\perp}^{\mathrm{RPB}}(z) \end{pmatrix}, \tag{C.11}$$

where the parallel self mobility is given by

$$\mu_{\parallel}^{\mathrm{RPB}}(z) = \frac{1}{6\pi\eta a}\left[1 - \frac{9a}{16z} + \frac{1}{8}\left(\frac{a}{z}\right)^3\right] + \mathcal{O}(a^4), \tag{C.12}$$

and the perpendicular self mobility by

$$\mu_{\perp}^{\mathrm{RPB}}(z) = \frac{1}{6\pi\eta a}\left[1 - \frac{9a}{8z} + \frac{1}{2}\left(\frac{a}{z}\right)^3\right] + \mathcal{O}(a^4). \tag{C.13}$$

This symmetry-breaking leads to a correction term $\mathbf{v}_i^{\mathrm{correction}}$ that is given by[266]

$$\mathbf{v}_i^{\mathrm{correction}} = k_{\mathrm{B}} T \frac{\mathrm{d}\mu_{\perp}^{\mathrm{RPB}}(z)}{\mathrm{d}z}\Big|_{z=z_i} \hat{\mathbf{z}}. \tag{C.14}$$

So consequently the drag force defining the first term (drag term), depending on the situation, is given as

$$\mathbf{F}_{\mathrm{D},i} = \mu_0^{-1}\mathbf{v}_{\mathrm{i},\infty} = \begin{cases} \dot{\gamma}\ \mu_0\ z_i\ \hat{\mathbf{x}} & \text{(non-grafted)} \\ \dot{\gamma}\ \mu_{\parallel}^{\mathrm{RPB}}(z)\ z_i\ \hat{\mathbf{x}} & \text{(grafted)} \end{cases}. \tag{C.15}$$

The second term of Eq. (C.1) is the velocity of bead i due to the forces exerted by all other beads j. The last term of Eq. (C.1) follows from the fluctuation-dissipation theorem

$$\langle \boldsymbol{\xi}_i(t) \otimes \boldsymbol{\xi}_j(t') \rangle = 2k_{\mathrm{B}}T\boldsymbol{\mu}_{ij}\delta(t-t'). \tag{C.16}$$

To create random velocities that satisfy the correlation given by Eq. (C.16), we use the Cholesky decomposition of a matrix that is given as

$$\boldsymbol{\mu} = \begin{pmatrix} \boldsymbol{\mu}_{11} & \cdots & \boldsymbol{\mu}_{1N} \\ \vdots & \ddots & \vdots \\ \boldsymbol{\mu}_{N1} & \cdots & \boldsymbol{\mu}_{NN} \end{pmatrix} \tag{C.17}$$

which returns a lower triangular matrix, $\mathbf{L}$, that satisfies the relation $\mathbf{L}\,\mathbf{L}^{\mathrm{T}} = \boldsymbol{\mu}$. If we now define a normal random vector $\mathbf{x}$ that satisfies the conditions of gaussian white noise, meaning $\langle \mathbf{x}\,\mathbf{x}^{\mathrm{T}} \rangle = \mathbb{1}$, then one can write

$$\langle \boldsymbol{\mu} \rangle = \langle (\mathbf{L}\,\mathbf{x})\,(\mathbf{L}\,\mathbf{x})^{\mathrm{T}} \rangle = \langle \mathbf{L}\mathbf{x}\ \mathbf{x}^{\mathrm{T}}\mathbf{L}^{\mathrm{T}} \rangle = \mathbf{L}\langle \mathbf{x}\ \mathbf{x}^{\mathrm{T}} \rangle \mathbf{L}^{\mathrm{T}}. \tag{C.18}$$

So consequently, we used the following method to calculate the random velocities for each step:

$$\boldsymbol{\xi} = \begin{pmatrix} \boldsymbol{\xi}_1 \\ \vdots \\ \boldsymbol{\xi}_N \end{pmatrix} = \sqrt{\frac{2k_{\mathrm{B}}T}{\Delta t}}\ \mathbf{L}\,\mathbf{x}. \tag{C.19}$$

C.2 Simulation Parameters

N	$\Delta t/\tau$	n_t/τ	n_w/τ
10	0.0005	4000000000	100
20	0.0005	4000000000	1000
30	0.0005	1000000000	10000
75	0.0005	500000000	100
100	0.0005	500000000	10000

Table C.2: Explicit simulation parameters for the time step Δt, the total number of simulation steps n_t and the number of steps between each saving of positions of all beads n_w for the *grafted scenario*.

N	$\Delta t/\tau$	n_t/τ	n_w/τ
10	0.0005	4000000000	10000
30	0.0005	2000000000	10000
50	0.0005	1000000000	10000
75	0.0005	500000000	10000
100	0.0005	200000000	100000

Table C.4: Explicit simulation parameters for the time step Δt, the total number of simulation steps n_t and the number of steps between each saving of positions of all beads n_w for the *non-grafted scenario*.

C.3 Estimate Standard Error of the Mean

Time dependent quantities such as the squared radius of gyration and the end to end distance in pull direction are analyzed using the gromacs tool gmx analyze.[306] The error estimate of the time averaged quantity is calculated using the block average method according to the definition by Berk Hess,[307]

$$\text{err.est.}(x(t)) = \sigma\sqrt{\frac{2(\alpha\tau_1 + (1-\alpha)\tau_2)}{T}}, \tag{C.20}$$

where σ is the standard deviation of the sample and $T = n_t\Delta t$ is the total time of the simulation run. The quantities τ_1, τ_2 and α are estimates for the short correlation time,

the long correlation time and a weighting factor which are fitted using the auto correlation function of the observable in question. Note that we define the auto correlation function such that it decays to 0, meaning we actually look at the mean fluctuations of the observable minus its mean value over the sample,

$$C(\tau) = \frac{1}{(T-\tau)\sigma^2} \int_0^{T-\tau} [x(t) - \mu]\,[(x(t+\tau) - \mu]\,\mathrm{d}t. \tag{C.21}$$

A full derivation of the error estimate given in Eq. (C.20) can be found in the appendix of the 2002 article by Berk Hess.[307]

C.4 Determining Critical Shear Rate

Determining the critical shear rate

Determining the critical shear rate, $\dot{\gamma}^*$, should in principle be possible by evaluating any reasonable quantity that is directly effected by the change in shear rate that becomes maximal or minimal at the point of transition between the collapsed and non collapsed state. Previous publications used the elongation of the chain in direction of the shear flow to pinpoint the transition.[81,260]

In this section we compare a number of different quantities, which naively we would expect to give similar results for the critical shear rate. We mainly show both the squared radius of gyration, R_G^2, as well as the squared elongation in flow direction, R_S^2. We look at both their relative fluctuations, defined as

$$\sqrt{\langle R_{\mathrm{G/S}}^4(t)\rangle - \langle R_{\mathrm{G/S}}^2(t)\rangle^2} / \langle R_{\mathrm{G/S}}^2(t)\rangle^2, \tag{C.22}$$

we further calculate a relative error using the error estimate, defined in the previous section and in addition we show both the numerical derivative, $\Delta(R_{\mathrm{G/S}})/\Delta(\dot{\gamma})$ and the numerical derivative in the double logarithmic depiction, $\Delta\log(R_{\mathrm{G/S}})/\Delta\log(\dot{\gamma})$.

Looking at the results in Tab. C.5 and Tab. C.6, we see that the results for $\dot{\gamma}^*$ become disengaged, when we compare the relative fluctuation of R_G^2 and R_S^2 for either low (for bulk) or high (for grafted) number of beads, depending on the scenario. Judging from the comparisons in Fig. C.1 and Fig. C.2, we come to the conclusion that the numerical derivatives, $\Delta(R_{\mathrm{G/S}})/\Delta(\dot{\gamma})$, are a more reliable estimator for the critical shear rate, $\dot{\gamma}^*$.

Figure C.1: Grafted scenario: a comparison of different quantities that can be used to pinpoint the critical shear rate, $\dot{\gamma}^*$, as a function of the number of beads in the bead-spring chain.

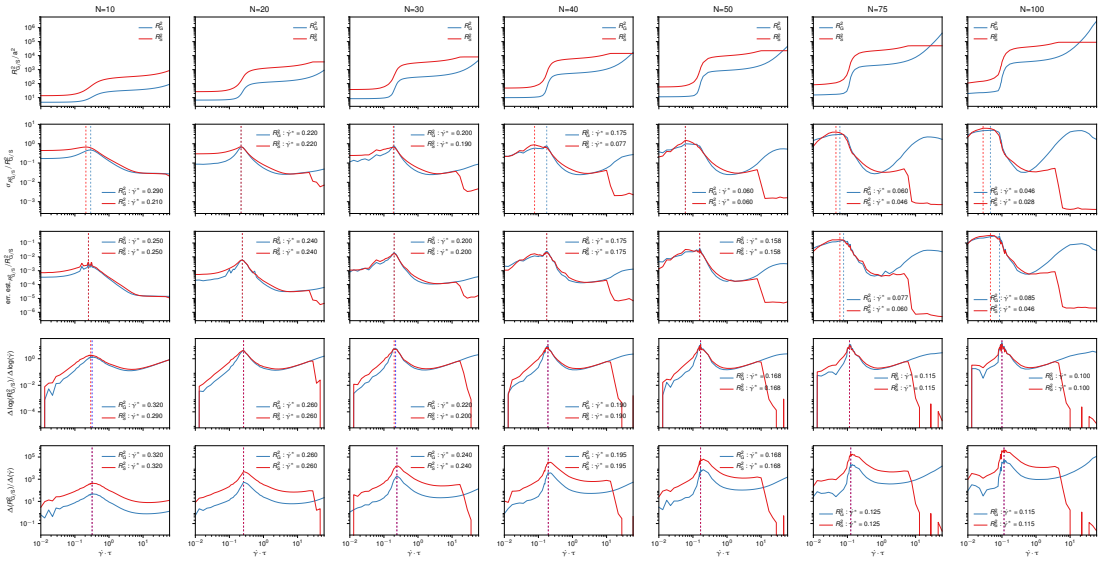

Figure C.2: Non grafted scenario: a comparison of different quantities that can be used to pinpoint the critical shear rate, $\dot{\gamma}^*$, as a function of the number of beads in the bead-spring chain.

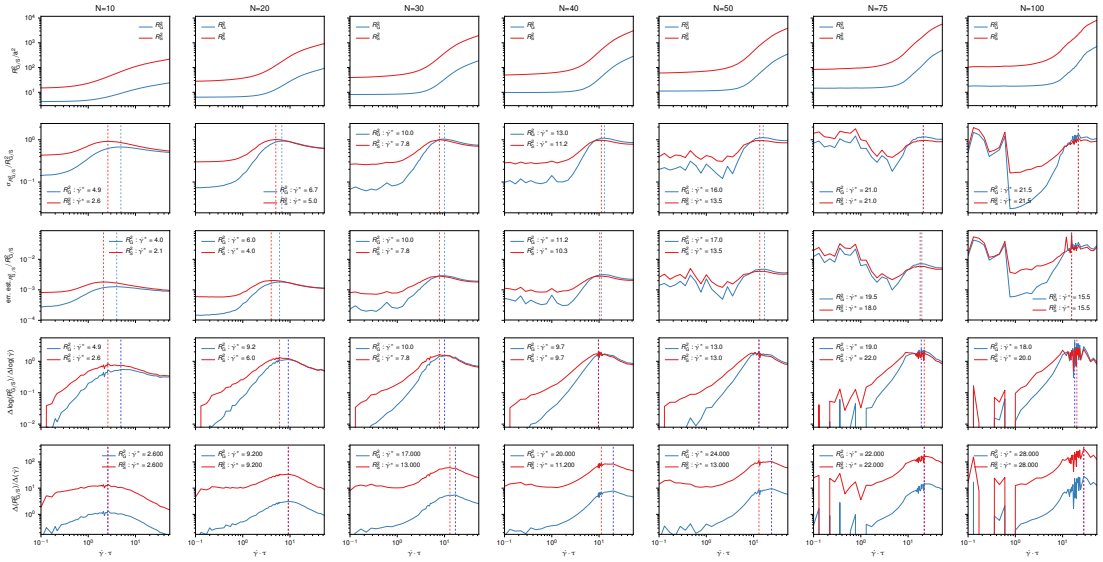

N	from $\sigma_{R_G^2}/R_G^2$	from err. est.$_{R_G^2}/R_G^2$	from $\Delta\log(R_G^2)/\Delta\log(\dot\gamma)$	from $\Delta(R_G^2)/\Delta(\dot\gamma)$	from $\sigma_{R_S^2}/R_S^2$	from err. est.$_{R_S^2}/R_S^2$	from $\Delta\log(R_S^2)/\Delta\log(\dot\gamma)$	from $\Delta(R_S^2)/\Delta(\dot\gamma)$
10	0.25	0.29	0.32	0.32	0.21	0.25	0.29	0.32
20	0.24	0.22	0.26	0.26	0.22	0.24	0.26	0.26
30	0.2	0.2	0.22	0.24	0.19	0.2	0.2	0.24
40	0.175	0.175	0.19	0.195	0.077	0.175	0.19	0.195
50	0.1575	0.06	0.1675	0.1675	0.06	0.1575	0.1675	0.1675
75	0.077	0.06	0.115	0.125	0.046	0.06	0.115	0.125
100	0.085	0.046	0.1	0.115	0.028	0.046	0.1	0.115

Table C.5: Grafted scenario: comparison of the critical shear rate results, $\dot\gamma^* \cdot \tau$, by evaluation of different characteristic quantities.

N	from $\sigma_{R_G^2}/R_G^2$	from err. est.$_{R_G^2}/R_G^2$	from $\Delta\log(R_G^2)/\Delta\log(\dot\gamma)$	from $\Delta(R_G^2)/\Delta(\dot\gamma)$	from $\sigma_{R_S^2}/R_S^2$	from err. est.$_{R_S^2}/R_S^2$	from $\Delta\log(R_S^2)/\Delta\log(\dot\gamma)$	from $\Delta(R_S^2)/\Delta(\dot\gamma)$
10	4.9	4	4.9	2.6	2.6	2.1	2.6	2.6
20	6.7	6	9.2	9.2	5	4	6	9.2
30	10	10	10	17	7.8	7.8	7.8	13
40	13	11.2	9.7	20	11.2	10.3	9.7	11.2
50	16	17	13	24	13.5	13.5	13	13
75	21	19.5	19	22	21	18	22	22
100	21.5	15.5	18	28	21.5	15.5	20	28

Table C.6: Non grafted scenario: comparison of the critical shear rate results, $\dot\gamma^* \cdot \tau$, by evaluation of different characteristic quantities.

List of Figures

List of Tables

List of Publications

The present thesis is based on the following manuscripts, which have been published or are in preparation for publication in peer-reviewed journals:

[i] R. Schwarzl, S. Liese, F. N. Brünig, F. Laudisio, and R. R. Netz, *Force Response of Polypeptide Chains from Water-Explicit MD Simulations*, Macromolecules **53**, 4618 (2020).

[ii] R. Schwarzl and R. R. Netz, *Quantification of the frequency-dependent signal transduction for the coiled coil linker Jα*, in preparation (2020).

[iii] A. Kolberg, C. Wenzel, K. Hackenstrass, R. Schwarzl, C. Rüttiger, T. Hugel, M. Gallei, R. R. Netz, and B. N. Balzer, *Opposing Temperature Dependence of the Stretching Response of Single PEG and PNiPAM Polymers*, Journal of the American Chemical Society **141**, 11603 (2019).

[iv] R. Schwarzl and R. R. Netz, *Hydrodynamic Shear Effects on Grafted and Non-Grafted Collapsed Polymers*, Polymers **10**, 926 (2018).

The following publications are related to this thesis:

[v] S. Liese, M. Gensler, S. Krysiak, R. Schwarzl, A. Achazi, B. Paulus, T. Hugel, J. P. Rabe, and R. R. Netz, *Hydration Effects Turn a Highly Stretched Polymer from an Entropic into an Energetic Spring*, ACS Nano **11**, 702 (2017).

[vi] S. Posch, C. Aponte-Santamaría, R. Schwarzl, A. Karner, M. Radtke, F. Gräter, T. Obser, G. König, M. A. Brehm, H. J. Gruber, R. R. Netz, C. Baldauf, R. Schneppenheim, R. Tampé, and P. Hinterdorfer, *Mutual A domain interactions in the force sensing protein von Willebrand factor*, Journal of Structural Biology **197**, 57 (2017).

[vii] S. Posch, C. Aponte-Santamaría, R. Schwarzl, A. Karner, M. Radtke, F. Gräter, T. Obser, G. König, M. A. Brehm, H. J. Gruber, R. R. Netz, C. Baldauf, R. Schneppenheim, R. Tampé, and P. Hinterdorfer, *Single molecule force spectroscopy data and BD- and MD simulations on the blood protein von Willebrand factor*, Data in Brief **8**, 1080 (2016).

The following publications are unrelated to this thesis:

[viii] M. L. Unbehauen, D. Łabuz, R. Schwarzl, S. Moré, R. R. Netz, C. Stein, H. Machelska, and R. Haag, *Tailor-Made Core-Multishell Nanocarriers for the Delivery of Cationic Analgesics to Inflamed Tissue*, Advanced Therapeutics **2**, 1900007 (2019).

[ix] R. Schwarzl, F. Du, R. Haag, and R. R. Netz, *General method for the quantification of drug loading and release kinetics of nanocarriers*, European Journal of Pharmaceutics and Biopharmaceutics **116**, 131 (2017).

[x] H. Krüsemann, R. Schwarzl, and R. Metzler, *Ageing Scher–Montroll Transport*, Transport in Porous Media **115**, 327 (2016).

[xi] P. Pingel, R. Schwarzl, and D. Neher, *Effect of molecular p-doping on hole density and mobility in poly(3-hexylthiophene)*, Applied Physics Letters **100**, 143303 (2012).

Bibliography

[1] R. A. Dwek, *Glycobiology: Toward Understanding the Function of Sugars,* Chemical Reviews **96**, 683 (1996).

[2] M. Edidin, *Lipids on the frontier: a century of cell-membrane bilayers,* Nature Reviews Molecular Cell Biology **4**, 414 (2003).

[3] E. Z. Eisenmesser, D. A. Bosco, M. Akke, and D. Kern, *Enzyme Dynamics During Catalysis,* Science **295**, 1520 (2002).

[4] S.-R. Tzeng and C. G. Kalodimos, *Protein activity regulation by conformational entropy,* Nature **488**, 236 (2012).

[5] M. B. Eisen, P. T. Spellman, P. O. Brown, and D. Botstein, *Cluster analysis and display of genome-wide expression patterns,* Proceedings of the National Academy of Sciences **95**, 14863 (1998).

[6] Nobelprize.org, The Nobel Prize in Chemistry 1946, `https://www.nobelprize.org/prizes/chemistry/1946/summary/` (2020).

[7] Nobelprize.org, The Nobel Prize in Chemistry 1958, `https://www.nobelprize.org/prizes/chemistry/1958/` (2020).

[8] F. Sanger, *The free amino groups of insulin,* Biochemical Journal **39**, 507 (1945).

[9] F. Sanger and H. Tuppy, *The amino-acid sequence in the phenylalanyl chain of insulin. 1. The identification of lower peptides from partial hydrolysates,* Biochemical Journal **49**, 463 (1951).

[10] A. P. Ryle, F. Sanger, L. F. Smith, and R. Kitai, *The disulphide bonds of insulin,* Biochemical Journal **60**, 541 (1955).

[11] C. J. Wilson, R. E. Clegg, D. I. Leavesley, and M. J. Pearcy, *Mediation of Biomaterial–Cell Interactions by Adsorbed Proteins: A Review,* Tissue Engineering **11**, 1 (2005).

[12] I. Salama, P. Malone, F. Mihaimeed, and J. Jones, *A review of the S100 proteins in cancer,* European Journal of Surgical Oncology (EJSO) **34**, 357 (2008).

[13] B. H. Sarmadi and A. Ismail, *Antioxidative peptides from food proteins: A review,* Peptides **31**, 1949 (2010).

[14] B. Bragdon, O. Moseychuk, S. Saldanha, D. King, J. Julian, and A. Nohe, *Bone Morphogenetic Proteins: A critical review,* Cellular Signalling **23**, 609 (2011).

[15] L. E. Kay, D. A. Torchia, and A. Bax, *Backbone dynamics of proteins as studied by nitrogen-15 inverse detected heteronuclear NMR spectroscopy: application to staphylococcal nuclease,* Biochemistry **28**, 8972 (1989).

[16] D. Marion, M. Ikura, R. Tschudin, and A. Bax, *Rapid recording of 2D NMR spectra without phase cycling. Application to the study of hydrogen exchange in proteins,* Journal of Magnetic Resonance **85**, 393 (1989).

[17] D. S. Wishart, B. D. Sykes, and F. M. Richards, *The chemical shift index: a fast and simple method for the assignment of protein secondary structure through NMR spectroscopy,* Biochemistry **31**, 1647 (1992).

[18] A. Mittermaier, *New Tools Provide New Insights in NMR Studies of Protein Dynamics,* Science **312**, 224 (2006).

[19] R. H. Somani, B. S. Hsiao, A. Nogales, S. Srinivas, A. H. Tsou, I. Sics, F. J. Balta-Calleja, and T. A. Ezquerra, *Structure Development during Shear Flow-Induced Crystallization of i-PP: In-Situ Small-Angle X-ray Scattering Study,* Macromolecules **33**, 9385 (2000).

[20] B. Chu and B. S. Hsiao, *Small-Angle X-ray Scattering of Polymers,* Chemical Reviews **101**, 1727 (2001).

[21] J. Lipfert and S. Doniach, *Small-Angle X-Ray Scattering from RNA, Proteins, and Protein Complexes,* Annual Review of Biophysics and Biomolecular Structure **36**, 307 (2007).

[22] M. Rief, *Single Molecule Force Spectroscopy on Polysaccharides by Atomic Force Microscopy,* Science **275**, 1295 (1997).

[23] M. Rief, J. Pascual, M. Saraste, and H. E. Gaub, *Single molecule force spectroscopy of spectrin repeats: low unfolding forces in helix bundles,* Journal of Molecular Biology **286**, 553 (1999).

[24] M. Benoit, D. Gabriel, G. Gerisch, and H. E. Gaub, *Discrete interactions in cell adhesion measured by single-molecule force spectroscopy,* Nature Cell Biology **2**, 313 (2000).

[25] N. B. Holland, T. Hugel, G. Neuert, A. Cattani-Scholz, C. Renner, D. Oesterhelt, L. Moroder, M. Seitz, and H. E. Gaub, *Single Molecule Force Spectroscopy of Azobenzene Polymers: Switching Elasticity of Single Photochromic Macromolecules,* Macromolecules **36**, 2015 (2003).

[26] K. C. Neuman and A. Nagy, *Single-molecule force spectroscopy: optical tweezers, magnetic tweezers and atomic force microscopy,* Nature Methods **5**, 491 (2008).

[27] D. Stoner-Ma, A. A. Jaye, P. Matousek, M. Towrie, S. R. Meech, and P. J. Tonge, *Observation of Excited-State Proton Transfer in Green Fluorescent Protein using Ultrafast Vibrational Spectroscopy,* Journal of the American Chemical Society **127**, 2864 (2005).

[28] K. T. Nguyen, S. V. Le Clair, S. Ye, and Z. Chen, *Orientation Determination of Protein Helical Secondary Structures Using Linear and Nonlinear Vibrational Spectroscopy,* The Journal of Physical Chemistry B **113**, 12169 (2009).

[29] R. Adato, A. A. Yanik, J. J. Amsden, D. L. Kaplan, F. G. Omenetto, M. K. Hong, S. Erramilli, and H. Altug, *Ultra-sensitive vibrational spectroscopy of protein monolayers with plasmonic nanoantenna arrays,* Proceedings of the National Academy of Sciences **106**, 19227 (2009).

[30] A. Rygula, K. Majzner, K. M. Marzec, A. Kaczor, M. Pilarczyk, and M. Baranska, *Raman spectroscopy of proteins: a review,* Journal of Raman Spectroscopy **44**, 1061 (2013).

[31] S. R. Babu and P. Ammasi, *Fluorescence resonance energy transfer (FRET) microscopy imaging of live cell protein localizations ,* Journal of Cell Biology **160**, 629 (2003).

[32] B. Schuler, *Single Molecule FRET of Protein Folding Dynamics,* The FASEB Journal **23**, 327.1 (2009).

[33] H. Sahoo, *Förster resonance energy transfer – A spectroscopic nanoruler: Principle and applications,* Journal of Photochemistry and Photobiology C: Photochemistry Reviews **12**, 20 (2011).

[34] J. N. Onuchic, Z. Luthey-Schulten, and P. G. Wolynes, *THEORY OF PROTEIN FOLDING: The Energy Landscape Perspective,* Annual Review of Physical Chemistry **48**, 545 (1997).

[35] C. M. Dobson, A. Šali, and M. Karplus, *Protein Folding: A Perspective from Theory and Experiment,* Angewandte Chemie International Edition **37**, 868 (1998).

[36] L. Mirny and E. Shakhnovich, *Protein Folding Theory: From Lattice to All-Atom Models,* Annual Review of Biophysics and Biomolecular Structure **30**, 361 (2001).

[37] J. N. Onuchic and P. G. Wolynes, *Theory of protein folding,* Current Opinion in Structural Biology **14**, 70 (2004).

[38] O. K. Dudko, T. G. W. Graham, and R. B. Best, *Locating the barrier for folding of single molecules under an external force,* Physical Review Letters **107**, 3 (2011).

[39] W. K. Kim and R. R. Netz, *The mean shape of transition and first-passage paths,* The Journal of Chemical Physics **143**, 224108 (2015).

[40] D. L. Ermak and J. A. McCammon, *Brownian dynamics with hydrodynamic interactions,* The Journal of Chemical Physics **69**, 1352 (1978).

[41] M. Hinczewski, X. Schlagberger, M. Rubinstein, O. Krichevsky, and R. R. Netz, *End-Monomer Dynamics in Semiflexible Polymers,* Macromolecules **42**, 860 (2009).

[42] J. O. Daldrop, J. Kappler, F. N. Brünig, and R. R. Netz, *Butane dihedral angle dynamics in water is dominated by internal friction,* Proceedings of the National Academy of Sciences **115**, 5169 (2018).

[43] J. Hasty, D. McMillen, F. Isaacs, and J. J. Collins, *Computational studies of gene regulatory networks: in numero molecular biology,* Nature Reviews Genetics **2**, 268 (2001).

[44] D. E. Shaw, M. M. Deneroff, R. O. Dror, J. S. Kuskin, R. H. Larson, J. K. Salmon, C. Young, B. Batson, K. J. Bowers, J. C. Chao, M. P. Eastwood, J. Gagliardo, J. P. Grossman, C. R. Ho, D. J. Ierardi, I. Kolossváry, J. L. Klepeis, T. Layman, C. McLeavey, M. A. Moraes, R. Mueller, E. C. Priest, Y. Shan, J. Spengler, M. Theobald, B. Towles, and S. C. Wang, *Anton, a Special-Purpose Machine for Molecular Dynamics Simulation,* SIGARCH Comput. Archit. News **35**, 1–12 (2007).

[45] K. A. Dill and J. L. MacCallum, *The protein-folding problem, 50 years on,* Science **338**, 1042 (2012).

[46] E. Schneck, D. Horinek, and R. R. Netz, *Insight into the Molecular Mechanisms of Protein Stabilizing Osmolytes from Global Force-Field Variations,* The Journal of Physical Chemistry B **117**, 8310 (2013).

[47] K. Lindorff-Larsen, P. Maragakis, S. Piana, and D. E. Shaw, *Picosecond to Millisecond Structural Dynamics in Human Ubiquitin,* The Journal of Physical Chemistry B **120**, 8313 (2016).

[48] S. Liese, M. Gensler, S. Krysiak, R. Schwarzl, A. Achazi, B. Paulus, T. Hugel, J. P. Rabe, and R. R. Netz, *Hydration Effects Turn a Highly Stretched Polymer from an Entropic into an Energetic Spring,* ACS Nano **11**, 702 (2017).

[49] J. Gao and D. G. Truhlar, *Quantum Mechanical Methods for Enzyme Kinetics,* Annual Review of Physical Chemistry **53**, 467 (2002).

[50] H. Hu and W. Yang, *Free Energies of Chemical Reactions in Solution and in Enzymes with Ab Initio Quantum Mechanics/Molecular Mechanics Methods,* Annual Review of Physical Chemistry **59**, 573 (2008).

[51] J. O. Daldrop, M. Saita, M. Heyden, V. A. Lorenz-Fonfria, J. Heberle, and R. R. Netz, *Orientation of non-spherical protonated water clusters revealed by infrared absorption dichroism,* Nature Communications **9**, 311 (2018).

[52] A. Tobolsky and H. Eyring, *Mechanical Properties of Polymeric Materials,* The Journal of Chemical Physics **11**, 125 (1943).

[53] P.-G. de Gennes, *Scaling Concepts in Polymer Physics* (Cornell University Press, 1979).

[54] E. Chiellini and R. Solaro, *Biodegradable Polymeric Materials,* Advanced Materials **8**, 305 (1996).

[55] J. Ruokolainen, R. Mäkinen, M. Torkkeli, T. Mäkelä, R. Serimaa, G. ten Brinke, and O. Ikkala, *Switching Supramolecular Polymeric Materials with Multiple Length Scales,* Science **280**, 557 (1998).

[56] F. van de Manakker, T. Vermonden, C. F. van Nostrum, and W. E. Hennink, *Cyclodextrin-Based Polymeric Materials: Synthesis, Properties, and Pharmaceutical/Biomedical Applications,* Biomacromolecules **10**, 3157 (2009).

[57] U. Hersel, C. Dahmen, and H. Kessler, *RGD modified polymers: biomaterials for stimulated cell adhesion and beyond,* Biomaterials **24**, 4385 (2003).

[58] V. Siracusa, P. Rocculi, S. Romani, and M. D. Rosa, *Biodegradable polymers for food packaging: a review,* Trends in Food Science & Technology **19**, 634 (2008).

[59] C. Liu, H. Qin, and P. T. Mather, *Review of progress in shape-memory polymers,* J. Mater. Chem. **17**, 1543 (2007).

[60] G. W. Ehrenstein, *Polymeric Materials: Structure, Properties, Applications* (Carl Hanser Verlag GmbH & Company KG, 2012).

[61] M. I. Sabir, X. Xu, and L. Li, *A review on biodegradable polymeric materials for bone tissue engineering applications,* Journal of Materials Science **44**, 5713 (2009).

[62] L. Polo-Corrales, M. Latorre-Esteves, and J. E. Ramirez-Vick, *Scaffold design for bone regeneration,* Journal of nanoscience and nanotechnology **14**, 15 (2014).

[63] T. Ghassemi, A. Shahroodi, M. H. Ebrahimzadeh, A. Mousavian, J. Movaffagh, and A. Moradi, *Current Concepts in Scaffolding for Bone Tissue Engineering,* The archives of bone and joint surgery **6**, 90 (2018).

[64] R. Haag, *Supramolecular Drug-Delivery Systems Based on Polymeric Core–Shell Architectures,* Angewandte Chemie International Edition **43**, 278 (2004).

[65] E. Fleige, M. A. Quadir, and R. Haag, *Stimuli-responsive polymeric nanocarriers for the controlled transport of active compounds: Concepts and applications,* Advanced Drug Delivery Reviews **64**, 866 (2012).

[66] P. Kesharwani, K. Jain, and N. K. Jain, *Dendrimer as nanocarrier for drug delivery,* Progress in Polymer Science **39**, 268 (2014).

[67] S. Posch, C. Aponte-Santamaría, R. Schwarzl, A. Karner, M. Radtke, F. Gräter, T. Obser, G. König, M. A. Brehm, H. J. Gruber, R. R. Netz, C. Baldauf, R. Schneppenheim, R. Tampé, and P. Hinterdorfer, *Single molecule force spectroscopy data and BD- and MD simulations on the blood protein von Willebrand factor,* Data in Brief **8**, 1080 (2016).

[68] S. Posch, C. Aponte-Santamaría, R. Schwarzl, A. Karner, M. Radtke, F. Gräter, T. Obser, G. König, M. A. Brehm, H. J. Gruber, R. R. Netz, C. Baldauf, R. Schneppenheim, R. Tampé, and P. Hinterdorfer, *Mutual A domain interactions in the force sensing protein von Willebrand factor,* Journal of Structural Biology **197**, 57 (2017).

[69] R. Schwarzl, F. Du, R. Haag, and R. R. Netz, *General method for the quantification of drug loading and release kinetics of nanocarriers,* European Journal of Pharmaceutics and Biopharmaceutics **116**, 131 (2017).

[70] M. L. Unbehauen, D. Łabuz, R. Schwarzl, S. Moré, R. R. Netz, C. Stein, H. Machelska, and R. Haag, *Tailor-Made Core-Multishell Nanocarriers for the Delivery of Cationic Analgesics to Inflamed Tissue,* Advanced Therapeutics **2**, 1900007 (2019).

[71] A. Kolberg, C. Wenzel, K. Hackenstrass, R. Schwarzl, C. Rüttiger, T. Hugel, M. Gallei, R. R. Netz, and B. N. Balzer, *Opposing Temperature Dependence of the Stretching Response of Single PEG and PNiPAM Polymers,* Journal of the American Chemical Society **141**, 11603 (2019).

[72] A. Möglich, R. A. Ayers, and K. Moffat, *Design and Signaling Mechanism of Light-Regulated Histidine Kinases,* Journal of Molecular Biology **385**, 1433 (2009).

[73] A. Möglich, *Signal transduction in photoreceptor histidine kinases,* Protein Science **28**, 1923 (2019).

[74] A. Alexander-Katz, M. F. Schneider, S. W. Schneider, A. Wixforth, and R. R. Netz, *Shear-Flow-Induced Unfolding of Polymeric Globules,* Physical Review Letters **97**, 138101 (2006).

[75] S. W. Schneider, S. Nuschele, A. Wixforth, C. Gorzelanny, A. Alexander-Katz, R. R. Netz, and M. F. Schneider, *Shear-induced unfolding triggers adhesion of*

von Willebrand factor fibers, Proceedings of the National Academy of Sciences **104**, 7899 (2007).

[76] C. Siediecki, B. Lestini, K. Kottke-Marchant, S. Eppell, D. Wilson, and R. Marchant, *Shear-dependent changes in the three-dimensional structure of human von Willebrand factor,* Blood **88**, 2939 (1996).

[77] T. a. Springer, *Biology and physics of von Willebrand factor concatamers,* Journal of Thrombosis and Haemostasis **9**, 130 (2011).

[78] T. A. Springer, *von Willebrand factor, Jedi knight of the bloodstream,* Blood **124**, 1412 (2014).

[79] T. V. Colace and S. L. Diamond, *Direct Observation of von Willebrand Factor Elongation and Fiber Formation on Collagen During Acute Whole Blood Exposure to Pathological Flow,* Arteriosclerosis, Thrombosis, and Vascular Biology **33**, 105 (2013).

[80] S. Lippok, M. Radtke, T. Obser, L. Kleemeier, R. Schneppenheim, U. Budde, R. R. Netz, and J. O. Rädler, *Shear-Induced Unfolding and Enzymatic Cleavage of Full-Length VWF Multimers,* Biophysical Journal **110**, 545 (2016).

[81] M. Radtke, S. Lippok, J. O. Rädler, and R. R. Netz, *Internal tension in a collapsed polymer under shear flow and the connection to enzymatic cleavage of von Willebrand factor,* The European Physical Journal E **39**, 32 (2016).

[82] K. Rack, V. Huck, M. Hoore, D. A. Fedosov, S. W. Schneider, and G. Gompper, *Margination and stretching of von Willebrand factor in the blood stream enable adhesion,* Scientific Reports **7**, 14278 (2017).

[83] S. Posch, T. Obser, G. König, R. Schneppenheim, R. Tampé, and P. Hinterdorfer, *Interaction of von Willebrand factor domains with collagen investigated by single molecule force spectroscopy,* The Journal of Chemical Physics **148**, 123310 (2018).

[84] K. Wang, J. G. Forbes, and A. J. Jin, *Single molecule measurements of titin elasticity,* Progress in Biophysics and Molecular Biology **77**, 1 (2001).

[85] E. M. Puchner and H. E. Gaub, *Force and function: probing proteins with AFM-based force spectroscopy,* Current Opinion in Structural Biology **19**, 605 (2009).

[86] M. Geisler, S. Xiao, E. M. Puchner, F. Gräter, and T. Hugel, *Controlling the Structure of Proteins at Surfaces,* Journal of the American Chemical Society **132**, 17277 (2010).

[87] S. Kienle, S. Liese, N. Schwierz, R. R. Netz, and T. Hugel, *The Effect of Temperature on Single-Polypeptide Adsorption,* ChemPhysChem **13**, 982 (2012).

[88] M. Wei, Y. Gao, X. Li, and M. J. Serpe, *Stimuli-responsive polymers and their applications,* Polym. Chem. **8**, 127 (2017).

[89] S. Kuroyanagi, N. Shimada, S. Fujii, T. Furuta, A. Harada, K. Sakurai, and A. Maruyama, *Highly Ordered Polypeptide with UCST Phase Separation Behavior,* Journal of the American Chemical Society **141**, 1261 (2019).

[90] G. Meyer and N. M. Amer, *Erratum: Novel optical approach to atomic force microscopy,* Applied Physics Letters **53**, 2400 (1988).

[91] M. J. Allen, E. M. Bradbury, and R. Balhorn, *AFM analysis of DNA-protamine complexes bound to mica,* Nucleic Acids Research **25**, 2221 (1997).

[92] M. Rief, *Reversible Unfolding of Individual Titin Immunoglobulin Domains by AFM,* Science **276**, 1109 (1997).

[93] T. Hugel and M. Seitz, *The Study of Molecular Interactions by AFM Force Spectroscopy,* Macromolecular Rapid Communications **22**, 989 (2001).

[94] Y. L. Lyubchenko and L. S. Shlyakhtenko, *AFM for analysis of structure and dynamics of DNA and protein-DNA complexes,* Methods **47**, 206 (2009).

[95] J. Camunas-Soler, M. Ribezzi-Crivellari, and F. Ritort, *Elastic Properties of Nucleic Acids by Single-Molecule Force Spectroscopy,* Annual Review of Biophysics **45**, 65 (2016).

[96] L. Grebikova, M. Radiom, P. Maroni, A. D. Schlüter, and M. Borkovec, *Recording stretching response of single polymer chains adsorbed on solid substrates,* Polymer **102**, 350 (2016).

[97] M. Fixman and J. Kovac, *Dynamics of stiff polymer chains. I,* The Journal of Chemical Physics **61**, 4939 (1974).

[98] P. D. Gennes, *Scaling theory of polymer adsorption,* Journal de Physique **37**, 1445 (1976).

[99] F. Manca, S. Giordano, P. L. Palla, R. Zucca, F. Cleri, and L. Colombo, *Elasticity of flexible and semiflexible polymers with extensible bonds in the Gibbs and Helmholtz ensembles,* The Journal of Chemical Physics **136**, 154906 (2012).

[100] J. F. Marko and E. D. Siggia, *Stretching DNA,* Macromolecules **28**, 8759 (1995).

[101] T. Odijk, *Stiff Chains and Filaments under Tension,* Macromolecules **28**, 7016 (1995).

[102] C. Bouchiat, M. D. Wang, J.-F. Allemand, T. Strick, S. Block, and V. Croquette, *Estimating the persistence length of a worm-like chain molecule from force-extension measurements,* Biophysical journal **76**, 409 (1999).

[103] L. Tskhovrebova, J. Trinick, J. A. Sleep, and R. M. Simmons, *Elasticity and unfolding of single molecules of the giant muscle protein titin,* Nature **387**, 308 (1997).

[104] F. Gräter, J. Shen, H. Jiang, M. Gautel, and H. Grubmüller, *Mechanically induced titin kinase activation studied by force-probe molecular dynamics simulations,* Biophysical journal **88**, 790 (2005).

[105] A. Grützner, S. Garcia-Manyes, S. Kötter, C. L. Badilla, J. M. Fernandez, and W. A. Linke, *Modulation of titin-based stiffness by disulfide bonding in the cardiac titin N2-B unique sequence,* Biophysical journal **97**, 825 (2009).

[106] L. Livadaru, R. R. Netz, and H. J. Kreuzer, *Stretching Response of Discrete Semiflexible Polymers,* Macromolecules **36**, 3732 (2003).

[107] T. Hugel, M. Rief, M. Seitz, H. E. Gaub, and R. R. Netz, *Highly Stretched Single Polymers: Atomic-Force-Microscope Experiments Versus Ab-Initio Theory,* Physical Review Letters **94**, 048301 (2005).

[108] F. Hanke, A. Serr, H. J. Kreuzer, and R. R. Netz, *Stretching single polypeptides: The effect of rotational constraints in the backbone,* EPL (Europhysics Letters) **92**, 53001 (2010).

[109] V. Hornak, R. Abel, A. Okur, B. Strockbine, A. Roitberg, and C. Simmerling, *Comparison of multiple Amber force fields and development of improved protein backbone parameters,* Proteins: Structure, Function, and Bioinformatics **65**, 712 (2006).

[110] B. K. Ho and R. Brasseur, *The Ramachandran plots of glycine and pre-proline.* BMC structural biology **5**, 14 (2005).

[111] J. Huang, S. Rauscher, G. Nawrocki, T. Ran, M. Feig, B. L. de Groot, H. Grubmüller, and A. D. MacKerell, *CHARMM36m: an improved force field for folded and intrinsically disordered proteins,* Nature Methods **14**, 71 (2016).

[112] G. A. Balaji, H. G. Nagendra, V. N. Balaji, and S. N. Rao, *Experimental conformational energy maps of proteins and peptides,* Proteins: Structure, Function and Bioinformatics **85**, 979 (2017).

[113] R. R. Netz and D. Andelman, *Neutral and charged polymers at interfaces,* Physics Reports **380**, 1 (2003).

[114] A. Dittmore, D. B. McIntosh, S. Halliday, and O. A. Saleh, *Single-Molecule Elasticity Measurements of the Onset of Excluded Volume in Poly(Ethylene Glycol),* Phys. Rev. Lett. **107**, 148301 (2011).

[115] P. Pincus, *Excluded Volume Effects and Stretched Polymer Chains,* Macromolecules **9**, 386 (1976).

[116] O. A. Saleh, D. B. McIntosh, P. Pincus, and N. Ribeck, *Nonlinear Low-Force Elasticity of Single-Stranded DNA Molecules,* Phys. Rev. Lett. **102**, 068301 (2009).

[117] G. Morrison, C. Hyeon, N. M. Toan, B.-Y. Ha, and D. Thirumalai, *Stretching Homopolymers,* Macromolecules **40**, 7343 (2007).

[118] O. A. Saleh, *Perspective: Single polymer mechanics across the force regimes,* The Journal of Chemical Physics **142**, 194902 (2015).

[119] J. P. Berezney and O. A. Saleh, *Electrostatic Effects on the Conformation and Elasticity of Hyaluronic Acid, a Moderately Flexible Polyelectrolyte,* Macromolecules **50**, 1085 (2017).

[120] D. Van Der Spoel, E. Lindahl, B. Hess, G. Groenhof, A. E. Mark, and H. J. C. Berendsen, *GROMACS: Fast, flexible, and free,* Journal of Computational Chemistry **26**, 1701 (2005).

[121] G. Bussi, D. Donadio, and M. Parrinello, *Canonical sampling through velocity rescaling,* The Journal of Chemical Physics **126**, 14101 (2007).

[122] M. Parrinello and A. Rahman, *Polymorphic transitions in single crystals: A new molecular dynamics method,* Journal of Applied Physics **52**, 7182 (1981).

[123] U. Essmann, L. Perera, M. L. Berkowitz, T. Darden, H. Lee, and L. G. Pedersen, *A smooth particle mesh Ewald method,* The Journal of Chemical Physics **103**, 8577 (1995).

[124] V. Hornak, R. Abel, A. Okur, B. Strockbine, A. Roitberg, and C. Simmerling, *Comparison of multiple Amber force fields and development of improved protein backbone parameters,* Proteins: Structure, Function, and Bioinformatics **65**, 712 (2006).

[125] M. D. Hanwell, D. E. Curtis, D. C. Lonie, T. Vandermeersch, E. Zurek, and G. R. Hutchison, *Avogadro: an advanced semantic chemical editor, visualization, and analysis platform,* Journal of Cheminformatics **4**, 17 (2012).

[126] W. L. Jorgensen, J. Chandrasekhar, J. D. Madura, R. W. Impey, and M. L. Klein, *Comparison of simple potential functions for simulating liquid water,* The Journal of Chemical Physics **79**, 926 (1983).

[127] G. Desiraju and T. Steiner, *International Union of Crystallography Monographs on Crystallography* (Oxford University Press, Oxford, 2001).

[128] D. van der Spoel, P. J. van Maaren, P. Larsson, and N. Tîmneanu, *Thermodynamics of Hydrogen Bonding in Hydrophilic and Hydrophobic Media,* The Journal of Physical Chemistry B **110**, 4393 (2006).

[129] P. A. Wood, F. H. Allen, and E. Pidcock, *Hydrogen-bond directionality at the donor H atom-analysis of interaction energies and database statistics,* CrystEngComm **11**, 1563 (2009).

[130] N. Michaud-Agrawal, E. J. Denning, T. B. Woolf, and O. Beckstein, *MDAnalysis: A toolkit for the analysis of molecular dynamics simulations,* Journal of Computational Chemistry **32**, 2319 (2011).

[131] R. J. Gowers, M. Linke, J. Barnoud, T. J. E. Reddy, M. N. Melo, S. L. Seyler, J. Domański, D. L. Dotson, S. Buchoux, I. M. Kenney, and O. Beckstein, in *Proceedings of the 15th Python in Science Conference*, edited by S. Benthall and S. Rostrup (2016) pp. 98–105.

[132] S. Kumar, J. M. Rosenberg, D. Bouzida, R. H. Swendsen, and P. A. Kollman, *THE weighted histogram analysis method for free-energy calculations on biomolecules. I. The method,* Journal of Computational Chemistry **13**, 1011 (1992).

[133] P. Höchtl, S. Boresch, W. Bitomsky, and O. Steinhauser, *Rationalization of the dielectric properties of common three-site water models in terms of their force field parameters,* Journal of Chemical Physics **109**, 4927 (1998).

[134] D. A. Pearlman, D. A. Case, J. W. Caldwell, W. S. Ross, T. E. Cheatham, S. DeBolt, D. Ferguson, G. Seibel, and P. Kollman, *AMBER, a package of computer programs for applying molecular mechanics, normal mode analysis, molecular dynamics and free energy calculations to simulate the structural and energetic properties of molecules,* Computer Physics Communications **91**, 1 (1995).

[135] J. Hutter, M. Iannuzzi, F. Schiffmann, and J. Vandevondele, *Cp2k: Atomistic simulations of condensed matter systems,* Wiley Interdisciplinary Reviews: Computational Molecular Science **4**, 15 (2014).

[136] R. A. Kendall, T. H. Dunning, and R. J. Harrison, *Electron affinities of the first-row atoms revisited. Systematic basis sets and wave functions,* The Journal of Chemical Physics **96**, 6796 (1992).

[137] S. Grimme, J. Antony, S. Ehrlich, and H. Krieg, The Journal of Chemical Physics **132**, 154104 (2010).

[138] Y. Gu, M.-D. Filippi, J. A. Cancelas, J. E. Siefring, E. P. Williams, A. C. Jasti, C. E. Harris, A. W. Lee, R. Prabhakar, S. J. Atkinson, D. J. Kwiatkowski, and D. A. Williams, *Hematopoietic Cell Regulation by Rac1 and Rac2 Guanosine Triphosphatases,* Science **302**, 445 (2003).

[139] G. Di Paolo and P. De Camilli, *Phosphoinositides in cell regulation and membrane dynamics,* Nature **443**, 651 (2006).

[140] W. G. Junger, *Immune cell regulation by autocrine purinergic signalling,* Nature Reviews Immunology **11**, 201 (2011).

[141] Å. Apelqvist, H. Li, L. Sommer, P. Beatus, D. J. Anderson, T. Honjo, M. H. de Angelis, U. Lendahl, and H. Edlund, *Notch signalling controls pancreatic cell differentiation,* Nature **400**, 877 (1999).

[142] M.-C. Rissoan, V. Soumelis, N. Kadowaki, G. Grouard, F. Briere, R. d. W. Malefyt, and Y.-J. Liu, *Reciprocal Control of T Helper Cell and Dendritic Cell Differentiation,* Science **283**, 1183 (1999).

[143] D. Mucida, Y. Park, G. Kim, O. Turovskaya, I. Scott, M. Kronenberg, and H. Cheroutre, *Reciprocal TH17 and Regulatory T Cell Differentiation Mediated by Retinoic Acid,* Science **317**, 256 (2007).

[144] H. E. Hamm, *The Many Faces of G Protein Signaling,* Journal of Biological Chemistry **273**, 669 (1998).

[145] T. Gleichmann, R. P. Diensthuber, and A. Möglich, *Charting the signal trajectory in a light-oxygen-voltage photoreceptor by random mutagenesis and covariance analysis,* Journal of Biological Chemistry **288**, 29345 (2013).

[146] M. Yamamoto, T. W. Kensler, and H. Motohashi, *The KEAP1-NRF2 System: a Thiol-Based Sensor-Effector Apparatus for Maintaining Redox Homeostasis,* Physiological Reviews **98**, 1169 (2018).

[147] A. W. Nguyen and P. S. Daugherty, *Evolutionary optimization of fluorescent proteins for intracellular FRET,* Nature Biotechnology **23**, 355 (2005).

[148] A. J. Lam, F. St-Pierre, Y. Gong, J. D. Marshall, P. J. Cranfill, M. A. Baird, M. R. McKeown, J. Wiedenmann, M. W. Davidson, M. J. Schnitzer, R. Y. Tsien, and M. Z. Lin, *Improving FRET dynamic range with bright green and red fluorescent proteins,* Nature Methods **9**, 1005 (2012).

[149] D. Mochly-Rosen, *Localization of protein kinases by anchoring proteins: a theme in signal transduction,* Science **268**, 247 (1995).

[150] G. M. Barton and R. Medzhitov, *Toll-Like Receptor Signaling Pathways,* Science **300**, 1524 (2003).

[151] E. Vivier, J. A. Nunès, and F. Vély, *Natural Killer Cell Signaling Pathways,* Science **306**, 1517 (2004).

[152] A. Camilli and B. L. Bassler, *Bacterial Small-Molecule Signaling Pathways,* Science **311**, 1113 (2006).

[153] C. Zhao, X. Zhang, K. Li, S. Zhu, Z. Guo, L. Zhang, F. Wang, Q. Fei, S. Luo, P. Shi, H. Tian, and W.-H. Zhu, *Förster Resonance Energy Transfer Switchable Self-Assembled Micellar Nanoprobe: Ratiometric Fluorescent Trapping of Endogenous H2S Generation via Fluvastatin-Stimulated Upregulation,* Journal of the American Chemical Society **137**, 8490 (2015).

[154] M. A. Bhate, K. A. Molnar, M. Goulian, and W. F. Degrado, *Signal Transduction in Histidine Kinases: Insights from New Structures,* Structure **23**, 981 (2015).

[155] S. Goetzl, C. Teutloff, T. Werther, S. E. Hennig, J.-H. Jeoung, R. Bittl, and H. Dobbek, *Protein Dynamics in the Reductive Activation of a B12-Containing Enzyme,* Biochemistry **56**, 5496 (2017).

[156] B. Buchli, S. A. Waldauer, R. Walser, M. L. Donten, R. Pfister, N. Blöchliger, S. Steiner, A. Caflisch, O. Zerbe, and P. Hamm, *Kinetic response of a photoperturbed allosteric protein,* Proceedings of the National Academy of Sciences **110**, 11725 (2013).

[157] C. Viappiani, S. Abbruzzetti, L. Ronda, S. Bettati, E. R. Henry, A. Mozzarelli, and W. A. Eaton, *Experimental basis for a new allosteric model for multisubunit proteins,* Proceedings of the National Academy of Sciences **111**, 12758 (2014).

[158] S. Buchenberg, F. Sittel, and G. Stock, *Time-resolved observation of protein allosteric communication,* Proceedings of the National Academy of Sciences **114**, E6804 (2017).

[159] O. Bozovic, C. Zanobini, A. Gulzar, B. Jankovic, D. Buhrke, M. Post, S. Wolf, G. Stock, and P. Hamm, *Real-time observation of ligand-induced allosteric transitions in a PDZ domain,* Proceedings of the National Academy of Sciences (2020), 10.1073/pnas.2012999117.

[160] B. M. T. Burgering and P. J. Coffer, *Protein kinase B (c-Akt) in phosphatidylinositol-3-OH kinase signal transduction,* Nature **376**, 599 (1995).

[161] T. Bouwmeester, A. Bauch, H. Ruffner, P.-O. Angrand, G. Bergamini, K. Croughton, C. Cruciat, D. Eberhard, J. Gagneur, S. Ghidelli, C. Hopf, B. Huhse, R. Mangano, A.-M. Michon, M. Schirle, J. Schlegl, M. Schwab, M. A. Stein, A. Bauer, G. Casari, G. Drewes, A.-C. Gavin, D. B. Jackson, G. Joberty, G. Neubauer, J. Rick, B. Kuster, and G. Superti-Furga, *A physical and functional map of the human TNF-alpha/NF-kappa B signal transduction pathway.* Nature cell biology **6**, 97 (2004).

[162] A. N. Lupas and M. Gruber, *The structure of alpha-helical coiled coils,* Advances in protein chemistry **70**, 37 (2005).

[163] M. Inouye, *Signaling by Transmembrane Proteins Shifts Gears,* Cell **126**, 829 (2006).

[164] M. Hulko, F. Berndt, M. Gruber, J. U. Linder, V. Truffault, A. Schultz, J. Martin, J. E. Schultz, A. N. Lupas, and M. Coles, *The HAMP Domain Structure Implies Helix Rotation in Transmembrane Signaling,* Cell **126**, 929 (2006).

[165] E. E. Matthews, M. Zoonens, and D. M. Engelman, *Dynamic Helix Interactions in Transmembrane Signaling,* Cell **127**, 447 (2006).

[166] V. Anantharaman, S. Balaji, and L. Aravind, *The signaling helix: a common functional theme in diverse signaling proteins,* Biology direct **1**, 25 (2006).

[167] M. Hinczewski and R. R. Netz, *Global cross-over dynamics of single semiflexible polymers,* EPL (Europhysics Letters) **88**, 18001 (2009).

[168] R. Kubo, *The fluctuation-dissipation theorem,* Reports on Progress in Physics **29**, 255 (1966).

[169] R. P. Diensthuber, M. Bommer, T. Gleichmann, and A. Möglich, *Full-Length Structure of a Sensor Histidine Kinase Pinpoints Coaxial Coiled Coils as Signal Transducers and Modulators,* Structure **21**, 1127 (2013).

[170] H. M. Berman, J. Westbrook, Z. Feng, G. Gilliland, T. N. Bhat, H. Weissig, I. N. Shindyalov, and P. E. Bourne, *The Protein Data Bank,* Nucleic Acids Research **28**, 235 (2000).

[171] S. Páll, M. J. Abraham, C. Kutzner, B. Hess, and E. Lindahl, in *Solving Software Challenges for Exascale*, edited by S. Markidis and E. Laure (Springer International Publishing, Cham, 2015) pp. 3–27.

[172] M. J. Abraham, T. Murtola, R. Schulz, S. Páll, J. C. Smith, B. Hess, and E. Lindahl, *GROMACS: High performance molecular simulations through multi-level parallelism from laptops to supercomputers,* SoftwareX **1-2**, 19 (2015).

[173] A. D. MacKerell, D. Bashford, M. Bellott, R. L. Dunbrack, J. D. Evanseck, M. J. Field, S. Fischer, J. Gao, H. Guo, S. Ha, D. Joseph-McCarthy, L. Kuchnir, K. Kuczera, F. T. K. Lau, C. Mattos, S. Michnick, T. Ngo, D. T. Nguyen, B. Prodhom, W. E. Reiher, B. Roux, M. Schlenkrich, J. C. Smith, R. Stote, J. Straub, M. Watanabe, J. Wiórkiewicz-Kuczera, D. Yin, and M. Karplus, *All-Atom Empirical Potential for Molecular Modeling and Dynamics Studies of Proteins,* The Journal of Physical Chemistry B **102**, 3586 (1998).

[174] A. D. Mackerell Jr., M. Feig, and C. L. Brooks III, *Extending the treatment of backbone energetics in protein force fields: Limitations of gas-phase quantum mechanics in reproducing protein conformational distributions in molecular dynamics simulations,* Journal of Computational Chemistry **25**, 1400 (2004).

[175] W. L. Jorgensen, J. Chandrasekhar, J. D. Madura, R. W. Impey, and M. L. Klein, *Comparison of simple potential functions for simulating liquid water,* The Journal of Chemical Physics **79**, 926 (1983).

[176] G. Bussi, D. Donadio, and M. Parrinello, *Canonical sampling through velocity rescaling,* The Journal of Chemical Physics **126**, 14101 (2007).

[177] M. Parrinello and A. Rahman, *Polymorphic transitions in single crystals: A new molecular dynamics method,* Journal of Applied Physics **52**, 7182 (1981).

[178] S. G. Johnson and M. Frigo, *A modified split-radix FFT with fewer arithmetic operations,* IEEE Trans. Signal Processing **55**, 111 (2007).

[179] M. Frigo and S. G. Johnson, *The Fastest Fourier Transform in the West*, Tech. Rep. MIT-LCS-TR-728 (Massachusetts Institute of Technology, 1997).

[180] M. Frigo and S. G. Johnson, in *Proc. 1998 IEEE Intl. Conf. Acoustics Speech and Signal Processing*, Vol. 3 (IEEE, 1998) pp. 1381–1384.

[181] M. Frigo, in *Proc. 1999 ACM SIGPLAN Conf. on Programming Language Design and Implementation*, Vol. 34 (ACM, 1999) pp. 169–180.

[182] M. Frigo, C. E. Leiserson, H. Prokop, and S. Ramachandran, in *Proc. 40th Ann. Symp. on Foundations of Comp. Sci. (FOCS)* (IEEE Comput. Soc., 1999) pp. 285–297.

[183] S. G. Johnson and M. Frigo, in *Fast Fourier Transforms*, edited by C. S. Burrus (Connexions, Rice University, Houston TX, 2008) Chap. 11.

[184] Z. Bao, Y. Feng, A. Dodabalapur, V. R. Raju, and A. J. Lovinger, *High-Performance Plastic Transistors Fabricated by Printing Techniques,* Chem. Mater. **9**, 1299 (1997).

[185] E. J. Bienk and N. J. Mikkelsen, *Application of advanced surface treatment technologies in the modern plastics moulding industry,* Wear **207**, 6 (1997).

[186] C.-T. Chen and K. S. Suslick, *One-dimensional coordination polymers: Applications to material science,* Coord. Chem. Rev. **128**, 293 (1993).

[187] K. Gall, C. M. Yakacki, Y. Liu, R. Shandas, N. Willett, and K. S. Anseth, *Thermomechanics of the shape memory effect in polymers for biomedical applications,* J. Biomed. Mater. Res., Part A **73A**, 339 (2005).

[188] J. L. Keddie, R. A. L. Jones, and R. A. Cory, *Size-Dependent Depression of the Glass Transition Temperature in Polymer Films.* Europhys. Lett. **27**, 59 (1994).

[189] S. Kuroyanagi, N. Shimada, S. Fujii, T. Furuta, A. Harada, K. Sakurai, and A. Maruyama, *Highly Ordered Polypeptide with UCST Phase Separation Behavior,* J. Am. Chem. Soc. **141**, 1261 (2019).

[190] J. P. Magnusson, A. Khan, G. Pasparakis, A. O. Saeed, W. Wang, and C. Alexander, *Ion-sensitive "isothermal" responsive polymers prepared in water,* J. Am. Chem. Soc. **130**, 10852 (2008).

[191] M. Wei, Y. Gao, X. Li, and M. J. Serpe, *Stimuli-responsive polymers and their applications,* Polym. Chem. **8**, 127 (2017).

[192] H. Huang and M. J. Serpe, *Poly(N-isopropylacrylamide) microgel-based etalons for determining the concentration of ethanol in gasoline,* J. Appl. Polym. Sci. **132**, 24106 (2015).

[193] Y.-Z. You, K. K. Kalebaila, S. L. Brock, and D. Oupický, *Temperature-Controlled Uptake and Release in PNIPAM-Modified Porous Silica Nanoparticles,* Chem. Mater. **20**, 3354 (2008).

[194] J. Qian and F. Wu, *Thermosensitive PNIPAM semi-hollow spheres for controlled drug release,* J. Mater. Chem. B **1**, 3464 (2013).

[195] M. Geisler, S. Xiao, E. M. Puchner, F. Gräter, and T. Hugel, *Controlling the structure of proteins at surfaces,* J. Am. Chem. Soc. **132**, 17277 (2010).

[196] F. W. S. Stetter, L. Cwiklik, P. Jungwirth, and T. Hugel, *Single lipid extraction: the anchoring strength of cholesterol in liquid-ordered and liquid-disordered phases,* Biophys. J. **107**, 1167 (2014).

[197] I. T. S. Li and G. C. Walker, *Signature of hydrophobic hydration in a single polymer,* Proc. Natl. Acad. Sci. U. S. A. **108**, 16527 (2011).

[198] S. Kienle, S. Liese, N. Schwierz, R. R. Netz, and T. Hugel, *The effect of temperature on single-polypeptide adsorption,* ChemPhysChem **13**, 982 (2012).

[199] S. Cui, X. Pang, S. Zhang, Y. Yu, H. Ma, and X. Zhang, *Unexpected Temperature-Dependent Single Chain Mechanics of Poly(N-isopropyl-acrylamide) in Water,* Langmuir **28**, 5151 (2012).

[200] X. Liang and K. Nakajima, *Nanofishing of a Single Polymer Chain: Temperature-Induced Coil-Globule Transition of Poly(N -isopropylacrylamide) Chain in Water,* Macromol. Chem. Phys. **219**, 1700394 (2018).

[201] W. Zhang, S. Zou, C. Wang, and X. Zhang, *Single Polymer Chain Elongation of Poly(N -isopropylacrylamide) and Poly(acrylamide) by Atomic Force Microscopy,* J. Phys. Chem. B **104**, 10258 (2000).

[202] M. Heskins and J. E. Guillet, *Solution Properties of Poly(N-isopropylacrylamide),* J. Macromol. Sci., Chem. **2**, 1441 (1968).

[203] H. Mao, C. Li, Y. Zhang, D. E. Bergbreiter, and P. S. Cremer, *Measuring LCSTs by novel temperature gradient methods: evidence for intermolecular interactions in mixed polymer solutions,* J. Am. Chem. Soc. **125**, 2850 (2003).

[204] S. A. Deshmukh, S. K. R. S. Sankaranarayanan, K. Suthar, and D. C. Mancini, *Role of Solvation Dynamics and Local Ordering of Water in Inducing Conformational Transitions in Poly(N-isopropylacrylamide) Oligomers through the LCST,* J. Phys. Chem. B **116**, 2651 (2012).

[205] J. E. Chung, M. Yokoyama, M. Yamato, T. Aoyagi, Y. Sakurai, and T. Okano, *Thermo-responsive drug delivery from polymeric micelles constructed using block copolymers of poly(N-isopropylacrylamide) and poly(butylmethacrylate),* J. Controlled Release **62**, 115 (1999).

[206] T. Okano, Y. H. Bae, H. Jacobs, and S. W. Kim, *Thermally on-off switching polymers for drug permeation and release,* J. Controlled Release **11**, 255 (1990).

[207] D. Kato, W. Y. Sohn, and K. Katayama, *Aggregation-Induced Expansion of Poly-(N-isopropyl acrylamide) Solutions Observed Directly by the Transient Grating Imaging Technique,* ACS Omega **3**, 8484 (2018).

[208] L. J. Abbott, A. K. Tucker, and M. J. Stevens, *Single Chain Structure of a Poly(N-isopropylacrylamide) Surfactant in Water,* J. Phys. Chem. B **119**, 3837 (2015).

[209] M. H. Futscher, M. Philipp, P. Müller-Buschbaum, and A. Schulte, *The Role of Backbone Hydration of Poly(N-isopropyl acrylamide) across the Volume Phase Transition Compared to Its Monomer,* Sci. Rep. **7**, 17012 (2017).

[210] E. Kutnyanszky, A. Embrechts, M. A. Hempenius, and G. J. Vancso, *Is there a molecular signature of the LCST of single PNIPAM chains as measured by AFM force spectroscopy?* Chem. Phys. Lett. **535**, 126 (2012).

[211] A. J. Harnoy, I. Rosenbaum, E. Tirosh, Y. Ebenstein, R. Shaharabani, R. Beck, and R. J. Amir, *Enzyme-Responsive Amphiphilic PEG-Dendron Hybrids and Their Assembly into Smart Micellar Nanocarriers,* J. Am. Chem. Soc. **136**, 7531 (2014).

[212] R. Duncan, *Polymer conjugates as anticancer nanomedicines,* Nat. Rev. Cancer **6**, 688 (2006).

[213] J. Chen, S. K. Spear, J. G. Huddleston, and R. D. Rogers, *Polyethylene glycol and solutions of polyethylene glycol as green reaction media,* Green Chem. **7**, 64 (2005).

[214] C. Brandenberger, C. Mühlfeld, Z. Ali, A.-G. Lenz, O. Schmid, W. J. Parak, P. Gehr, and B. Rothen-Rutishauser, *Quantitative Evaluation of Cellular Uptake and Trafficking of Plain and Polyethylene Glycol-Coated Gold Nanoparticles,* Small **6**, 1669 (2010).

[215] R. Kjellander and E. Florin, *Water structure and changes in thermal stability of the system poly(ethylene oxide)–water,* J. Chem. Soc., Faraday Trans. 1 **77**, 2053 (1981).

[216] B. Balzer and T. Hugel, in *Polymer Science: A Comprehensive Reference*, edited by K. Matyjaszewski and M. Möller (Elsevier, Amsterdam, 2012) pp. 629 – 645.

[217] F. Oesterhelt, M. Rief, and H. E. Gaub, *Single molecule force spectroscopy by AFM indicates helical structure of poly(ethylene-glycol) in water,* New J. Phys. **1**, 6.1 (1999).

[218] L. S. Bartell, *On the Effects of Intramolecular van der Waals Forces,* J. Chem. Phys. **32**, 827 (1960).

[219] B. Hess, C. Kutzner, D. van der Spoel, and E. Lindahl, *GROMACS 4: Algorithms for Highly Efficient, Load-Balanced, and Scalable Molecular Simulation,* J. Chem. Theory Comput. **4**, 435 (2008).

[220] G. Bussi, D. Donadio, and M. Parrinello, *Canonical sampling through velocity rescaling,* J. Chem. Phys. **126**, 014101 (2007).

[221] M. Parrinello and A. Rahman, *Polymorphic transitions in single crystals: A new molecular dynamics method,* J. Appl. Phys. **52**, 7182 (1981).

[222] U. Essmann, L. Perera, M. L. Berkowitz, T. Darden, H. Lee, and L. G. Pedersen, *A smooth particle mesh Ewald method,* J. Chem. Phys. **103**, 8577 (1995).

[223] H. Lee, R. M. Venable, A. D. Mackerell, and R. W. Pastor, *Molecular dynamics studies of polyethylene oxide and polyethylene glycol: hydrodynamic radius and shape anisotropy,* Biophys. J. **95**, 1590 (2008).

[224] H. J. C. Berendsen, J. R. Grigera, and T. P. Straatsma, *The missing term in effective pair potentials,* J. Phys. Chem. **91**, 6269 (1987).

[225] W. L. Jorgensen and J. Tirado-Rives, *The OPLS optimized potentials for liquid simulations potential functions for proteins, energy minimizations for crystals of cyclic peptides and crambin,* J. Am. Chem. Soc. **110**, 1657 (1988).

[226] M. Kanduč, R. Chudoba, K. Palczynski, W. K. Kim, R. Roa, and J. Dzubiella, *Selective solute adsorption and partitioning around single PNIPAM chains,* Phys. Chem. Chem. Phys. **19**, 5906 (2017).

[227] V. Palivec, D. Zadrazil, and J. Heyda, *All-atom REMD simulation of poly-N-isopropylacrylamide thermodynamics in water: a model with a distinct 2-state behavior,* arXiv , arXiv:1806.05592 (2018).

[228] T. Pirzer and T. Hugel, *Atomic force microscopy spring constant determination in viscous liquids,* Rev. Sci. Instrum. **80**, 035110 (2009).

[229] R. Walder, M.-A. LeBlanc, W. J. van Patten, D. T. Edwards, J. A. Greenberg, A. Adhikari, S. R. Okoniewski, R. M. A. Sullan, D. Rabuka, M. C. Sousa, and T. T. Perkins, *Rapid Characterization of a Mechanically Labile α-Helical Protein Enabled by Efficient Site-Specific Bioconjugation,* J. Am. Chem. Soc. **139**, 9867 (2017).

[230] R. G. Barradas, S. Fletcher, and J. D. Porter, *The hydrolysis of maleimide in alkaline solution,* Can. J. Chem. **54**, 1400 (1976).

[231] J. L. Hutter and J. Bechhoefer, *Calibration of atomic-force microscope tips,* Rev. Sci. Instrum. **64**, 1868 (1993).

[232] B. Trathnigg, *Determination of MWD and chemical composition of polymers by chromatographic techniques,* Prog. Polym. Sci. **20**, 615 (1995).

[233] J. Blass, M. Albrecht, G. Wenz, Y. N. Zang, and R. Bennewitz, *Single-molecule force spectroscopy of fast reversible bonds,* Phys. Chem. Chem. Phys. **19**, 5239 (2017).

[234] A. Serr and R. R. Netz, *Pulling adsorbed polymers from surfaces with the AFM: stick vs. slip, peeling vs. gliding,* EPL **73**, 292 (2006).

[235] B. N. Balzer, M. Gallei, M. V. Hauf, M. Stallhofer, L. Wiegleb, A. Holleitner, M. Rehahn, and T. Hugel, *Nanoscale friction mechanisms at solid-liquid interfaces,* Angew. Chem., Int. Ed. **52**, 6541 (2013).

[236] A. Fava, A. Iliceto, and E. Camera, *Kinetics of the Thiol-Disulfide Exchange,* J. Am. Chem. Soc. **79**, 833 (1957).

[237] T. Hugel, M. Rief, M. Seitz, H. E. Gaub, and R. R. Netz, *Highly Stretched Single Polymers: Atomic-Force-Microscope Experiments versus Ab-Initio Theory,* Phys. Rev. Lett. **94**, 048301 (2005).

[238] P. Marchand and L. Marmet, *Binomial smoothing filter: A way to avoid some pitfalls of least-squares polynomial smoothing,* Rev. Sci. Instrum. **54**, 1034 (1983).

[239] B. Li, X. Wang, Y. Li, A. Paananen, G. R. Szilvay, M. Qin, W. Wang, and Y. Cao, *Single-Molecule Force Spectroscopy Reveals Self-Assembly Enhanced Surface Binding of Hydrophobins,* Chem. - Eur. J. **24**, 9224 (2018).

[240] N. Idota, K. Nagase, K. Tanaka, T. Okano, and M. Annaka, *Stereoregulation of Thermoresponsive Polymer Brushes by Surface-Initiated Living Radical Polymerization and the Effect of Tacticity on Surface Wettability,* Langmuir **26**, 17781 (2010).

[241] S. B. Smith, L. Finzi, and C. Bustamante, *Direct Mechanical Measurements of the Elasticity of Single DNA Molecules by Using Magnetic Beads,* Science **258**, 1122 (1992).

[242] J. F. Marko and E. D. Siggia, *Stretching DNA,* Macromolecules **28**, 8759 (1995).

[243] Y. Katsumoto, T. Tanaka, H. Sato, and Y. Ozaki, *Conformational change of poly(N-isopropylacrylamide) during the coil-globule transition investigated by attenuated total reflection/infrared spectroscopy and density functional theory calculation,* J. Phys. Chem. A **106**, 3429 (2002).

[244] S. Y. Lin, K. S. Chen, and R. C. Liang, *Thermal micro ATR/FT-IR spectroscopic system for quantitative study of the molecular structure of poly(N-isopropylacrylamide) in water,* Polymer **40**, 2619 (1999).

[245] Y. Maeda, T. Nakamura, and I. Ikeda, *Changes in the Hydration States of Poly(N-alkylacrylamide)s during Their Phase Transitions in Water Observed by FTIR Spectroscopy,* Macromolecules **34**, 1391 (2001).

[246] A. Percot, X. X. Zhu, and M. Lafleur, *A simple FTIR spectroscopic method for the determination of the lower critical solution temperature of N-isopropylacrylamide copolymers and related hydrogels,* J. Polym. Sci., Part B: Polym. Phys. **38**, 907 (2000).

[247] J. Chen, M. Liu, H. Gong, Y. Huang, and C. Chen, *Synthesis and Self-Assembly of Thermoresponsive PEG-b-PNIPAM-b-PCL ABC Triblock Copolymer through the Combination of Atom Transfer Radical Polymerization, Ring-Opening Polymerization, and Click Chemistry,* J. Phys. Chem. B **115**, 14947 (2011).

[248] J. Es Sayed, C. Lorthioir, P. Perrin, and N. Sanson, *PEGylated NiPAM microgels: synthesis, characterization and colloidal stability,* Soft Matter **15**, 963 (2019).

[249] B. Zhu, N. Jasinski, A. Benitez, M. Noack, D. Park, A. S. Goldmann, C. Barner-Kowollik, and A. Walther, *Hierarchical Nacre Mimetics with Synergistic Mechanical Properties by Control of Molecular Interactions in Self-Healing Polymers,* Angew. Chem., Int. Ed. **54**, 8653 (2015).

[250] R. Merindol, G. Delechiave, L. Heinen, L. H. Catalani, and A. Walther, *Modular Design of Programmable Mechanofluorescent DNA Hydrogels,* Nat. Commun. **10**, 528 (2019).

[251] V. Huck, M. F. Schneider, C. Gorzelanny, and S. W. Schneider, *The various states of von Willebrand factor and their function in physiology and pathophysiology,* Thrombosis and Haemostasis **111**, 598 (2014).

[252] A. Löf, J. P. Müller, and M. A. Brehm, *A biophysical view on von Willebrand factor activation,* Journal of Cellular Physiology **233**, 799 (2018).

[253] Z. Ruggeri and T. Zimmerman, *von Willebrand factor and von Willebrand disease,* Blood **70**, 895 (1987).

[254] H. Fu, Y. Jiang, D. Yang, F. Scheiflinger, W. P. Wong, and T. A. Springer, *Flow-induced elongation of von Willebrand factor precedes tension-dependent activation,* Nature Communications **8**, 324 (2017).

[255] D. E. Smith, H. P. Babcock, and S. Chu, *Single-Polymer Dynamics in Steady Shear Flow,* Science **283**, 1724 (1999).

[256] J. S. Myung, F. Taslimi, R. G. Winkler, and G. Gompper, *Self-Organized Structures of Attractive End-Functionalized Semiflexible Polymer Suspensions,* Macromolecules **47**, 4118 (2014).

[257] M. K. Singh, P. Ilg, R. M. Espinosa-Marzal, M. Kröger, and N. D. Spencer, *Polymer Brushes under Shear: Molecular Dynamics Simulations Compared to Experiments,* Langmuir **31**, 4798 (2015).

[258] T. Eisenstecken, G. Gompper, and R. G. Winkler, *Conformational Properties of Active Semiflexible Polymers,* Polymers **8**, 304 (2016).

[259] M. Hoore, K. Rack, D. A. Fedosov, and G. Gompper, *Flow-induced adhesion of shear-activated polymers to a substrate,* Journal of Physics: Condensed Matter **30**, 064001 (2018).

[260] A. Alexander-Katz and R. R. Netz, *Dynamics and Instabilities of Collapsed Polymers in Shear Flow,* Macromolecules **41**, 3363 (2008).

[261] M. Radtke, M. Radtke, and R. Netz, *Shear-induced dynamics of polymeric globules at adsorbing homogeneous and inhomogeneous surfaces,* The European Physical Journal E **37**, 20 (2014).

[262] M. A. Cruz, H. Yuan, J. R. Lee, R. J. Wise, and R. I. Handin, *Interaction of the von Willebrand Factor (vWF) with Collagen: Localization of the primary collagen-binding site by analysis of recombinant vwf a domain polypeptides,* Journal of Biological Chemistry **270**, 10822 (1995).

[263] J. Chen and J. A. Lopez, *Interactions of Platelets with Subendothelium and Endothelium,* Microcirculation **12**, 235 (2005).

[264] V. J. Marder, W. C. Aird, J. S. Bennett, S. Schulman, and G. C. W. II, *Hemostasis and thrombosis: basic principles and clinical practice*, 6th ed. (Wolters Kluwer / LWW, 2013).

[265] J. P. Müller, S. Mielke, A. Löf, T. Obser, C. Beer, L. K. Bruetzel, and D. A. Pippig, *Force sensing by the vascular protein von Willebrand factor is tuned by a strong intermonomer interaction,* Proceedings of the National Academy of Sciences **I**, 1 (2016).

[266] Y. von Hansen, M. Hinczewski, and R. R. Netz, *Hydrodynamic screening near planar boundaries: Effects on semiflexible polymer dynamics,* The Journal of Chemical Physics **134**, 235102 (2011).

[267] T. T. Pham, M. Bajaj, and J. R. Prakash, *Brownian dynamics simulation of polymer collapse in a poor solvent: Influence of implicit hydrodynamic interactions,* Soft Matter **4**, 1196 (2008).

[268] H. Kramers, *Brownian motion in a field of force and the diffusion model of chemical reactions,* Physica **7**, 284 (1940).

[269] G. Bell, *Models for the specific adhesion of cells to cells,* Science **200**, 618 (1978).

[270] O. K. Dudko, G. Hummer, and A. Szabo, *Intrinsic Rates and Activation Free Energies from Single-Molecule Pulling Experiments,* Physical Review Letters **96**, 108101 (2006).

[271] J. T. Bullerjahn, S. Sturm, and K. Kroy, *Theory of rapid force spectroscopy,* Nature Communications **5**, 4463 (2014).

[272] E. Wajnryb, K. a. Mizerski, P. J. Zuk, and P. Szymczak, *Generalization of the Rotne–Prager–Yamakawa mobility and shear disturbance tensors,* Journal of Fluid Mechanics **731**, R3 (2013).

[273] M. Radtke and R. R. Netz, *Shear-enhanced adsorption of a homopolymeric globule mediated by surface catch bonds,* The European Physical Journal E **38**, 69 (2015).

[274] M. Stimson and G. B. Jeffery, *The Motion of Two Spheres in a Viscous Fluid,* Proceedings of the Royal Society of London A: Mathematical, Physical and Engineering Sciences **111**, 110 (1926).

[275] G. S. Perkins and R. B. Jones, *Hydrodynamic interaction of a spherical particle with a planar boundary I. Free surface,* Physica A: Statistical Mechanics and its Applications **171**, 575 (1991).

[276] J. Tang, N. Du, and P. S. Doyle, *Compression and self-entanglement of single DNA molecules under uniform electric field,* Proceedings of the National Academy of Sciences **108**, 16153 (2011).

[277] C. Sendner and R. R. Netz, *Single flexible and semiflexible polymers at high shear: Non-monotonic and non-universal stretching response,* The European Physical Journal E **30**, 75 (2009).

[278] P. S. Doyle, B. Ladoux, and J. L. Viovy, *Dynamics of a tethered polymer in shear flow.* Physical review letters **84**, 4769 (2000).

[279] C. E. Sing, T. R. Einert, R. R. Netz, and A. Alexander-Katz, *Probing structural and dynamical transitions in polymer globules by force,* Physical Review E **83**, 040801 (2011).

[280] C. Sing and A. Alexander-Katz, *Theory of tethered polymers in shear flow: The strong stretching limit,* Macromolecules **44**, 9020 (2011).

[281] J. Kestin, M. Sokolov, and W. A. Wakeham, *Viscosity of liquid water in the range -8 °C to 150 °C,* Journal of Physical and Chemical Reference Data **7**, 941 (1978).

[282] A. Kolberg, C. Wenzel, K. Hackenstrass, R. Schwarzl, C. Rüttiger, T. Hugel, M. Gallei, R. R. Netz, and B. N. Balzer, *Opposing Temperature Dependence of the Stretching Response of Single PEG and PNiPAM Polymers,* Journal of the American Chemical Society **141**, 11603 (2019).

[283] H. Hoshina, Y. Saito, T. Furuhashi, T. Shimazaki, M. Sawada, Y. Hioki, and C. Otani, *Terahertz Spectroscopy for Characterization of Hydrogen Bonding and Cross-linked Structure Dynamics in Polyurethane,* Journal of Infrared, Millimeter, and Terahertz Waves **41**, 265 (2020).

[284] J. Lu, Y. Zhang, H. Y. Hwang, B. K. Ofori-Okai, S. Fleischer, and K. A. Nelson, *Nonlinear two-dimensional terahertz photon echo and rotational spectroscopy in the gas phase,* Proceedings of the National Academy of Sciences (2016), 10.1073/pnas.1609558113.

[285] C. S. Ponseca, O. Kambara, S. Kawaguchi, K. Yamamoto, and K. Tominaga, *Low-Frequency Spectra of Amino Acids and Short-Chain Peptides Studied by Terahertz Time-Domain Spectroscopy,* Journal of Infrared, Millimeter, and Terahertz Waves **31**, 799 (2010).

[286] B. Yu, F. Zeng, Y. Yang, Q. Xing, A. Chechin, X. Xin, I. Zeylikovich, and R. R. Alfano, *Torsional Vibrational Modes of Tryptophan Studied by Terahertz Time-Domain Spectroscopy,* Biophysical Journal **86**, 1649 (2004).

[287] M. R. Kutteruf, C. M. Brown, L. K. Iwaki, M. B. Campbell, T. M. Korter, and E. J. Heilweil, *Terahertz spectroscopy of short-chain polypeptides,* Chemical Physics Letters **375**, 337 (2003).

[288] M. A. Ward and T. K. Georgiou, *Thermoresponsive Polymers for Biomedical Applications,* Polymers **3**, 1215 (2011).

[289] D. Roy, W. L. A. Brooks, and B. S. Sumerlin, *New directions in thermoresponsive polymers,* Chem. Soc. Rev. **42**, 7214 (2013).

[290] J. Zhang, W. Chen, L. Yu, M. Li, F. Neumann, W. Li, and R. Haag, *Selective Endothelial Cell Adhesion via Mussel-Inspired Hybrid Microfibrous Scaffold,* ACS Applied Nano Materials **1**, 1513 (2018).

[291] P. Zarrintaj, M. Jouyandeh, M. R. Ganjali, B. S. Hadavand, M. Mozafari, S. S. Sheiko, M. Vatankhah-Varnoosfaderani, T. J. Gutiérrez, and M. R. Saeb, *Thermo-sensitive polymers in medicine: A review,* European Polymer Journal **117**, 402 (2019).

[292] W. Deng, Y. Xu, W. Chen, D. S. Paul, A. K. Syed, M. A. Dragovich, X. Liang, P. Zakas, M. C. Berndt, J. Di Paola, J. Ware, F. Lanza, C. B. Doering, W. Bergmeier, X. F. Zhang, and R. Li, *Platelet clearance via shear-induced unfolding of a membrane mechanoreceptor,* Nature Communications **7**, 12863 (2016).

[293] L. Ju, Y. Chen, L. Xue, X. Du, and C. Zhu, *Cooperative unfolding of distinctive mechanoreceptor domains transduces force into signals,* eLife **5**, e15447 (2016).

[294] M. Morabito, C. Dong, W. Wei, X. Cheng, X. F. Zhang, A. Oztekin, and E. Webb, *Internal Tensile Force and A2 Domain Unfolding of von Willebrand Factor Multimers in Shear Flow,* Biophysical Journal **115**, 1860 (2018).

[295] C. Dong, J. Lee, S. Kim, W. Lai, E. B. Webb, A. Oztekin, X. F. Zhang, and W. Im, *Long-ranged Protein-glycan Interactions Stabilize von Willebrand Factor A2 Domain from Mechanical Unfolding,* Scientific Reports **8**, 16017 (2018).

[296] R. Schwarzl, S. Liese, F. N. Brünig, F. Laudisio, and R. R. Netz, *Force Response of Polypeptide Chains from Water-Explicit MD Simulations,* Macromolecules **53**, 4618 (2020).

[297] A. Möglich, *Signaltransduktion einer lichtregulierten Sensorhistidinkinase,* Nachrichten aus der Chemie **66**, 123 (2018).

[298] A. Löf, P. U. Walker, S. M. Sedlak, S. Gruber, T. Obser, M. A. Brehm, M. Benoit, and J. Lipfert, *Multiplexed protein force spectroscopy reveals equilibrium protein folding dynamics and the low-force response of von Willebrand factor,* Proceedings of the National Academy of Sciences **116**, 18798 LP (2019).

[299] C. Djerassi, M. Gorman, F. X. Markley, and E. B. Oldenburg, *Studies in Organic Sulfur Compounds. VII.1 Lithium Aluminum Hydride Reduction of Xanthates to Mercaptans. Synthesis of Substituted β-Mercaptoethanols,* Journal of the American Chemical Society **77**, 568 (1955).

[300] C. W. Scales, A. J. Convertine, and C. L. McCormick, *Fluorescent Labeling of RAFT-Generated Poly(N-isopropylacrylamide) via a Facile Maleimide-Thiol Coupling Reaction,* Biomacromolecules **7**, 1389 (2006).

[301] N. Idota, K. Nagase, K. Tanaka, T. Okano, and M. Annaka, *Stereoregulation of Thermoresponsive Polymer Brushes by Surface-Initiated Living Radical Polymerization and the Effect of Tacticity on Surface Wettability.* Langmuir **26**, 17781 (2010).

[302] M. Fixman and J. Kovac, *Polymer conformational statistics. III. Modified Gaussian models of stiff chains,* The Journal of Chemical Physics **58**, 1564 (1973).

[303] A. Dittmore, D. B. McIntosh, S. Halliday, and O. A. Saleh, *Single-Molecule Elasticity Measurements of the Onset of Excluded Volume in Poly(Ethylene Glycol),* Phys. Rev. Lett. **107**, 148301 (2011).

[304] H. Flyvbjerg and H. G. Petersen, *Error estimates on averages of correlated data,* The Journal of Chemical Physics **91**, 461 (1989).

[305] T. Hugel, N. B. Holland, A. Cattani, L. Moroder, M. Seitz, and H. E. Gaub, *Single-Molecule Optomechanical Cycle,* Science **296**, 1103 (2002).

[306] B. Hess, C. Kutzner, D. van der Spoel, and E. Lindahl, *GROMACS 4: Algorithms for Highly Efficient, Load-Balanced, and Scalable Molecular Simulation,* Journal of Chemical Theory and Computation **4**, 435 (2008).

[307] B. Hess, *Determining the shear viscosity of model liquids from molecular dynamics simulations,* The Journal of Chemical Physics **116**, 209 (2002).

Abstract

Understanding the mechanical response of polymers to external force gives crucial insights into physiological processes. In this thesis we present the force extension relation of homo- and polypeptides as well as two synthetic polymer examples. Our findings rely on a combination of molecular or Brownian dynamics simulations, analytical modeling, and comparison to experimental results.
First, we present the force-extension relations for the five homopeptides from molecular dynamics simulations in explicit water. The Kuhn length, equilibrium contour length and linear and nonlinear stretching moduli are deduced. An augmented freely rotating chain model, which accounts for side-chain interactions and restricted dihedral rotation, is shown to describe the simulated force-extension relations very well. We present a comparison between published experimental single-molecule force-extension curves for different polypeptides with simulation and model predictions. The simulations allow for the disentanglement of energetic and entropic contributions to the stretching energy of the polypeptides.
Secondly, molecular dynamics simulations of a coiled coil linker present in photoreceptor histidine kinases are evaluated in terms of three different mechanical modes which are candidates for signal transmission. The levels of the output signals of shift, splay, and twist on one end of the coiled coil linker are quantified as a function over a wide range of frequencies for the driving force input on the other end of the coiled coil linker by investigation of response functions.
Thirdly, the opposite temperature dependence of polyethylene glycol and poly(N-isopropylacrylamide) is investigated from a basis of single molecule force spectroscopy and molecular dynamics simulations in explicit water. Energetic and entropic contributions are deduced from simulations and compared for PEG and PNiPAM. Hydration effects are shown to explain the different temperature dependent responses.
Finally, the response of the glycoprotein von Willebrand factor to linear shear flow is examined by a coarse-grained model in Brownian dynamics simulations including long range hydrodynamic interactions. Tensile forces and the shear-rate-dependent globular-coil transition are investigated. The scaling of the critical shear rate for the globular-coil transition with the monomer number is inverse for the grafted and non-grafted scenarios. This implicates that for the grafted scenario, larger chains have a decreased critical shear rate, while for the non-grafted scenario higher shear rates are needed to unfold larger chains.

Kurzfassung

Ein Verständnis der mechanischen Antwort von Polymeren auf eine äußere Kraft gibt wichtige Einblicke in physiologisch relevante Prozesse. In dieser Arbeit präsentieren wir Kraft-Dehnungs-Kurven von Homo- und Polypeptiden und von zwei synthetischen Polymeren. Unsere Ergebnisse basieren auf computerbasierten Simulationsmethoden, analytischen Berechnungen und Vergleichen mit experimentellen Daten.
Zuerst zeigen wir die Kraft-Dehnungs-Kurven für fünf Homopeptide aus Molekulardynamiksimulationen in explizitem Wasser. Ein abgewandeltes Polymermodel der frei rotierenden Kette, das die sterische Wechselwirkung der Seitenketten und die Einschränkung der Torsionswinkel berücksichtigt, liefert eine sehr gute Übereinstimmung mit den simulierten Kraft-Dehnungs-Kurven. Wir präsentieren einen Vergleich von experimentellen Daten für verschiedene Polypeptide mit unseren Simulations- und Modellvorhersagen. Die Simulationen ermöglichen es, die entropischen und energetischen Beiträge zur notwendigen Arbeit für die Dehnung der Peptide auseinanderzuhalten.
Als zweites zeigen wir Ergebnisse aus Simulationen eines molekularen Verbindungsstückes, das aus zwei nebeneinander verlaufenden α-Helices besteht. Dieses Verbindungsstück ist bei der Signalweiterleitung in einer Kinase beteiligt. Wir untersuchen die Effektivität verschiedener mechanischer Moden wie Verschiebung, Spreizung oder Verdrillung für die Signalweiterleitung. Aus dem Verhältnis einer Kreuzkorrelationsfunktion und einer Eigenkorrelationsfunktion der Enden wird die frequenzabhängige Effizienz der Signalübertragung ermittelt.
Als drittes betrachten wir die gegensätzlichen Temperaturabhängigkeiten der Kraft-Dehnungs-Kurven von Polyethylenglycol und Poly-N-Isopropylacrylamid in einem Vergleich aus Molekulardynamiksimulationsdaten und Rasterkraftmikroskopie einzelner Moleküle. Wir ziehen entropische und energetische Beiträge zur Arbeit, die zur Dehnung der Polymere benötigt wird, aus den Simulationen. Hydrationseffekte erklären die Temperaturabhängigkeiten.
Zuletzt betrachten wir das Blutprotein Von-Willebrand-Faktor unter Einfluss von Scherfluss in Simulationen eines vereinfachten Models auf Basis der zufälligen Molekularbewegung. Dabei werden langreichweitige hydrodynamische Wechselwirkungen berücksichtigt. Wir präsentieren die Zugkräfte und die kritische Scherrate, bei der ein Übergang des Polymers von einem Globul- in einen Coil-Zustand zu beobachten ist. Wir zeigen, dass der Einfluss der Länge der Kette auf die kritische Scherrate gegensätzlich ist, je nachdem ob das Polymer an einem Ende befestigt ist oder nicht.

Selbstständigkeitserklärung

Hiermit erkläre ich, dass ich in der vorliegenden Dissertationsschrift mit dem Titel

Elasticity of Proteins and Polymers from Molecular Dynamics Simulations

die Vorgaben guter wissenschaftlicher Praxis gemäß der Empfehlung der Konferenz der Fachbereiche Physik, Freien Universität Berlin eingehalten habe. Ich erkläre, dass ich Kapitel der vorliegende Dissertationsschrift, sofern diese im Folgenden nicht explizit aufgeführt werden, selbstständig angefertigt habe und hierfür keine anderen als die angegebenen Hilfsmittel verwendet habe. Die vorliegende Dissertationsschrift enthält vorab publizierte Arbeiten, die einen Peer-Review Prozess durchlaufen haben. Diese Publikationen sind eindeutig als solche ausgewiesen und haben immer mehr als einen Autor. Es ist sichergestellt, dass ich diese Publikationen entweder als Erstautor selbst angefertigt habe (Kapitel 2, Kapitel 3 (in der Vorbereitung zur Publikation), Kapitel 5) oder im Fall von Kapitel 4 durch die Aufarbeitung von selbsterstellten Simulationsdaten einen beachtlichen Anteil zu der Publikation beigetragen habe. Den Kapiteln 2, 3, 4 und 5 habe ich jeweils eine Erklärung vorangestellt, die die Beiträge der einzelnen Autoren darlegt. Ich habe sie jeweils aus der folgenden deutschen Originalerklärung übersetzt:

Kapitel 2 und Appendix A "Force Response of Polypeptide Chains from Water-Explicit MD Simulations" : Richard Schwarzl führte alle Simulationen und Analysen durch mit Ausnahme der DFT Rechnungen, die von Florian N. Brünig durchgeführt wurden. Roland R. Netz beaufsichtigte das Projekt. Richard Schwarzl erstellte alle Graphen und schrieb die erste Version des Manuskripts mit Ausnahme des Methodenteils für die DFT Rechnungen, der von Florian N. Brünig geschrieben wurde. Fabio Laudisio trug durch seine Untersuchung des Effekts der Salzkonzentration während seiner Bachelorarbeit unter der Anleitung von Richard Schwarzl zu Grafik A.1 in Appendix A bei. Dabei stellte Richard Schwarzl die Input Dateien für die Simulationen bereit und führte die Simulationen zusätzlich auch selbst durch. Alle Autoren mit Ausnahme von Fabio Laudisio diskutierten die Ergebnisse und trugen zur endgültigen Fassung des Manuskripts bei, das publiziert ist unter: R. Schwarzl, S. Liese, F. N. Brünig, F. Laudisio, and R. R. Netz, Force Response of Polypeptide Chains from Water-Explicit MD Simulations, Macromolecules 53, 4618 (2020).

Kapitel 3 "Quantification of the Frequency-Dependent Signal Transduction for the Coiled Coil Linker Ja" : Richard Schwarzl führte alle Simulationen und Analysen durch. Roland R. Netz beaufsichtigte das Projekt. Richard Schwarzl erstellte alle Grafiken und schrieb das Manuskript, das noch nicht zur Publikation eingereicht ist.

Kapitel 4 und Appendix B "Opposing Temperature Dependence of the Stretching Response of Single PEG and PNiPAM Polymers": Richard Schwarzl führte alle Molekulardynamiksimulationen und die Analyse dieser Daten durch. Die Vorstellung dieser Daten durch Roland R. Netz am Lehrstuhl von Torsten Hugel regte die experimentellen Untersuchungen der Temperaturabhängigkeit des Kraftdehnungsverhaltens von PEG und PNiPAM durch Adrianna Kolberg unter der Anleitung von Bizan N. Balzer an. Richard Schwarzl stellte zu Beginn der experimentellen Untersuchungen eine Übersicht von Simulationsergebnissen und Auswertungsgrafiken bereit. In Vorbereitung auf die Veröffentlichung stellte Richard Schwarzl sein Manuskript zur Temperaturabhängigkeit der Kraftdehnungskurve von PEG Bizan N. Balzer zu Verfügung. Bizan N. Balzer schrieb die erste Version des Manuskripts mit Ausnahme des Methodenteils zu den Simulationen, der von Richard Schwarzl geschrieben wurde. Bizan N. Balzer erstellte alle Grafiken mit Ausnahme der Grafik 4.5 a und 4.5 b und der Snapshots der Molekulardynamiksimulationen in Figur 4.1, die Richard Schwarzl bereitstellte. Die Tabelle B.1 in Appendix B wurde von Richard Schwarzl erstellt und für die Veröffentlichung bereitgestellt. Alle Autoren trugen zur endgültigen Fassung des Manuskripts bei, das publiziert ist unter: A. Kolberg, C. Wenzel, K. Hackenstrass, R. Schwarzl, C. Rüttiger, T. Hugel, M. Gallei, R. R. Netz, and B. N. Balzer, Opposing Temperature Dependence of the Stretching Response of Single PEG and PNiPAM Polymers, Journal of the American Chemical Society 141, 11603 (2019).

Kapitel 5 und Appendix C "Hydrodynamic Shear Effects on Grafted and Non-Grafted Collapsed Polymers": Richard Schwarzl führte alle Simulationen und Analysen durch. Roland R. Netz beaufsichtigte das Projekt. Richard Schwarzl erstellte alle Grafiken und schrieb die erste Version des Manuskripts. Beide Autoren trugen zur endgültigen Fassung des Manuskripts bei, das publiziert ist unter: R. Schwarzl and R. R. Netz, Hydrodynamic Shear Effects on Grafted and Non-Grafted Collapsed Polymers, Polymers 10, 926 (2018).

Die vorliegende Arbeit ist frei von Plagiaten. Alle Ausführungen, die wörtlich oder inhaltlich aus anderen Schriften entnommen sind, habe ich als solche kenntlich gemacht. Die Arbeit ist weder in einem früheren Promotionsverfahren angenommen noch als ungenügend beurteilt worden.

Mit einer Prüfung meiner Arbeit durch ein Plagiatsprüfungsprogramm erkläre ich mich einverstanden.

Berlin, den 22. November 2020

Danksagung

An dieser Stelle möchte ich mich bei allen bedanken, die durch ihre Unterstützung die Entstehung dieser Dissertation vorangetrieben haben.
Mein Dank gilt in erster Linie meinem Doktorvater Prof. Dr. Roland R. Netz, der durch seine klaren Vorstellungen und die Fähigkeit Themen aus den verschiedensten Disziplinen mit der theoretischen Physik zu verbinden, ein besonders vielfältiges Arbeitsumfeld geschaffen hat. Ich bin dankbar für die zahlreichen Diskussionen und Hinweise, die immer zu einer Verbesserung der wissenschaftlichen Arbeit führten. Aus einigen Gesprächen ging ich verärgert, weil meine Arbeit scheinbar wieder nicht ausreichte, nur um später festzustellen, dass die erhaltenen Hinweise zu einer Verbesserung der Ergebnisse führten. Besonders bedanken möchte ich mich auch für die erhalten gebliebene Zusammenarbeit nach meiner Entscheidung, das Referendariat zu beginnen.
Darüber hinaus möchte ich mich bei allen Koautoren und Kollegen bedanken, die meine wissenschaftliche Arbeit begleitet haben, insbesondere Dr. Julius Schulz, Dr. Alexander Schlaich, Dr. Susanne Liese, Dr. Sandra Posch, Dr. Maria Brehm, Dr. Martin Benoit, Dr. Matthias Radtke, Dr. Camilo Aponte-Santamaría, sowie Dr. Fang Du, Prof. Dr. Rainer Haag, Dr. Bizan N. Balzar, Adrianna Kolberg, Prof. Dr. Thorsten Hugel, Florian Brünig, Fabio Laudisio, Alexander Rathert, Dr. Markus Miettinen, Philip Loche, Prof. Dr. Andreas Möglich.
Ein großer Dank geht auch an alle Mitglieder der AG Netz für die kollegiale und angenehme Zusammenarbeit. Besonders dankbar bin ich Dr. Jan Daldrop für seine unterstützende Art, Annette Schumann-Welde für ihre Organisation bei Reisen und Jens Dreger und Jörg Behrmann für die Pflege der IT-Systeme am Fachbereich Physik.
Zuletzt möchte ich meiner Familie herzlich für ihre Unterstützung und ihr Vertrauen danken.